INFORMATION TO USERS

This manuscript has been reproduced from the microfilm master. UMI films the text directly from the original or copy submitted. Thus, some thesis and dissertation copies are in typewriter face, while others may be from any type of computer printer.

The quality of this reproduction is dependent upon the quality of the copy submitted. Broken or indistinct print, colored or poor quality illustrations and photographs, print bleedthrough, substandard margins, and improper alignment can adversely affect reproduction.

In the unlikely event that the author did not send UMI a complete manuscript and there are missing pages, these will be noted. Also, if unauthorized copyright material had to be removed, a note will indicate the deletion.

Oversize materials (e.g., maps, drawings, charts) are reproduced by sectioning the original, beginning at the upper left-hand corner and continuing from left to right in equal sections with small overlaps. Each original is also photographed in one exposure and is included in reduced form at the back of the book.

Photographs included in the original manuscript have been reproduced xerographically in this copy. Higher quality 6" x 9" black and white photographic prints are available for any photographs or illustrations appearing in this copy for an additional charge. Contact UMI directly to order.

UMI®

Bell & Howell Information and Learning
300 North Zeeb Road, Ann Arbor, MI 48106-1346 USA
800-521-0600

Fluid model of dielectric barrier gas discharge

Michel Dufresne, B. Sc., M. Sc.

A thesis submitted to the Faculty of Graduate Studies and Research
in partial fulfillment of the requirements
for the degree of
Doctor of Philosophy

Computational Analysis and Design Laboratory
Department of Electrical Engineering
McGill University, Montreal

May 1997

0-612-36971-4

"What it means really to understand an equation — that is, in more than a strictly mathematical sense — was described by Dirac. He said: "I understand what an equation means if I have a way of figuring out the characteristics of its solution without actually solving it." A physical understanding is a completely unmathematical, imprecise, and inexact thing, but absolutely necessary for a Physicist"

Richard P. Feynman, 1962

To the memory of Professor Peter P. Silvester

Abstract

A two-fluid model of dielectric barrier gas discharge is presented in this thesis. The model predicts the physical structure of the gas discharge obtained between two electrodes, when one is covered with a dielectric material: It predicts the distribution of the electron and ion particle densities, electron energy, and electric field strength. It is a self-consistent numerical model, in which the dielectric properties of the dielectric material are included and the geometry of the electrodes is taken into account, thus coupling the charged-particle transport to the electric field.

New boundary conditions are developed for the electron gas at the anode; the results indicate that the common boundary conditions frequently used in the literature give solutions with non-physical behavior. The new boundary conditions give solutions with the expected physical behavior.

The equations of the model are formulated numerically using a Galerkin finite element method and solved using the Newton iteration method. New universal matrices for the finite element method are presented which can be used to construct complex finite element matrices, by replacing integrals with matrix products, in a consistent and uniform manner independent of element shape, dimensionality, and order.

Solutions for DC, pulse-waveform and time-harmonic applied electrode voltages for geometries with and without a dielectric barrier are presented. The regulating effect of the dielectric barrier by surface charge accumulation is shown for discharge under constant applied voltage, assuming a static temperature for the electron gas, for the full self-consistent model. Also, simulations of dielectric barrier discharge with applied pulse-waveform voltages are compared with simulations of applied time-harmonic voltages. The results show very similar period-averaged electric fields, electron temperature profiles, charged particle densities, and total conduction current densities. However, a much higher period-integrated ionization rate is obtained from voltage pulse simulations, compared to time-harmonic voltage simulations. Therefore, we obtain a greater reaction rate for an equivalent conduction current, in a period-averaged sense, for a discharge driven by pulse-waveform applied voltages than with time-harmonic applied voltages. Such a difference was not observed for simulations without the dielectric barrier.

Résumé

Un modèle de type fluide pour décharge éléctrique avec barrière diélectrique est présenté dans cette thèse. Le modèle prédit la structure physique de la décharge obtenue entre deux électrodes dans un gaz, une pouvant être couverte d'un matériel diélectrique. Le modèle calcule la distribution de la densité des électrons et des ions, l'énergie des électrons ainsi que le champ électrique. C'est un modèle cohérent dans lequel les propriétés diélectrique de la barrière diélectrique sont prisent en compte ainsi que la géométrie des électrodes, couplant ainsi le mouvement des particules chargées au champ électrique.

De nouvelles conditions aux limites pour le gaz des électrons à l'anode a été développées. Les résultats démontrent que les conditions couramment utilisé dans la littérature donne lieu à des solutions ayant des comportements physique injustifiable. Les solutions obtenues avec les nouvelles conditions aux limites ont les propiétés physique attendue.

Les équations du modèle sont résolues numériquement par la méthode des éléments finie de Galerkin avec la méthode iterative de Newton. De nouvelle matrices universelle sont développées pour la méthode des éléments finie est présenté permettant la construction des matrices d'élément finie complèxe en remplaçant les intégrales par des produits de matrices de façon cohérant et uniforme indépendant de la forme, la dimension et de l'ordre polynômial des éléments.

Des solutions du modèle pour cas avec courant continue et cas avec voltage aux électrodes dépendant du temps appliqué sous forme harmonique et pulse répétés sont présentées pour des géométries avec et sans barrière diélectrique. L'effet de régulation de la barrière diélectrique par accumulation des charges sur la surface de la barrière est obtenue pour des décharges à courant continue dans deux cas, l'un en supposant que les électrons ont une température statique et l'autre pour le modèle complet. De plus, des simulations comparées pour cas avec voltage appliqué de façon harmonique et en forme de pulses répétés sont présentées. Nous obtenons des résultats similaire pour le champ électrique, la température des électrons, la distribution des particules ainsi que le courrant total de conduction moyenné sur une période. Par contre, un plus grand taux d'ionization, intégré sur une période, est obtenue pour les simulations avec le voltage appliqué en forme de pulses. Par conséquent, nous obtenons un plus grand taux de réaction pour un courrant de conduction équivalent, de façon moyenné, pour les décharges avec un voltage appliqué en forme de pulses répétés comparativement au cas où le voltage est appliqué de façon harmonique. Cette difference n'a pas été observée pour les décharges n'ayant pas de barrière diélectrique.

Acknowledgements

When I started my Ph. D. graduate studies at McGill University in January 1991 I was, at the same time, a software consultant for Ozonics Systems Inc., renamed Corona Technologies in 1993. One of the two original entrepreneurs, David Fletcher, spontaneously said that I should develop a numerical model to help them design their air purification system for food storage. After reviewing some literature on the subject I realized that it was a very challenging offer.

I would like to thank the NSERC Collaborative Research and Development Grant (CRD) program which made possible a collaboration between Ozonics System Inc. and McGill University in 1992 to 1994 (contract NSERC 661-043/91), under which the mathematical formulation and its validation was carried out. Prior to that collaboration I received financial assistance from the Centre de Recherche Informatique de Montréal (CRIM) for which I am very grateful.

Corona Technologies Inc. created a wholly owned research and development subsidiary called FE2000 Inc. which obtained a major development RDA grant from the National Research Council (NRC), Project 14205Q, for which a major part of the analytic basis of the proposal was based on work resulting from the collaboration between Ozonics Technology Inc. and McGill University. I would like to thank Michel Éthier of NRC for his help during the technology transfer process.

I would like to thank David Fletcher and Barry Welford of Corona Technologies Inc. who believed in the industrial and commercial applications of such an abstract numerical model. I am very grateful to David Fletcher who gave

me the opportunity to participate in the commercialization of a new technology while carrying out research and development duties.

I would like to thank and express my gratitude to Professor Silvester who was my thesis supervisor until he passed away in October 1996. His academic rigor and his results-oriented approach made possible the development of a mathematically complex project with direct industrial applications. He was supportive until the last moment. I am very grateful to Mrs. Silvester who, despite the very difficult moments she went through, found the strength to encourage me to complete the present work.

I would like to thank Professor McFee who kindly offered to become my thesis supervisor after Professor Silvester passed away. I appreciate enormously his ability to jump right in the water and pick up the lead where Professor Silvester left it.

I would like to thank Professor Gitzhofer of the CRTP of the University of Sherbrooke, Professor Chaker INRS attached to UQUAM University, and Dr. Robbins of Draper Laboratory for very fruitful discussions relating theory to experiments during the FE2000 project. I would like also to thank my friends and colleagues from FE2000 Inc. and the CADLAB.

Finally I would like to thank my family, especially my Mother, my Father, and my sister Natalie, and also close friends Stephane and Sylvain for their moral and sometimes financial support which made the "student life" not so difficult for me. Many thanks to my girlfriend Diane who proof read the manuscript and for her friendship.

Contents

Abstract iii

Résumé v

Acknowledgements vii

1 Introduction 9

- 1.1 Definition of non-thermal plasmas 11
  - 1.1.1 Motivations and objectives of this thesis 13
  - 1.1.2 Contributions of this thesis to advancement of knowledge 17
- 1.2 Modeling non-thermal plasmas 17
  - 1.2.1 Kinetic models 18
  - 1.2.2 Monte Carlo and PIC/CIC simulation methods 23
  - 1.2.3 Continuum models 26

2 The equations of the model 33

- 2.1 The Boltzmann equation 34
  - 2.1.1 Hydrodynamic equations 35
- 2.2 Two-fluid model equations 38
  - 2.2.1 Transport coefficients 38
  - 2.2.2 Plasma model 42
  - 2.2.3 Plasma-electrode boundary conditions 44
  - 2.2.4 Plasma-dielectric barrier boundary condition 48
- 2.3 Non-dimensional form of the model's equations 51
  - 2.3.1 Boundary conditions 54

3 Finite element formulation of the model **57**
3.1 Weighted residuals of the model's equations 57
3.1.1 Surface terms of the residuals 60
3.2 Universal matrices for an n-dimensional element 62
3.2.1 Universal matrices 63
3.2.2 Integrals on surfaces 74
3.3 Weighted residuals using universal matrices 77
3.3.1 Surface terms using universal matrices 79
3.4 Time domain solution 81
3.4.1 Validation of the method 84
3.4.2 Stability and convergence criteria 85
3.4.3 Space-time integration of the residuals 86
3.4.4 Newton's method for nonlinear equations 87

4 Results **89**
4.1 Validation of the formulation 92
4.2 Geometry without dielectric barrier 100
4.2.1 DC solution 100
4.2.2 Simulations with new boundary conditions at electrodes . 107
4.2.3 Time-dependent discharge case 112
4.3 Geometry with dielectric barrier 126
4.3.1 DC solution 126
4.3.2 Charge accumulation on dielectric barrier for electron fluid with a static temperature case. 137
4.3.3 Charge accumulation on dielectric barrier, full model. . . 141
4.3.4 Time-dependent discharge case 149

5 Conclusion and summary **163**

Bibliography **177**

List of Tables

2.1 Plasma parameters for discharge space region with their units. . 42
2.2 Plasma kinematic parameters at electrodes and dielectric barrier boundaries with their units. 51
2.3 Plasma scaling factors with their units. 52
2.4 Dimensionless variables characterizing the plasma with their definitions. 53
2.5 Dimensionless ratios used in plasma equations with their definitions. 54
2.6 Dimensionless ratios used for the boundary conditions with their definitions. 55

3.1 Node numbering for the line element. 68
3.2 Node numbering for the triangular element. 70
3.3 Node numbering for the tetrahedral element. 73
3.4 Lookup tables for triangle element contour integral 75
3.5 Lookup tables for tetrahedral element surface integral 76

4.1 Gas discharge parameters used to obtained simulation results. . 92
4.2 Plasma scaling factors used to obtain simulation results. 93

List of Figures

1.1 Geometry of electrode system model and plasma regions 13

2.1 Definition of the unit vector normal to the surface enclosing the plasma. 50

3.1 Transformation from global coordinate system to local coordinate system for triangular element. 65
3.2 Typical spatially one-dimensional element. The element size is L; a_0 and a_1 are the end points of the element; x_1 and ξ_1 are the geometric and simplex coordinates respectively. 68
3.3 Typical triangular element. 69
3.4 Typical tetrahedral element. 72
3.5 Space-time discretization, spatially one-dimensional case. 83
3.6 Space-time discretization for spatially two-dimensional case. . . . 84

4.1 Charge densities and electric field, photoionization case, Figure 7 of Wardlaw and Cohen 97
4.2 Charge densities and electric field, photoionization case, Figure 8 of Wardlaw and Cohen 98
4.3 Charge densities and electric field, photoionization case, Figure 9 of Wardlaw and Cohen 99
4.4 Electron and ion densities, DC case. 101
4.5 Electric potential and electric field, DC case. 102
4.6 Electron temperature and ionization rate, DC case. 103
4.7 Electron and ion flux densities and total conduction current, DC case. 105

4.8 Drift and diffusion contributions to the electron and ion flux densities, DC case. 106

4.9 Electron heat flux density and electron and ion Joule heating, DC case 108

4.10 Electron temperature at anode, DC case. 109

4.11 Electric Field at anode, DC case. 110

4.12 Effect of electron temperature on electron conductivity coefficient, DC case. 111

4.13 Electron heat flux at cathode, DC case. 112

4.14 Electric potential applied at the cathode. 113

4.15 Total (electron plus ion) conduction current density at the cathode. 114

4.16 Electric field and electron temperature at different times in the period, pulse case. 115

4.17 Electron impact ionization rate at different times in the period, pulse case. 116

4.18 Electron flux density at different times in the period, pulse case. 117

4.19 Period-averaged electric field and Period-integrated electron impact ionization rate, pulse case versus harmonic case. 118

4.20 Period-averaged electric field and electron temperature, pulse-waveform cases. 119

4.21 Period-integrated electron impact ionization rate, pulse-waveform cases. 120

4.22 Period-averaged electron and ion Joule heating densities, pulse-waveform cases. 121

4.23 Period-averaged electron flux density and total conduction current density, pulse-waveform cases. 123

4.24 Total conduction and displacement current densities at different times in the period, pulse-waveform case. 124

4.25 Total current density at different times in the period, pulse-waveform case. 125

4.26 Electric potential, DC case with a dielectric barrier. 127

4.27 Electric field, DC case with dielectric barrier. 129
4.28 Electric field, DC case with dielectric barrier, full model. 129
4.29 Electron and ion charge densities, DC case with a dielectric barrier. 130
4.30 Electron temperature, DC case with a dielectric barrier. 131
4.31 Electron impact ionization rate, DC case with a dielectric barrier. 132
4.32 Electron and ion flux densities, DC case with a dielectric barrier. 133
4.33 Drift and diffusion contributions to the electron flux, DC case with a dielectric barrier. 134
4.34 Total conduction current, DC case with a dielectric barrier. . . . 134
4.35 Electron heat flux density, DC case with dielectric barrier. . . . 135
4.36 Electron and ion Joule heating, DC case with a dielectric barrier. 136
4.37 Electric field for charge accumulation on the dielectric barrier. . 137
4.38 Ion surface density accumulating on the dielectric barrier. 139
4.39 Electron density as charges accumulate on the dielectric barrier. 140
4.40 Electron surface charge accumulation on the dielectric barrier. . 140
4.41 Ion flux density as charges accumulate on the dielectric barrier. . 142
4.42 Electron flux density as charges accumulate on the dielectric barrier. 142
4.43 Electron and total conduction current density as charges accumulate on the dielectric barrier. 143
4.44 Electric field for charge accumulation on the dielectric barrier. . 144
4.45 Ion surface charge accumulation on the dielectric barrier. 144
4.46 Electron temperature and electron impact ionization rate as charges accumulate on the dielectric barrier. 146
4.47 Electron heat flux density as charges accumulate on the dielectric barrier. 147
4.48 Ion flux density as charges accumulate on the dielectric barrier. . 148
4.49 Electron and total conduction current densities as charges accumulate on the dielectric barrier. 148
4.50 Electric field at different times in the period, pulse case with a dielectric barrier (ϵ_r=5). 149

4.51 Electron impact ionization rate at different times in the period, for the pulse-waveform voltages with a dielectric barrier (ϵ_r=5) case. 150
4.52 Electron temperature at different times in the period, for the pulse-waveform voltages with a dielectric barrier (ϵ_r=5) case. . . 151
4.53 Period-averaged electric field and electron temperature, for geometry with a dielectric barrier, pulse-waveform case versus time-harmonic case. 152
4.54 Period-integrated electron impact ionization rate, for geometry with a dielectric barrier, pulse-waveform case versus time-harmonic case. 153
4.55 Period-averaged total current density, for geometry with a dielectric barrier, pulse-waveform case versus time-harmonic case. 154
4.56 Period-averaged electron Joule heating density, for geometry with a dielectric barrier, pulse-waveform case versus time-harmonic case. 154
4.57 Period-averaged electric field and electron temperature, for geometry with a dielectric barrier, pulse-waveform case. 155
4.58 Period-integrated electron impact ionization rate, for geometry with a dielectric barrier, pulse-waveform case. 157
4.59 Period-averaged total conduction current density, for geometry with a dielectric barrier, pulse-waveform cases. 157
4.60 Period-averaged electron and ion Joule heating densities, for geometry with a dielectric barrier, pulse-waveform case. 159
4.61 Total conduction and displacement current densities at different times in the period, pulse-waveform case with a dielectric barrier. 160
4.62 Total current density at different times in the period, for the pulse-waveform case with a dielectric barrier. 161

5.1 Inclusion of the developed physical model into a plasma chemistry model. 165

Chapter 1

Introduction

Applications of non-thermal plasma technology (NTPT) are important and diverse in today's world. One of the most important applications of low pressure radio frequency (RF) glow discharge is in the microelectronics manufacturing industry. Graves [1] pointed out that up to 30% of all process steps in the manufacturing of integrated circuits involve plasmas in one way or another. This is quite significant considering the large capital investment in sophisticated equipment required in a semiconductor plant. As an example, Advanced Micro Devices Inc., of Sunnyvale California, announced on December 14, 1996 [2] that it would build a $1.9 billion semiconductor plant in Dresden, in eastern Germany.

Further, the ability of the plasma etching process to remove material vertically, or anisotropically, during the silicon etching process made possible the reduction of features that would be otherwise unattainable with liquid etchants. In the early 1970's the minimum feature dimension of a chip was about 6 μm, on July 9, 1996 Lucent Technology Inc., of Murray Hill, New Jersey, announced [3] that it had developed an electron-beam system, called Scalpel, that can be used to create circuits with 0.08 μm features.

Corona discharge and dielectric barrier gas discharge processes were used as early as the 1850's by Siemens to generate ozone. It is still one of the most important applications of the gas discharge process at or near atmospheric pressure, see the review paper of Eliasson and Kogelschatz [4]. Other applications, which continue to attract a growing interest from industry, academia, and government laboratories, are the uses of these techniques for reducing or eliminating nitrogen oxides and sulfur dioxide in flue gases [5, 6], and volatile organic compounds (VOCs) in industrial effluents [7], which are important sources of environmental pollution. Many papers in the proceedings of the NATO Advanced Research Workshop on Non-Thermal Plasma Techniques for Pollution Control, edited by Penetrante and Schultheis [8], report on recent advances in these areas.

In the purpose and goals statement of a recent workshop on the treatment of gaseous emissions via plasma technology organized by NIST [9], it was stated:

> Plasma processing is an important step in manufacturing, and is emerging as a means for controlling emissions and a method for remediation. Plasma characterization (theoretical, computational, and experimental) has progressed significantly in recent years. Pilot plant facilities for treatment of gaseous emissions have been built to test the scale-up, efficiency and reliability of certain devices in the field. Yet, a significant limitation to including plasma technologies in environmental, safety, and health strategies is the lack of a fundamental understanding of plasma chemistry and engineering. As a consequence, there is an inability to predict the performance and cost effectiveness of a given plasma reactor for new applications [9].

This thesis reports on the development of a computational model for predicting the physical structure of the gas discharge obtained between two conducting parallel plates (electrodes) supporting an applied voltage difference. One of the plates may be covered with a dielectric material. The model predicts the distribution of the electron and ion particle densities, electron energy, and electric field strength. This is a self-consistent numerical model, in which the dielectric properties of the dielectric material are included and the geometry of the electrodes is taken into account, thus coupling the charged-particle transport to the electric field.

1.1 Definition of non-thermal plasmas

We consider the formation of a plasma by ionization of a gas by electron impact. An applied electric field is used to accelerate free electrons between collisions with the gas molecules; the electrons will ionize the neutral molecules when their energy attained is greater than the ionization energy. Upon ionization, one more free electron is released which will also gain energy from the field and ionize additional molecules. This is commonly termed a Townsend avalanche and results in an exponential multiplication of the current, see the textbook of Kuffel and Abdullah [10]. If the energy of the electron is insufficient the molecule may transit to an excited state, if such a state exists, or break up may occur to produce chemically active species (radicals). In turn, these excited molecules and radicals will involve themselves in chemical reactions. These are the only non-elastic processes considered in the model. All other collisions are assumed to be elastic and the gas behavior is assumed to be describable by the Boltzmann transport equation, see chapter (2).

Since the mass of the ions is a few thousand times the mass of the electrons, the electrons do not lose significant energy during elastic collisions. On the other hand, the ions also gain energy from the applied electric field and transfer energy during elastic collisions with the background gas, thereby increasing the temperature of the gas. However, when the ions collide with the gas molecules they generally are unable to raise the molecules to an excited state and, therefore, are incapable of promoting significant chemical reactions. Consequently, the ion current does not contribute to the chemical reaction process, but wastes power by heating the gas.

By considering the electrons and the ions as gases, one may define a temperature indicating the mean kinetic energy of the electrons and mean total energy of the ions. The average temperature of the electron gas may be as high as 10 thousand degrees Kelvin while the ions stay in thermal equilibrium with the neutral species which is close to room temperature. Therefore a gas discharge process can provide high-temperature chemistry at low gas temperature. This feature yields the term non-thermal plasma induced chemistry.

The population of charged particles in the bulk space between the electrodes will grow not only by ionization through direct electron impact, but also by secondary electron emission at the cathode, or at the dielectric barrier covering the cathode, due to ion impact. When an ion is accelerated by the electric field and hits the cathode or the dielectric barrier with sufficient energy to extract two electrons from the surface, one is used to neutralize the ion while the second is released into the inter-electrode space. Rapidly the inter-electrode space can be filled with ions and electrons which produce their own fields, which oppose the applied electric field.

The plasma will stabilize when the field produced by the separation of charges reaches the same magnitude as the applied field. At that moment, the charges will begin to move freely, which is a principal characteristic of a plasma. One might think that all the ions and electrons will recombine in the bulk space causing the plasma to collapse. This is not the case because a positive ion is made up of a positive nucleus surrounded by a cloud of electrons. At relatively larger distances, electrons see the net positive charge of the ions. As an electron gets closer, it starts to distinguish the electron cloud which screens the positive nucleus. Once close enough, the incoming electron will be repelled by the electron cloud. For recombination to occur in the bulk space, the incoming electron must have sufficient kinetic energy to overcome the Coulomb barrier. The minority of electrons having such energy are more likely to hit a neutral molecule and ionize it, rather than encounter another minority species such as a positive ion.

The ionization rate in the cathode sheath, where the applied electric field exists, will compensate for the losses due to recombination and diffusion. The electrons, having a much higher mobility than the ions, will diffuse out of the bulk gas space before the ions, leaving them behind. This charge separation will create a local electric field in the anode sheath which will retard the electron diffusion while accelerating the ion diffusion. Ambipolar diffusion takes place when both, electron and ion, diffuse at the same rate. Figure 1.1 shows the electrode geometry considered in this thesis and the various regions characterizing the plasma.

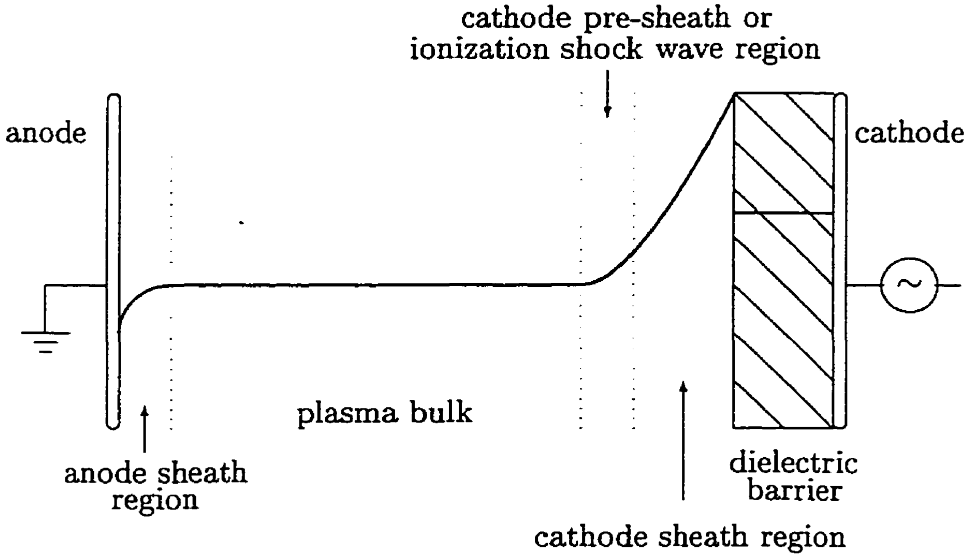

Figure 1.1: Geometry of electrode system model and plasma regions: electrode sheaths, ionization shock wave region, and plasma bulk. A typical electric field distribution is drawn (magnitude only), note the discontinuity at the plasma-dielectric barrier interface

1.1.1 Motivations and objectives of this thesis

The research reported in this thesis was motivated by the lack, in the open literature, of a self-consistent numerical model for dielectric barrier gas discharge which integrates the effect of the dielectric barrier on the discharge characteristics.

The principal component of the mathematical model consists of four coupled equations: electron and ion (positively charged only) continuity equations, Poisson's equation, and the electron energy equation. From a simultaneous solution of these equations, subject to the appropriate boundary conditions at the electrodes and interface conditions at the dielectric barrier, we obtain, respectively, electron and ion densities, electric potential, and electron temperature. Electric field strength, particle fluxes, surface charge accumulation on the surface of the dielectric barrier, ionization and molecule dissociation rates, etc., can then be derived from the solution. These quantities can be determined as functions of position in the discharge gap and, in the case of a periodic discharge, as functions of time in the period.

The aim of this research was to develop the mathematical model, and its implementation in computer software, to be used as a design tool for parametric studies leading to the development of energy efficient devices, and to optimize desirable chemical processes induced by the discharge. Therefore, the emphasis was on the "problem solving" aspect of the research rather than studying a particular application. Applications of this model include:

- Low pressure to medium pressure (below atmospheric) glow discharge for material (polymer) surface alteration.
- At or near atmospheric dielectric barrier discharge for air remediation. Modeling the global plasma remediation reactor.
- Non-equilibrium fluid model for streamers, providing a self-consistent coupling between the streamer and the dielectric barrier.

To our knowledge, the only dielectric barrier discharge that explicitly considers the properties of the dielectric material is the model used by Eliasson and Kogelschatz [11]. In their formulation they did not consider the ionic movement and assumed the electron gas to be in local thermal equilibrium with the electric field. Furthermore, their model addresses the formation of a single streamer rather than being a global model for the device under study.

Other streamer-based models exist in the literature, however they do not take into consideration the dielectric barrier in a self-consistent fashion. Gentile and Kushner [12] developed a plasma chemistry model that includes a dielectric barrier discharge module in which the coupling between the barrier and the plasma is represented by a circuit model. Li, Sun, Pashaie, and Dhali [13] developed a fluid model for dielectric barrier gas streamers assuming a very high dielectric permittivity such that the potential drop in the dielectric is small and therefore neglected altogether inside the dielectric. Other researchers have done likewise, e.g., Guo and Wu [14] and Naidis [15].

It is well established that the dielectric barrier is key to the proper functioning of the discharge and our results show that the effect of the dielectric barrier on the electric field distribution in the cathode fall region is important, even for the case when the potential drop is not significant in the barrier. In turn, this results in a considerable effect on the ionization rate and, as a consequence, the discharge behavior throughout the discharge space.

By its nature, dielectric barrier discharge is inhomogeneous due to the formation of many random micro-discharges. To this extent, the barrier has two functions: it limits the amount of charge transported by a single discharge, and evenly distributes the micro-discharges over the entire electrode area. When the discharge is in steady state, the discharge volume is occupied evenly by the streamers. Since at near atmospheric pressure there is no significant radial diffusion of the streamers, we assume that no important mechanism is neglected by considering a one-dimensional model and representing the discharge as a homogeneous plasma.

Naidis [15] developed a model for streamer propagation in a wire-plate configuration for pulse corona discharge that considers the interaction between streamers propagating simultaneously. The results obtained taking streamer interaction into account are in better accordance with experimental data than the values calculated in the single-streamer case. However, the calculated values of the streamer velocities are two or three time greater than those obtained experimentally. Therefore, it is not clear whether or not streamer interaction plays a significant role in streamer dynamics.

The assumptions made in the development of the mathematical model presented in this thesis are:

- **Gas is weakly ionized.** Only collisions between charged particles and neutral molecules are considered.

- **Heavy ions and background gas are at room temperature.** The ions are in thermal equilibrium with the background gas by elastic collision.

- **Charged particles are treated collectively as a fluid.** The gas pressure is sufficiently high to treat the electrons and the ions as two distinct fluids.

- **Electron has a near Maxwellian distribution function.** The electron mean free path is small enough compared to the device size to smooth out the anisotropy in the velocity distribution. A small mean free path permits the use of a continuum description for the electrons. In the cathode fall region it is expected that the electron distribution function will not be Maxwellian. To remedy to this shortcoming the model can be coupled to a Boltzmann solver to compute kinetic coefficients as functions of electron temperature.

- **The only external force is the electric field.** No magnetic field is considered in the Lorentz force.

- **The dielectric barrier is a dielectric of class A.** we consider the permittivity to be constant and uniform. However, the numerical methods used permit spatially inhomogeneous and field-dependent permittivities.

- **Assume uniform discharge.** Assume the discharge is uniform in the plane parallel to the electrodes. This allows a spatially one-dimensional formulation. We developed a finite element formulation using universal matrices such that the expressions for the residuals are independent of element dimensionality and order. Therefore it should be straightforward to extend the model to two and three spatial dimensions.

1.1.2 Contributions of this thesis to advancement of knowledge

The contributions of this thesis to advancement of knowledge are:

- **Finite element formulation using universal matrices.** New universal matrices for non-linear problems were developed.

- **Self-consistent dielectric barrier discharge model.** A fundamental understanding of the role of the dielectric barrier in the discharge process was developed. A self-consistent formulation that integrates the dielectric properties of the barrier into a fluid model that predicts charged particle densities, electric potential, and electron temperature was developed. New results showing the regulating effect of the dielectric barrier on the discharge process were established.

- **Improved boundary conditions for the electron gas at anode.** Most similar models in the literature use incorrect boundary conditions for the electron gas. Solutions obtained with the new boundary conditions do not exhibit the otherwise observed non-physical behavior reported in the literature.

- **Complete geometric model of the plasma device.** Provided a macroscopic analysis of the device under study based on a simultaneous solution of the model's equations (in opposition to an iterative decoupled solution).

1.2 Modeling non-thermal plasmas

A complete description of the physical processes involved in a partially ionized gas plasma would require the solution to the Boltzmann transport equation for each species of particles and the Maxwell equations for the applied and self-consistent electric and magnetic fields. Using such a model would be a formidable task and may exceed today's computer power when it is necessary to include sufficient geometrical details to give useful information for plasma device design improvements.

Assumptions and simplifications must to be made in order to obtain a model for practical use. Three options are presented to the researcher. One consists of keeping a kinetic description for one particle species, generally the electron, while assuming a given distribution function for the other species. Further, the region containing the plasma is traditionally divided into three regions: the anode and cathode sheaths, and the bulk region. The modeling is often restricted in one of the regions. These models are reviewed in section 1.2.1.

Another option consists of simulating a representative ensemble of particles of each species to obtain their distribution functions under given conditions. This approach is reviewed in section 1.2.2.

Finally, the continuum models, reviewed in section 1.2.3, use a semi-phenomenological description of the particles' interactions to obtain global plasma properties. Such macroscopic models may be tailored to support the model's equations for the properties of interest.

In a recent analysis, Verboncoeur, Parker, Penetrante, and Morgan [16] compared electron-neutral collision rates obtained from simulation methods and from solving the Boltzmann equation. They report good agreement between the two methods over a wide range of parameters of interest in discharge physics.

1.2.1 Kinetic models

Kinetic models consist of solving the Boltzmann equation, see section 2.1, for the particle species of interest, in general the electron. The nature of this approach is microscopic; the space and time scale of a collision process, as well as distribution function relaxation length and time, are much smaller than the characteristic spatial and temporal scales defined by the smaller of the plasma size and the inhomogeneity scale of the field, and by the driving frequency of the field.

Rockwood [17] developed a time-dependent numerical technique to solve the DC Boltzmann equation to compute the electron distribution function in a partly ionized gas under a given reduced field E/N. The electron velocity distribution function is expanded using the first two terms of a spherical harmonic expansion to account for a small anisotropy. This technique is commonly used to compute electron transport coefficients and electron impact collision reaction rates for the bulk region of the plasma from cross section data. The cross section data are known more or less precisely because of the presence of numerical or experimental errors. Esposito, Colonna, Longo, and Capitelli [18] developed a sensitivity analysis of the Boltzmann equation in the two-term approximation on changes in the cross section data.

Thompson, Smith and Davies [19] developed the BOLTZ computer code implementing a time-independent version of the Rockwood's technique to compute electron transport coefficients and electron vibrational excitation rates of CO_2. The obtained coefficients and rates were used as input data for a kinetic code of a CO_2 laser-produced plasma.

Morgan and Penetrante [20] have implemented the fully time-dependent Rockwood's technique in a computer program called ELENDIF. The computer program computes the time evolution of a given initial electron distribution function under constant electric field. Using the computed distribution function for the electron, the program computes the electron mean energy, drift velocity, diffusion coefficient transverse to the electric field, and rate coefficients. Feoktistov, Popov, Popovicheva, Rakhimov, Rakhimova, and Volkova [21] solved the Boltzmann equation in the two-term expansion approximation to obtain the electron transport coefficients for discharge in He, and then used these coefficients in continuity equations for the electron and ion particle distributions in conjunction with the Poisson equation for the self-consistent electric field. A similar approach was used by Ferreira, Alves, Pinheiro, and Sa [22] to model low-pressure microwave discharge in Ar, He, and O_2, and by Capitelli, Colonna, Hassouni, and Gicquel [23] for discharge in a $H_2/H/CH_4$ gas mixture for diamond film deposition.

Capriati, Colonna, Gorse, and Capitelli [24] solved the Boltzmann transport equation using the same approximation to obtain analytical expressions for macroscopic electron parameters (rate coefficients, mobility and diffusion coefficients, and mean energy) as functions of the reduced field, metastable concentration, and degree of ionization. These relations were used in a fluid model by Capriati, Boeuf, and Capitelli [25] assuming that the electrons were in local thermal equilibrium with the electric field. However, one may express the macroscopic parameters as functions of the electron mean energy rather than the reduced field and drop the local equilibrium approximation.

The above mentioned approach assumed uniformity in the electric field, implying that the gas discharge properties can be determined using the local electric field. This local field approximation is not valid in the cathode sheath region due to the non-uniformity in the electric field. Aleksandrov and Kochetov [26] extended the two-term expansion of the electron distribution function method to solve the Boltzmann equation for a non-uniform electric field based on perturbation theory (for small non-uniformity).

An extensive analysis by Kushner [27] of the plasma-etching process of silicon and silicone oxide in C_nF_m/H_2 and C_nF_m/O_2 plasmas was done using calculated electron-impact reaction rates from the electron distribution function solution of the Boltzmann equation in a two-term approximation. These rates and neutral gas-phase reaction rates were used in kinetic rate equations and time-integrated from an initial gas mixture until a steady-state solution was reached. Gordiets, *et al* [28] used the same approach to model low pressure N_2–O_2 glow discharge.

Dielectric barrier discharge was modeled by Gentile and Kushner for the destruction of N_xO_y [12] and of perchloroethylene [29] from a gas stream. The model consisted of a circuit model to compute the (constant) reduced field, the Boltzmann equation to determine the electron distribution function given the reduced field, and a plasma chemistry model.

The two-term expansion of the distribution function is not valid in plasma sheaths, in particular in the cathode sheath, where a large reduced field and gradients exist. In the cathode sheath the electrons emitted by ion impact attain a large velocity and collisional equilibrium in the presence of the electric field is never reached. These electrons play an important role in the discharge process since the current resulting from collisional ionization of the gas eventually grows exponentially with distance.

These fast secondary electrons can be viewed as an electron beam entering the plasma bulk. Phelps, Jelenkovie, and Pitchford [30] investigated anisotropy effects in the cathode fall region by using, for the electron, a distribution function of a mono-energetic beam moving in the direction of the acceleration. This parametrized distribution function is substituted into the Boltzmann equation and the first three velocity moments over the velocity space are taken. The obtained equations are similar to the fluid equations with the difference that the peculiar velocity is negligible compared to the fluid mean velocity. This is valid only at very high reduced field. From these equations excitation and ionization rates are obtained from the cross section data.

Anisotropy effects in the cathode fall region, resulting from high E/N, can be considered by using more than two terms in the spherical harmonic expansion of the distribution function. Shankar and Jensen [31] use an expansion of the form

$$f(x, v, \theta, t) = \sum_{k=1}^{10} P_k(\cos\theta) f_k(x, v, t)$$

where $P_k(\cos\theta)$ is the Legendre polynomial of order k, see the textbook of Mathews and Walker [32], and $\cos\theta = v_x/v$ is the direction cosine of anisotropy. The directions of the position coordinate x and velocity coordinate v_x are aligned with the direction of the electric field. The Boltzmann equation is solved, using the above expansion of the distribution function, through an implicit upwinding Galerkin finite element method for two case studies, a collision-less electron beam and a cathode fall region of low pressure DC glow discharge in He assuming a known electric field distribution. The weighted average of the spherical harmonic expansion coefficients, using the obtained distribution functions as weight functions, was used as a measure of the anisotropy in the system. The evaluation of the first 10 averaged coefficients demonstrated that the electron distribution functions are very anisotropic in the regions close to the boundary, corresponding to 10% of the discharge space.

In a recent study, Loffhagen, Winkler, and Braglia [33] compared the electron distribution function obtained by solving the Boltzmann equation in a two-term and a eight-term expansion of the distribution function, and by a Monte Carlo simulation. Their results showed very good agreement between the eight-term Boltzmann approach and the Monte Carlo simulation.

Another approach to solving the Boltzmann equation is the so-called "convective scheme" of Sommerer, Hitchon, and Lawler [34], which is based on a propagator or Green's function method. In this method the integro-differential Boltzmann equation is replaced by an integral equation by the use of a propagator that advances the distribution function at time $t + \Delta t$ knowing the distribution function at time t. The method is described in the paper by Adams and Hitchon [35]. This convective scheme was used to obtain a self-consistent kinetic model of RF discharge in He by Sommerer *et al* [36]. The electron and ion distribution functions were obtained with a self-consistent electric field. The results yielded a low average electron energy in the bulk region, approximately 0.6 eV, compared to the often assumed value of ~ 1 eV in models which neglect the energy balance or continuity equation.

Uhrlandt and Winkler [37] investigated the radial structure of the electron kinetics in the DC column plasma (streamer). Their method consisted of solving the Boltzmann equation in the two-term approximation for a radially inhomogeneous electric field. This approach takes into consideration the non-local dependence of the electron kinetics on the electric field without the restriction of small non-uniformity required for the approach based on the theory of perturbations of Aleksandrov and Kochetov [26], and is computationally less demanding than the convective scheme, which is not based on a two-term expansion of the electron distribution function.

1.2.2 Monte Carlo and PIC/CIC simulation methods

Simulation methods place emphasis on the physical processes, at the particle level, involved in the plasma, such as particle collisions. These methods are based on simulating a representative ensemble of particles by successive integrations of their equations of motion (free flight under local resultant forces), following a collision. Particle collisions may be of two kinds: elastic and inelastic. Elastic collisions are simple in principle, but inelastic collisions open the door to many possibilities: composite incoming particles may leave the region of interaction in an excited state, break up may occur, or transition to a metastable state is possible.

The Monte Carlo method is based on simulating the stochastic movement of a particle in a gas by simulating collision events using a sequence of random numbers to determine the position and nature of each collision and the change in velocity due to the collision. The probability of a given collision type to occur is weighted according to its cross section relative to the total cross section of all processes. The Monte Carlo method applied to gas discharge is presented in the paper of Boeuf and Marode [38].

Tran, Marode, and Johnson [39] performed a Monte Carlo simulation of the electron behavior in the cathode fall region of a glow discharge in He. They studied in particular the ionization avalanche due to secondary electrons emitted by ion impacts assuming a linear relationship for the electric field. Their collision processes considered forward scattering only which reduced their analysis to a one-dimensional model. Angular scattering was included in a three-dimensional Monte Carlo simulation by Boeuf and Marode [38]. In these simulations the motion of the electrons leaving the cathode and their progenies were followed in the gap until their absorption by one of the electrodes.

Charged particle simulations consist of counting the number of particles between grid points and assigning the corresponding density to the cell center, some weighting function may be used, see the survey of Eastwood [40]. All the particles in a given cell are assigned the same resulting force, thus the name particle-in-cell (PIC). The particles can now be viewed as having a finite size, corresponding to the cell size, hence the name cloud-in-cell (CIC). Once the particle density is determined, integration of the Maxwell equations on the mesh yields the electromagnetic field in each cell. Given the new field values at the mesh nodes, the Lorentz force on all particles are computed. Integration of the equations of motion for a time step Δt, for each cell, gives a new density distribution. This process is iterated until a steady state is reached.

The PIC/CIC simulations are deterministic and valid for collision-less plasma. However, combining this technique with the Monte Carlo method to simulate statistical collisions between electrons or ions with the background gas to allow ionization and other processes yields a very powerful simulation method. See the review paper of Birdsall [41] and the monograph of Hockney and Eastwood [42].

Kushner [43] analyzed the electron properties in RF discharge in a parallel plate geometry using the Monte Carlo simulation method. In order to reduce the required number of simulated electrons the electric field was assumed to be known in the cathode sheath region. The results indicated that the electron distribution function has a low thermal energy group, corresponding to the electrons in the plasma bulk, and a high energy group resulting from the secondary electron emission from the cathode.

Vender and Boswell [44, 45] analyzed a similar discharge reactor using the PIC simulation technique. Their simulation computed the self-consistent electric field, however secondary electron emission was not included. The inclusion of secondary electron emission is problematic for simulation methods when the self-consistent electric field is computed. One needs to simulate a very large number of electrons to have an adequate estimation of the field in the sheath. Vender and Boswell [44] used 2 000 ion and electron pairs in their simulation while Surendra and Graves [46] used 12 000 to 400 000 pairs of particles to simulate a RF glow discharge with secondary electron emission and a self-consistent electric field.

The analysis of Surendra and Graves [46] investigated the differences between discharges sustained without secondary electron emission and discharge sustained by secondary electron emission. In the former case the discharge sustaining mechanism is sheath oscillation heating. Their results indicate that the average electron energy is nearly independent of the applied voltage for a given discharge condition, but increases sharply in the sheaths when secondary electron emission is significant.

Hybrid models may be used to overcome the difficulty of particle statistics when computing self-consistent fields for discharge with emitting electrodes. Sommerer and Kushner [47] developed a hybrid model incorporating a kinetic description of the electron distribution function, a self-consistent fluid description of the charge densities, and a neutral gas phase chemistry model to predict discharge by-products. In their formulation the electron distribution function is computed using a Monte Carlo simulation for a given electric field distribution. Electron transport coefficients and electron impact reaction rates as functions of the reduced electric field are then computed. These coefficients and rates are used in a fluid model which includes electron and positive ion continuity equations together with Poisson's equation for the electric field. The electrons are assumed to be in local equilibrium with the electric field. The computed electric field is to be used in the next run of the Monte Carlo simulation. The last module is the gas phase chemistry model which comprises the time-independent continuity equations for the chemical species of interest. The electron impact reaction rates obtained from the Monte Carlo simulation module are period-averaged since the transport of neutral particles has time scales that span many RF periods.

Wu, Li, Tsai, and Young [48] developed a hybrid model for RF discharge which computes the electron distribution function by solving the Boltzmann equation in which the collision term is modeled by the Monte Carlo flux method of Schaefer and Hui [49]. The transport coefficients and reaction rates are computed from the distribution function and used in a fluid model to compute the heavy ion and electric distributions, given the electron distribution obtained by the first moment of the electron distribution function. This model provides a temporal, spatially two-dimensional, and two-dimensional velocity resolution of the discharge.

The use of hybrid approaches permits partially decoupled modeling of the discharge process by using loosely coupled modules having very different characteristic space and time scales. This decomposition can provide an economical computation time for each module since the level of sophistication per module is reduced. However, by placing important nonlinear feedback mechanisms, such as the computation of the electric field distribution and the computation of the electron thermal energy, in different modules, one can considerably reduce the convergence rate towards a self-consistent solution. Further, a small error in the electric field distribution will produce a greater error in the electron kinetic energy, especially in the cathode sheath, which in turn will produce a much greater error in the reaction rates as a consequence of the exponential dependence of the reaction rate on the electron kinetic energy.

Other hybrid models are reviewed in the next section.

1.2.3 Continuum models

Continuum models use a semi-phenomenological approach in which the interactions are model dependent and not expressed in terms of the basic cross section of the underlying microscopic collision processes. Global plasma properties are obtained by averaging over the microscopic details of the particle interactions. Rather than computing spectral distribution functions for each particle species, which contain far more information than may be required, macroscopic models are tailored so that the model's equations target the properties of interest. The equations are in terms of the averaged plasma's constituent dynamics. The work of this thesis is in keeping with this approach.

The analysis of Ward [50, 51] on the cathode fall in gas discharge between parallel plates is one of the first analyses that computes the self-consistent electric field and particle distribution. In his analysis, particle diffusion is neglected and the electrons are assumed to be in thermal equilibrium with the electric field. The model is based on Townsend's basic ionization equation and

Poisson's equation. The Townsend theory of current multiplication is described in the monograph of Kuffel and Abdullah [10]. The ionization coefficients for discharge in various ideal gases, the so-called Townsend's first ionization coefficients, are expressed as analytical relations fitted to match experimental data.

Wardlaw and Cohen [52] analyzed the photoionization chamber using a continuum analysis based on the first moment of the Boltzmann equation for both the electron and ion gases, together with the Poisson equation for the self-consistent electric field. The photoionization chamber consists of a test gas confined by parallel conducting plates and ionized by means of UV radiation. The discharge process is not self-sustained by electron impact, therefore the assumption of a constant and uniform temperature for the electrons is not severe. In their analysis, the particle diffusion and the drift under the effect of the electric force is retained. Their results, obtained by a semi-analytic method, are reproduced in section 4.1. Recently, Pai, Guo, and Zhou [53] obtained an analytical solution in closed form to a similar continuum model describing a self-sustained glow discharge.

The study of the properties of the Langmuir probes yield a similar analysis of the electrical characteristics of the discharge process in weakly ionized gases. However the discharge sustaining mechanism is electron impact in the shock-layer formed near the conducting probe (the cathode fall region). Chung analyzed [54, 55] the non-equilibrium electron temperature in the shock layer and demonstrated that, according to kinetic theory, the electrons are completely out of equilibrium in the region near an absorbing surface.

A similar shock wave structure is observed in high voltage breakdown streamers. Albright and Tidman [56] analyzed the ionization shock wave formation in the breakdown of a dense gas in a strong electric field. This shock wave formation is analyzed in section 4.2.1. Their analysis is based on fluid equations for the electron gas, and the ionizing shock wave of the streamer is assumed to travel so rapidly that ions and neutrals do not have time to be heated before the wavefront has passed on. As a consequence, the ions are "frozen" in the background, and only the motion of the electrons is considered. They assumed the electron gas to be in thermal equilibrium with the electric field and a constant electron temperature was taken throughout the shock wave to obtain their numerical results.

Klingbeil, Tidman, and Fernsler [57] extended the analysis to include photoionization occurring at the streamer's head due to atomic excitation of the background gas to drop the constant electron temperature assumption. Graphical solutions of the equations are presented.

Abbas and Bayle [58] studied the ionizing shock wave formation and propagation using a fluid model for the electron and ion gases. They have shown, by studying the evolution of electron germ impulses, that the occurrence of a shock zone head associated with the discharge plasma is unavoidable. They report that the existence of this zone, defined by the presence of large gradients in particle densities and electric field distributions, results in a situation where the electron gas is out of equilibrium with respect to the electric field. Abbas and Bayle [58] and Bayle and Cornebois [59] obtained a numerical solution of a hydrodynamic model describing the propagation and evolution of a streamer's head. Their model consists of the particle number continuity equations for the electron and ion gases, Poisson's equation for the electric field, and the electron kinetic energy continuity equation. The numerical solution is obtained according to the following scheme. The initial electron and ion particle distributions and the electron temperature are assumed to be known (n_e, n_{ion}, and T_e). The electric field distribution is computed by solving the Poisson equation and the resulting electron velocity is obtained ($\boldsymbol{E}$ and $\boldsymbol{v}_e$). The time-evolution of the system is computed by updating alternatively n_e, n_{ion}, and T_e after a time step assuming $\boldsymbol{E}$ and $\boldsymbol{v}_e$ are unchanged and then using the new values of n_e, n_{ion}, and T_e to find better $\boldsymbol{E}$ and $\boldsymbol{v}_e$ estimates after the next time step.

This study of the transition between the insulating state of a gas to a conducting state by electrical breakdown is of practical interest for gas-filled voids or cavities found within solid insulators or in narrow slits between an insulator and a conductor. Novak and Bartnikas [60, 61, 62] studied such breakdown in narrow gaps using a two-dimensional fluid model in cylindrical coordinates which includes electrons, ions and metastable molecule particle continuity equations together with Poisson's equation. They computed the time evolution of an initial "burst" of electrons following an algorithm similar to the algorithm of Bayle and Cornebois [59] described above.

The applications of plasma chemistry in the microelectronics industry, for the deposition and etching of thin film, created a new fervor for the modeling of gas discharge devices of large scale compared to the shock wave region. Boeuf [63] analyzed the RF discharge occurring in a plasma reactor focusing on the physical aspect of the discharge. The model consisted of the continuity equations for the positive and negative ion and electron densities and the Poisson equation. The electrons were assumed to be in thermal equilibrium with the electric field which avoided the need for an energy continuity equation for the electron gas. The transport coefficients together with the ionization and recombination rates were functions of the local value of the electric field. The analytical relations obtained by Ward [50, 51] were used for the ions and the electrons.

To account for the non-equilibrium electron kinetics Graves and Jensen [64] and Park and Economou [65] added an electron temperature continuity equation to the particle number continuity equation and Poisson equation description of the plasma. This resulted in a self-consistent model of the discharge mechanism sustaining the plasma, however the electron and ion fluxes were modeled by the so-called drift-diffusion model which includes a field-driven term plus a gradient-driven term. As a result the stiffness of the model's equations is greatly increased, see section 4.2.1. To reduce the equations' stiffness Graves [66] used a constant and uniform electron temperature in the ionization term of the particle number continuity equations. However, the electron temperature continuity equation was retained in the model in order to resolve the distribution of the rate of molecule excitation by electron impact in the inter-electrode space. The well-posedness of Graves boundary conditions for the electron temperature continuity equation was questioned by Wilcoxson and

Manousiouthakis [67]; in this regard, new boundary conditions for the electron number and electron temperature continuity equation are presented in section 2.2.3.

Barnes, Cotler, and Elta [68] and Meyyappan and Kreskovsky [69], and recently Meyyappan, Govindan, and Kreskovsky [70] for two spatial dimensions, retained the first three moments of the Boltzmann equation for the electron gas description, which includes mass, momentum, and energy continuity equations. Only a mass continuity equation was used by Barnes *et al* for the ions with a drift-diffusion ion flux. Young and Wu [71] also analyzed the RF discharge using a three-moment fluid model for the electron gas in spatial two dimensions. Very few models in the literature actually simultaneously solve for the electron density, velocity, and temperature. In general the drift-diffusion model is used for the electron and ion fluxes.

As it will be discussed in section 2.2.1 we use the electron-impact ionization rate of Park and Economou [72], which is expressed as function of the electron temperature. The expression is a fit to the rate obtained by solving the Boltzmann equation. Many hybrid models were developed in which the electron transport coefficients and reaction rates are computed using a microscopic model, such as Monte Carlo or PIC simulations, or by solving the Boltzmann equation. The coefficients and rates obtained are used as input to fluid models to obtain a macroscopic description. These hybrid models are now reviewed.

Surendra, Graves, and Jellum [73] analyzed DC discharge with explicit treatment of the fast electrons in the cathode fall region. They used two approaches. One consisted of considering the fast electrons as a mono-energetic beam, and parametrized their distribution function as a delta function imposing the same velocity, at any given position, to all fast electrons. When the kinetic energy of the fast electron group drops below a threshold value in the plasma bulk they are shifted into the slow electron group. Belenguer and Boeuf [74] used this approach to analyze the RF discharge. Recently Bradley [75] developed a three fluid model for the cathode shock wave region in which the electrons, the ions, and the beam-like electrons are treated as separate fluids.

The second approach consists of a Monte Carlo simulation of the cathode fall region. Again, when the kinetic energy of the tracked electron drops below a threshold value the electron is transfered into the slow electron group. The slow electron group and the ion gas are modeled by mass conservation equations together with Poisson's equation.

Alternatively Pirooz, Ramachandran, and Abraham-Shrauner [76] and Nitschke and Graves [77] developed a hybrid model which decomposes the plasma reactor into two regions: the sheaths and the plasma bulk regions. Rethfeld, Wendelstorf, Klein, and Simon [78] also developed a similar model for the cathode fall region of an electric arc using three regions. The aim of this approach is to reduce the computational resources required to analyze a particular discharge condition. The structure of the plasma sheath, in particular the lack of electron equilibrium with respect to the electric field, has an important impact on the dynamics of the discharge throughout the plasma. This will be seen in chapter 4. The danger of such hybrid models is that important details may be lost in oversimplifying the coupling, or feedback, mechanism between the structure of the sheaths and the macroscopic properties of the plasma.

A hybrid Monte-Carlo and two-fluid model was used by Boeuf and Pitchford [79] for pseudospark discharge, which is a gas discharge mode characterized by an extremely rapid transition to a relatively high current density (arc mode). This approach was also used by Huang and Kushner [80] for DC discharge in N_2 and He/N_2. A Monte-Carlo simulation computes the electron and ion distribution functions from which transport coefficients and reaction rates are computed. These coefficients and rates are used in single-moment fluid models that compute electron and ion particle number densities and the electric field distribution.

Chapter 2

The equations of the model

A complete description of a plasma lies in the kinetic theory of matter. To develop a kinetic theory of matter, each particle species is described in terms of a distribution function $f(\boldsymbol{r}, \boldsymbol{v}, t)$ in a 6-dimensional phase space $(\boldsymbol{r}, \boldsymbol{v})$.

The meaning of the distribution function is such that $f(\boldsymbol{r}, \boldsymbol{v}, t)d\boldsymbol{r}d\boldsymbol{v}$ represents the probability of finding particles in the physical space defined by $\boldsymbol{r} \pm d\boldsymbol{r}$ having velocity $\boldsymbol{v} \pm d\boldsymbol{v}$ at time t. For the sake of generalization, one may speak of a fluid rather than a plasma, where the fluid is made of a collection of particles of different species. A plasma may be considered as a special fluid in which charged particles exist and move freely, i.e., the average electric and magnetic fields vanish in the plasma. However, localized fields due to charge separation over short distances may occur; but the charge separation may not be greater than a Debye's length.

For a more detailed description, the reader is referred to the textbooks of Boyd and Sanderson [81], Jancel and Kahan [82], or Shkarofsky and Johnston [83].

Various physical characteristics of the plasma, or the fluid, are obtained through various velocity moments of the distribution function:

particle density:	$n(\boldsymbol{r}, t) = \int_{-\infty}^{+\infty} f(\boldsymbol{r}, \boldsymbol{v}, t)d\boldsymbol{v}$,	zeroth order moment
momentum density:	$p(\boldsymbol{r}, t) = \int_{-\infty}^{+\infty} m\boldsymbol{v} f(\boldsymbol{r}, \boldsymbol{v}, t)d\boldsymbol{v}$,	first order moment
energy density:	$\mathcal{E}(\boldsymbol{r}, t) = \int_{-\infty}^{+\infty} \frac{1}{2}mv^2 f(\boldsymbol{r}, \boldsymbol{v}, t)d\boldsymbol{v}$,	second order moment
and so on...		

To lighten the notation the distribution function will simply be written as f. We may define the average velocity $\boldsymbol{u}(\boldsymbol{r},t)$, which is useful for determining macroscopic characteristics, as

$$\boldsymbol{u}(\boldsymbol{r},t) \equiv \frac{\int \boldsymbol{v} f d\boldsymbol{v}}{\int f d\boldsymbol{v}} \tag{2.1}$$

for the particle species described by the distribution function f.

2.1 The Boltzmann equation

The Liouville theorem stipulates that the distribution function is stationary in the phase space along the particle trajectory:

$$\frac{\delta}{\delta t} f(\boldsymbol{r},\boldsymbol{v},t) = 0. \tag{2.2}$$

The variation in f due to force, external and self-consistent, acting on the particle from the variation due to particle collision is treated separately;

$$\left(\frac{\mathrm{d}f}{\mathrm{d}t}\right)_F + \left(\frac{\mathrm{d}f}{\mathrm{d}t}\right)_c = 0. \tag{2.3}$$

The first term may be expanded to yield:

$$\frac{\partial f}{\partial t} + \boldsymbol{v} \cdot \boldsymbol{\nabla}_{\boldsymbol{r}} f + \frac{1}{m} \boldsymbol{F} \cdot \boldsymbol{\nabla}_{\boldsymbol{v}} f = \left(\frac{\mathrm{d}f}{\mathrm{d}t}\right)_c \tag{2.4}$$

where F is, in general, the Lorentz force $\boldsymbol{F} = q(\boldsymbol{E}+\boldsymbol{v}\times\boldsymbol{B})$ acting on the particle of charge q. The fields $\boldsymbol{E}(\boldsymbol{r},t)$ and $\boldsymbol{B}(\boldsymbol{r},t)$ are the electric and magnetic fields in the plasma respectively. This is known as the Boltzmann equation. The collision term, on the right-hand-side of equation (2.4), includes all elastic and inelastic collisions. In general, only a two-body term is retained, i.e., collisions involving only a pair of particles (of same species or not). The probability of three-body and higher-order collisions is much less. When no collision term is considered, equation (2.4) is known as Vlasov's equation.

2.1.1 Hydrodynamic equations

The Boltzmann equation is a 7-dimensional integro-differential equation. The solution of the Boltzmann equation specifies the distribution function of a particle species and is a microscopic description of the plasma. However, one can tailor a less accurate but simpler description of the plasma in terms of macroscopic quantities of interest such as particle number density, temperature and average velocity distribution in spatial coordinates and time. This description is known as the hydrodynamic equations of the plasma. Hydrodynamic equations are obtained for each particle species of a plasma by evaluating moments of the Boltzmann equation with respect to velocity $\boldsymbol{v}$.

If we define the weighted average of an arbitrary function $\phi(\boldsymbol{r}, \boldsymbol{v}, t)$ over the velocity space as

$$\langle \phi \rangle = \frac{1}{n(\boldsymbol{r}, t)} \int \phi(\boldsymbol{r}, \boldsymbol{v}, t)\, f d\boldsymbol{v}. \tag{2.5}$$

Then, taking the moment of the Boltzmann equation, equation (2.4), with a function $\psi(\boldsymbol{v})$ we get:

$$\frac{\partial}{\partial t}(n\langle\psi\rangle) + \boldsymbol{\nabla}_{\boldsymbol{r}} \cdot (n\langle\boldsymbol{v}\psi\rangle) - \frac{\boldsymbol{F}}{m} \cdot (n\langle\nabla_v\psi\rangle) = \left(\frac{\mathrm{d}}{\mathrm{d}t}(n\langle\psi\rangle)\right)_c \tag{2.6}$$

where we have interchanged the order of the differentiation and integration operators. Note that the force $\boldsymbol{F}$ is assumed to not depend on velocity (or at least $\boldsymbol{F}\cdot\boldsymbol{e}_i$ does not depend on $\boldsymbol{v}\cdot\boldsymbol{e}_i$, $\boldsymbol{e}_i$ being the coordinate unit vector in direction i in v-space), and integration-by-parts was performed on the last term on the left-hand-side followed by the use the divergence theorem assuming $f \to 0$ as $\boldsymbol{v} \to \infty$.

The particle number continuity equation is obtained by taking $\psi = 1$ in equation (2.6):

$$\frac{\partial n}{\partial t} + \boldsymbol{\nabla}_{\boldsymbol{r}} \cdot (n\boldsymbol{u}) = \left(\frac{\mathrm{d}n}{\mathrm{d}t}\right)_c. \tag{2.7}$$

Taking $\psi = m\boldsymbol{v}$ we get the momentum density continuity equation:

$$m\frac{\partial}{\partial t}(n\boldsymbol{u}) + m\boldsymbol{\nabla}_{\boldsymbol{r}} \cdot (n\langle\boldsymbol{v}\boldsymbol{v}\rangle) - \boldsymbol{F}n = \left(m\frac{\mathrm{d}}{\mathrm{d}t}(n\boldsymbol{u})\right)_c. \tag{2.8}$$

It is convenient to express the tensor $\langle \boldsymbol{v}\boldsymbol{v}\rangle$ as a combination of terms involving the local mean velocity $\boldsymbol{u}$ and the so-called peculiar velocity $\boldsymbol{w}$, which is defined as the velocity relative to $\boldsymbol{u}$ due to random motion, $\boldsymbol{w} = \boldsymbol{v} - \boldsymbol{u}$:

$$\langle v_i v_j\rangle = u_i u_j + \langle w_i w_j\rangle.$$

There are no cross terms since $\langle \boldsymbol{w}\rangle = \langle \boldsymbol{v} - \boldsymbol{u}\rangle = 0$.

The pressure tensor may be defined in terms of the peculiar velocity:

$$P_{ij} \equiv m\, n(\boldsymbol{r}, t)\langle w_i w_j\rangle \tag{2.9}$$

The elements of $\boldsymbol{P}$, P_{ij}, represent the force per unit area in the direction i on a plane normal to the direction j. The diagonal elements represent the normal force per unit area or the normal pressure on planes parallel to the coordinate system. The off-diagonal elements represent the shear forces on the same planes. The pressure exerted on the surface having normal $\hat{\boldsymbol{S}}$ is $\boldsymbol{p}_N = \hat{\boldsymbol{S}} \cdot \boldsymbol{P}$. The sum of normal pressures at a point is $\sum_i P_{ii} = nm\langle w^2\rangle$. The mean normal pressure acting on the three orthogonal planes parallel to the coordinate system is:

$$\frac{1}{3}\sum_i P_{ii} = \frac{1}{3} nm\langle w^2\rangle \equiv p(\boldsymbol{r}, t) \tag{2.10}$$

which is called the hydrostatic pressure at point ($\boldsymbol{r}$,t). We consider the velocity distribution function to be isotropic in $\boldsymbol{v}$, this is the case for a Maxwellian distribution function. In such cases the off-diagonal elements of $\boldsymbol{P}$ vanish, i.e., the pressure vector $\boldsymbol{p}_N$ is normal to the surface. Also, all diagonal elements are equal to the hydrostatic pressure p, therefore

$$\boldsymbol{P} = p\boldsymbol{I} \tag{2.11}$$

where $\boldsymbol{I}$ is the identity tensor.

Therefore, equation (2.8) may be recast as

$$mn\left(\frac{\partial \boldsymbol{u}}{\partial t} + \boldsymbol{u}\cdot\nabla_{\boldsymbol{r}}\boldsymbol{u}\right) + m\nabla_{\boldsymbol{r}}\cdot\boldsymbol{P} - n\boldsymbol{F} = \left(m\frac{\mathrm{d}}{\mathrm{d}t}(n\boldsymbol{u})\right)_c . \tag{2.12}$$

Note that equation (2.7) is used when the total number of particles of the species is conserved. The operator $\frac{\partial}{\partial t} + \boldsymbol{u} \cdot \boldsymbol{\nabla}_r$ is the convective derivative: the first term is the explicit variation in time while the second is the change due to the movement of the fluid.

The kinetic energy continuity equation is obtained by setting $\psi = \frac{1}{2}mv^2$ in equation (2.6):

$$\frac{\partial}{\partial t}\left(\frac{1}{2}nm\langle v^2\rangle\right) + \boldsymbol{\nabla}_r \cdot \left(\frac{1}{2}nm\langle v^2 \boldsymbol{v}\rangle\right) - n\boldsymbol{F}\cdot\boldsymbol{u} = \left(\frac{\mathrm{d}}{\mathrm{d}t}\left(\frac{1}{2}nm\langle v^2\rangle\right)\right)_c . \tag{2.13}$$

The temperature of a particle species may be defined as the kinetic energy due to peculiar motion:

$$\frac{1}{2}nm\langle w^2\rangle = \frac{3}{2}nkT \tag{2.14}$$

where k is the Boltzmann constant. The hydrostatic pressure, defined by equation (2.10), is

$$p = nkT. \tag{2.15}$$

Further, the heat flux due to peculiar motion may be expressed as:

$$\boldsymbol{q} = \frac{1}{2}nm\langle w^2 \boldsymbol{w}\rangle. \tag{2.16}$$

Therefore, by definitions (2.14) and (2.16):

$$\frac{1}{2}nm\langle v^2\rangle = \frac{3}{2}nkT + \frac{1}{2}nmu^2, \text{ and} \tag{2.17}$$

$$\frac{1}{2}nm\langle v^2 \boldsymbol{v}\rangle = \boldsymbol{q} + \frac{5}{2}nkT\boldsymbol{u} + \frac{1}{2}nmu^2\boldsymbol{u}, \tag{2.18}$$

whereby, substitution of (2.17) and (2.18) into (2.13) yields:

$$\frac{\partial}{\partial t}\left(\frac{3}{2}nkT + \frac{1}{2}nmu^2\right) + \boldsymbol{\nabla}_r \cdot \left(\boldsymbol{q} + \left(\frac{5}{2}nkT + \frac{1}{2}nmu^2\right)\boldsymbol{u}\right) = n\boldsymbol{F}\cdot\boldsymbol{u} + \left(\frac{\mathrm{d}}{\mathrm{d}t}\left(\frac{1}{2}nm\langle v^2\rangle\right)\right)_c . \tag{2.19}$$

This equation shows that the change of energy density, which includes the thermal kinetic energy due to peculiar motion, $3/2\, nkT$, and the kinetic energy of hydrodynamical motion, $1/2\, nmu^2$, is caused by the enthalpy flux, $(5/2\, nkT + 1/2\, nmu^2)\boldsymbol{u}$ and the heat flux $\boldsymbol{q}$. The terms on the right-hand-side, the power associated with the force density, $n\boldsymbol{F} \cdot \boldsymbol{u}$, and the collision term, act as a source or drain.

Equations (2.7), (2.12), and (2.19) are the hydrodynamic equations of a plasma for a single particle species. A corresponding set of equations exists for each particle species making up the plasma. However, these sets of equations are not closed because the three components of the heat flux vector $\boldsymbol{q}$ remain unknown, since they are determined by the next order moment of the Boltzmann equation. Assumptions have to be made to close these sets of equations. This will be the object of the next section.

2.2 Two-fluid model equations

A two-fluid model has been developed for gas discharge. In this model the plasma is represented as a mixture of an ionic and an electronic fluid. Since the model is developed for discharge near atmospheric pressure, the effects due to the peculiar velocity in the collision term of the momentum continuity equation, equation (2.12), may be neglected as the collisions tend to smooth out all anisotropy. Therefore, some terms in (2.12) may be replaced with the use of macroscopic kinetic coefficients, such as the diffusion and mobility coefficients of the particles. This simplification is well justified in the bulk of the plasma, but ignores the boundary effects in the momentum distribution.

2.2.1 Transport coefficients

The plasma is sustained by the application of a radio-frequency (RF) time-varying voltage at the electrodes, no magnetic field is applied. The Lorentz force reduces to $\boldsymbol{F} = q\boldsymbol{E}$, where q is the charge of the particle.

Since the level of ionization is low, the collision process is dominated by the two body electron-neutral collisions. Assuming that the collisions occur within infinitesimally small periods of time compared to any other macroscopic change in the plasma, we may write the momentum transfer between the electron and the heavy neutral molecule as:

$$-\nu_e \frac{m_e M}{m_e + M}(\boldsymbol{u}_e - \boldsymbol{u}_M) \simeq -\nu_e m_e \boldsymbol{u}_e \tag{2.20}$$

where m_e and M are the masses of the electron and the neutral molecule respectively; $\boldsymbol{u}_e$ and $\boldsymbol{u}_M$ are the electron and the neutral molecule mean velocities. The collision frequency is ν_e. Since the background gas is assumed to be static and uniform, $\boldsymbol{u}_M = 0$. Therefore, the momentum continuity equation for the electron fluid, (2.12), may be recast as:

$$-\frac{1}{\nu_e m_e}\boldsymbol{\nabla}_r p_e - \frac{e}{\nu_e m_e} n_e \boldsymbol{E} = n_e \boldsymbol{u}_e \tag{2.21}$$

where the convective derivative was dropped since the collisions are singular events in time and the driving frequency of the applied potential is negligible compared to ν_e. Equation (2.21) defines the electron particle flux. The electron mobility is defined as

$$\mu_e \equiv \frac{e}{\nu_e m_e}. \tag{2.22}$$

The electron diffusion coefficient, D_e, is defined as the particle flux caused by a unit density gradient. If the temperature is constant one may write

$$\boldsymbol{J}_D = -\frac{1}{\nu_e m_e}\boldsymbol{\nabla}_r p_e = -\frac{kT_e}{\nu_e m_e}\boldsymbol{\nabla}_r n_e \equiv -D_e \boldsymbol{\nabla}_r n_e. \tag{2.23}$$

The electron particle flux, equation (2.21), is now

$$\boldsymbol{J}_e = -D_e \boldsymbol{\nabla}_r n_e - \mu_e n_e \boldsymbol{E} = n_e \boldsymbol{u}_e. \tag{2.24}$$

From equations (2.22) and (2.23) we have

$$\frac{D_e}{\mu_e} = \frac{kT_e}{e} \tag{2.25}$$

which is known as the Einstein relation. A similar expression is obtained for the ion particle flux density:

$$\boldsymbol{J}_{ion} = -D_{ion}\boldsymbol{\nabla}_r n_{ion} + \mu_{ion} n_{ion} \boldsymbol{E} = n_{ion} u_{ion}. \tag{2.26}$$

The electron heat flux density due to peculiar motion, $\boldsymbol{q}_{ce}$, is taken to have the following phenomenological expression:

$$\boldsymbol{q}_{ce} = -K\boldsymbol{\nabla}_{\boldsymbol{r}}T_e. \tag{2.27}$$

An expression for the thermal heat conductivity, K, can be obtained from the so-called τ-approximation. In this approximation the distribution function has a small deviation from the Maxwellian distribution, and the integral defining $\boldsymbol{q}$, equation (2.16), can be evaluated to yield:

$$K = \frac{5nk^2T}{2m_e}\tau, \tag{2.28}$$

where τ is the characteristic collision time ($1/\nu_e$ above), which corresponds to the relaxation time for thermal equilibrium. Details of the derivation of equation (2.28) can be found in the textbook by Sitenko and Malnev [84]. By comparison with equation (2.23), we define the electron thermal conductivity as:

$$\tilde{K}_e = \frac{5k}{2}D_e n_e \frac{T_e}{T_e^{av}} \tag{2.29}$$

where the constant temperature assumption in equation (2.23) is not maintained, and T_e^{av} is the average electron temperature (scaling factor).

As discussed in section 1.1.1, the ions are assumed to be in thermal equilibrium with the background gas. Therefore the kinetic energy continuity equation for the ionic fluid, (2.19), is not considered.

We now need expressions for the collision terms for the particle number continuity equation, (2.7), and for the electron kinetic energy continuity equation.

The collision term for the particle continuity equation takes into consideration the creation and loss of particles of the given species by inelastic collision. We consider the ionization process given by electron impact on neutral molecules (background gas). In this process one electron and one positive ion are created, therefore the same collision integral will appear in both the electron and positive ion continuity equations. Since the ionization level of the gas is generally low, on the order of 10^{-6}, other processes such as double ionization and recombination processes do not play an important role. The collision integral for a binary collision between an electron and a neutral molecule at rest is given by:

$$\left(\frac{\mathrm{d}f}{\mathrm{d}t}\right)_c = \int \sigma_i v_e \left(f_e(\boldsymbol{r}, \boldsymbol{v}_e, t) f_M(\boldsymbol{r}, \boldsymbol{v}_M, t)\right) d\boldsymbol{v}_M \tag{2.30}$$

where σ_i is the ionization cross section, and subscripts e and M indicate quantities referring to the electron and neutral molecule respectively. This equation is known as the Boltzmann collision integral. Since the neutral molecules are at rest, by assuming their velocity distribution to be Maxwellian, it may be reduced to:

$$\left(\frac{\mathrm{d}f}{\mathrm{d}t}\right)_c = N\sigma_i v_e f_e(\boldsymbol{r}, \boldsymbol{v}_e, t). \tag{2.31}$$

The electron impact ionization rate is given by integrating over the electron velocity:

$$\tilde{S}_z = N \int \sigma_i v_e f_e(\boldsymbol{r}, \boldsymbol{v}_e, t) \tag{2.32}$$

We may assume the electron distribution function to also be Maxwellian, use the experimentally determined cross section, and integrate numerically to obtain the rate constant $\tilde{S}_z$:

$$\tilde{S}_z = N \left(\frac{m_e}{2\pi k T_e}\right)^{3/2} \int_0^\infty \sigma_i v_e^2 \exp\left(-\frac{m_e v_e^2}{2kT_e}\right) 4\pi v_e^2 \, dv_e. \tag{2.33}$$

The results presented by Graves and Jensen [64] were obtained by assuming an analytical approximation to $\tilde{S}_z$ in the form of

$$\tilde{S}_z = N n_e k_z e^{-\bar{E}/T_e} \tag{2.34}$$

where $\bar{E}$ is the ionization energy and the factor k_z is a constant. A better estimation of the ionization rate can be obtained by taking the electron distribution function obtained from the numerical resolution of the Boltzmann equation. We use an analytical approximation to the ionization rate in the form of

$$\tilde{S}_z = \begin{cases} N n_e k_{z0} & \text{if } T_e < T_L \\ N n_e k_z \exp\left(\frac{\bar{E}_1}{T_e} + \frac{\bar{E}_2}{T_e^2} + \frac{\bar{E}_3}{T_e^3} + \frac{\bar{E}_4}{T_e^4}\right) & \text{if } T_e > T_L \end{cases} \tag{2.35}$$

D_e	Electron diffusion rate	$\mathrm{cm^2\,s^{-1}}$
μ_e	Electron mobility	$\mathrm{cm^2\,V^{-1}\,s^{-1}}$
D_{ion}	Ion diffusion rate	$\mathrm{cm^2\,s^{-1}}$
μ_{ion}	Ion mobility	$\mathrm{cm^2\,V^{-1}\,s^{-1}}$
k_{z0}	Minimum electron impact inelastic collision frequency	$\mathrm{cm^3\,s^{-1}}$
T_L	Cut-off electron energy	eV
k_z	Electron impact inelastic collision pre-exponential factor	$\mathrm{cm^3\,s^{-1}}$
$\tilde{E}_1$	Activation energy for inelastic process by electron impact	eV
$\tilde{E}_2$	Activation energy for inelastic process by electron impact	$\mathrm{eV^2}$
$\tilde{E}_3$	Activation energy for inelastic process by electron impact	$\mathrm{eV^3}$
$\tilde{E}_4$	Activation energy for inelastic process by electron impact	$\mathrm{eV^4}$
$\tilde{H}_z$	Energy loss per inelastic process by the electron fluid	eV

Table 2.1: Plasma parameters for discharge space region with their units.

where $k_{z0}, k_z, T_L, \tilde{E}_1, \tilde{E}_2, \tilde{E}_3$, and $\tilde{E}_4$ are constants. See Table 2.1 for their units. Park and Economou [65] used a similar analytical approximation for RF discharge in low pressure Cl_2.

The collision integral for the electron kinetic energy continuity equation takes into account energy losses by the electron fluid due to ionization and excitation of the background gas. These losses are modeled as:

$$\left(\frac{\mathrm{d}}{\mathrm{d}t}\left(\frac{1}{2}n_e m_e \langle v^2\rangle\right)\right)_c = -\tilde{H}_z\tilde{S}_z - \sum_{Z=1}^{n_Z} \tilde{H}_Z\tilde{S}_Z \tag{2.36}$$

where $\tilde{H}_z\tilde{S}_z$ is the contribution for ionization process and $\sum_{Z=1}^{n_Z}\tilde{H}_Z\tilde{S}_Z$ represents contributions from other inelastic processes. The energy loss per ionization is given by $-\tilde{H}_z$.

2.2.2 Plasma model

The hydrodynamic equations can be closed to form a two-fluid model of gas discharge using the plasma kinetic parameters and transfer functions defined in the previous section.

The particle number continuity equations for the electrons and positive ions are:

$$\frac{\partial n_e}{\partial t} + \boldsymbol{\nabla}_{\boldsymbol{r}}\cdot\boldsymbol{J}_e = \tilde{S}_z, \text{ and} \tag{2.37}$$

$$\frac{\partial n_{ion}}{\partial t} + \boldsymbol{\nabla}_{\boldsymbol{r}}\cdot\boldsymbol{J}_{ion} = \tilde{S}_z \tag{2.38}$$

where n_e and n_{ion} are the electron and positive ion particle number densities. The electron flux density, $\boldsymbol{J}_e$, and the ion flux density, $\boldsymbol{J}_{ion}$, are each defined by a combination of a diffusion and a drift term:

$$\boldsymbol{J}_e = -D_e \boldsymbol{\nabla}_{\boldsymbol{r}} n_e + \mu_e n_e \boldsymbol{\nabla}_{\boldsymbol{r}} \Phi, \tag{2.39}$$

$$\boldsymbol{J}_{ion} = -D_{ion} \boldsymbol{\nabla}_{\boldsymbol{r}} n_{ion} - \mu_{ion} n_{ion} \boldsymbol{\nabla}_{\boldsymbol{r}} \Phi. \tag{2.40}$$

The charge density is obtained by multiplying the particle number density by the respective charge; $-e$ for electron and $+e$ for ion. The electric potential distribution between the electrodes, Φ, taking into consideration the space charge due to the particle distribution, is given by the Poisson equation:

$$\nabla_{\boldsymbol{r}}^2 \Phi + \frac{e}{\epsilon}\left(n_{ion} - n_e\right) = 0 \tag{2.41}$$

where ϵ is the electric permittivity. In the region without dielectric material the permittivity is taken as ϵ_0, the permittivity of free space. In the region occupied by the dielectric barrier the permittivity is $\epsilon = \epsilon_0 \epsilon_r$, see section 2.2.4.

As mentioned in the previous section, the ions are assumed to be in thermal equilibrium with the background gas. The electrons are not in equilibrium with the ions, but are assumed to be in equilibrium among themselves. The kinetic energy continuity equation for the electrons, (2.19), can be simplified when the transport energy of the particles is much less than their thermal energy due to the peculiar motion. This can be argued physically for an electron gas from the fact that the elastic collision cross section is much greater than the inelastic collision cross section, which keeps their velocities randomized rather than field directed. This assumption will be tested in section 4.2.1 once a solution to the model's equations is obtained. Using the collision integral given by equation (2.36), the electron temperature continuity equation is:

$$\frac{3k}{2}\frac{\partial\left(n_e T_e\right)}{\partial t} + \boldsymbol{\nabla}_{\boldsymbol{r}}\cdot\boldsymbol{q}_e + e\boldsymbol{J}_e \cdot \boldsymbol{E} = -\tilde{H}_z \tilde{S}_z - \sum_{Z=1}^{n_Z} \tilde{H}_Z \tilde{S}_Z \tag{2.42}$$

where q_e is the electron heat flux that includes the enthalpy flux and the thermal conductivity due to the peculiar motion of the electrons:

$$q_e = \frac{5k}{2} T_e \boldsymbol{J}_e - \tilde{K}_e \boldsymbol{\nabla}_r T_e. \tag{2.43}$$

The electron thermal conductivity is:

$$\tilde{K}_e = \frac{5}{2} D_e n_e \frac{T_e}{T_e^{av}}, \tag{2.44}$$

where T_e^{av} is an estimate of the average electron temperature. We use the analytical approximation given by equation (2.35) for the inelastic collision rates, $\bar{S}_z$ and $\bar{S}_Z$.

All the kinematic parameters of the plasma are grouped in Table 2.1.

2.2.3 Plasma-electrode boundary conditions

To uniquely specify the solutions of equations (2.37)–(2.42) each dependent variable must have two boundary conditions in geometric space and one in time. The boundary conditions are of the Dirichlet type or, more generally, expressed as equations specifying the behavior of dependent variables at the boundary.

At the plasma-electrode boundary the conditions for the electric potential are, in geometric space, of the Dirichlet type:

$$\Phi = \Phi^{A/C}(t). \tag{2.45}$$

The applied voltages at the anode and cathode are $\Phi^A(t)$ and $\Phi^C(t)$ respectively. The frequency of the applied potential is too high for the ions to have time to respond within each period. As a consequence, their density is practically frozen, with a small diffusion at the electrodes. Therefore, the ion flux density at the plasma-electrode boundary is

$$\boldsymbol{J}_{ion} = -\mu_{ion} n_{ion} \boldsymbol{\nabla}_r \Phi. \tag{2.46}$$

Secondary electron emission by ion impact on the cathode is considered. The boundary condition for the electron density at the cathode is

$$\boldsymbol{J}_e = -\gamma \boldsymbol{J}_{ion}. \tag{2.47}$$

The factor γ represents the fraction of the ions with sufficient kinetic energy to expel an electron from the cathode.

Many authors, following Chung [55], considered the anode surface to be a perfect conductor where the electrons and the ions recombine infinitely fast. In this case, one would set n_e=0 at the anode. Graves [66] considers the electrons to recombine at a finite rate, and writes the boundary condition for the electron density at the anode as:

$$\boldsymbol{J}_e \cdot \hat{\boldsymbol{S}} = k_r n_e \tag{2.48}$$

where $\hat{\boldsymbol{S}}$ is a unit normal vector directed outward from the plasma (pointing into the anode surface). By comparing this equation with the definition of $\boldsymbol{J}_e$, equation (2.24), the electron recombination rate at the anode, k_r, corresponds to the velocity at which the electrons hit the anode. Therefore specifying the rate at which the electrons recombine at the anode translates into specifying the velocity of the electrons at the anode. Graves [66] and many authors following him, such as Park and Economou [65], have taken the recombination rate k_r to be constant. This implicitly assumes a given electron temperature at the anode surface since at a non-emitting surface the velocity distribution function cannot be isotropic. Using equation (2.17) at the anode, taking $v_e|_{\text{anode}} = k_r$ and assuming the transport energy of the particles to be negligible compared to their thermal energy, we get:

$$k_r = \sqrt{\frac{3k}{m_e}T_e}. \tag{2.49}$$

By substituting this result in equation (2.48), the boundary condition for the electron flux density at the anode becomes:

$$\boldsymbol{J}_e \cdot \hat{\boldsymbol{S}} = n_e\sqrt{\frac{3k}{m_e}T_e}. \tag{2.50}$$

Lymberopoulos and Economou [85] used a similar boundary condition. However, their boundary condition for the electron temperature was incorrect, as will be shown below.

The boundary condition for the electron temperature is not easy to specify and remains an open question in the literature. Graves [66] derived an energy equation boundary condition based on an energy balance equation at the surface. Such a condition can be obtained only in the limit where the electron temperature is in equilibrium with the field. However, this is not the case, particularly in the plasma sheaths, where the electrons are far from equilibrium. In a recent analysis of polysilicon etching with chlorine by Lymberopoulos and Economou [85], a similar boundary condition was used. This energy balance boundary condition equates the electron heat flux at the surface to the net balance between the absorption and emission of energy:

$$\boldsymbol{q}_e \cdot \hat{\boldsymbol{S}} = k_r n_e \left(\frac{3}{2}kT_e\right) - \gamma \boldsymbol{J}_{ion} \cdot \hat{\boldsymbol{S}} \left(\frac{3}{2}kT_e^C\right) \tag{2.51}$$

where the energy lost by electrons being absorbed with temperature T_e is given by the first term on the right-hand-side, while the second term is the energy gained by the electron fluid due to secondary emission of electrons at cathode temperature T_e^C. This energy balance equation can be expressed as an equation for T_e. Consider a non-emitting electrode, using equation (2.43) for $\boldsymbol{q}_e$ we get:

$$\frac{5k}{2}T_e \boldsymbol{J}_e \cdot \hat{\boldsymbol{S}} - \bar{K}_e \hat{\boldsymbol{S}} \cdot \boldsymbol{\nabla}_r T_e = \frac{3kk_r}{2} n_e T_e \tag{2.52}$$

then using equation (2.48) for $\boldsymbol{J}_e \cdot \hat{\boldsymbol{S}}$ yields after rearranging:

$$\hat{\boldsymbol{S}} \cdot \boldsymbol{\nabla}_r T_e = \frac{2k_r}{5D_e} T_e^{av}. \tag{2.53}$$

This implies that the temperature gradient at a non-emitting electrode is constant, independent of the electric force acting on the electrons. This is physically incorrect. At the electrode the gradient of the electron temperature is expected to depend on the electric field; if the electrons are going against the field there should be a cooling of the electrons, while, if they drift toward the electrode there should be a heating of the electrons. This was pointed out by Wilcoxson and Manousiouthakis [67] without, however, explaining why the energy balance boundary condition is incorrect. As mentioned before, this boundary condition can only be derived if the electrons are in equilibrium with the electric field. Wilcoxson and Manousiouthakis were not able to formulate the boundary condition for the electron temperature from first principles.

Therefore, they fixed the electron temperature to a given value at both electrodes. However, their numerical results still exhibited non-physical behavior near the non-emitting electrode, the anode, regardless of the values used for the electron temperature at the electrodes.

We can obtain a correct boundary condition for the electron temperature based on physical considerations. Consider the region near the non-emitting, absorbent surface. In this region the electron density is small compared to that found over the bulk of the plasma. In the limit of small n_e, the electron thermal conductivity becomes negligible and the energy transport mechanism is due to the enthalpy flux. Moreover, the electron-neutral molecule collisions become negligible compared to the Joule heating term. Therefore, the electron temperature equation reduces to:

$$\frac{5k}{2}\boldsymbol{\nabla}_{\boldsymbol{r}}\cdot(T_e\boldsymbol{J}_e) = -e\boldsymbol{J}_e\cdot\boldsymbol{E}. \tag{2.54}$$

Since the electron-neutral molecule collision frequency is small, the electron density continuity equation reduces to $\boldsymbol{\nabla}_{\boldsymbol{r}}\cdot\boldsymbol{J}_e = 0$, and therefore:

$$\frac{5k}{2}\boldsymbol{J}_e\cdot\boldsymbol{\nabla}_{\boldsymbol{r}}T_e = -e\boldsymbol{J}_e\cdot\boldsymbol{E}. \tag{2.55}$$

Assuming that the electron flux is not zero, and since the surface is absorbing and non-emitting, in the limit of being sufficiently close to the surface, the electron flux may be assumed to be in the direction of $\hat{\boldsymbol{S}}$. However, the electric field is normal to the electrode in this region:

$$\hat{\boldsymbol{S}}\cdot\boldsymbol{\nabla}_{\boldsymbol{r}}T_e = -\frac{2e}{5k}\hat{\boldsymbol{S}}\cdot\boldsymbol{E}. \tag{2.56}$$

This condition is consistent with the correct physical behavior. Consider the case in which the electric field is directed toward the absorbing surface, which yields $\hat{\boldsymbol{S}}\cdot\boldsymbol{E} = E$, and therefore a negative gradient for the electron temperature, i.e., a cooling of the electrons. This is physically correct since the force on the electrons is $-e\boldsymbol{E}$, i.e., to exert a force to push them away from the surface.

In summary, it has been shown that in the limit when the electrons are in thermal equilibrium with the electric field, the gradient of the electron temperature is independent of the electric field, by equation (2.53), which is physically incorrect. However, a continuum analysis in the region close to the absorbing surface gives the physically correct relationship between the gradient of the electron temperature and the electric field, equation (2.56). Chung [55] showed that a singularity exists for the electron temperature continuity equation at the surface of a non-emitting conductor. Mathematically, this singularity was found to be removable by using a boundary condition similar to equation (2.56). It was argued by Chung that near the surface, in a region of few mean free paths, the electron distribution function is completely out of equilibrium. This layer is responsible for the surface electron temperature jump and affects the entire electron temperature profile across the plasma. His analysis also considered the case when the surface emits electrons. In this case he showed that fixing the electron temperature to a given value was a correct boundary condition.

The boundary conditions used in this thesis for the electron flux density and for the electron temperature at the anode are equations (2.50) and (2.56) respectively. At the cathode the electron temperature is fixed to a given value:

$$T_e = T_e^C. \tag{2.57}$$

The results presented in section 4.2.2 will show that the boundary condition given by equation (2.56) applied at the anode gives physically correct solutions, and that fixing the electron temperature at the anode gives physically incorrect solutions.

The applied potential at the electrode is periodic in time and acts as a driving force for the system. When the plasma reaches steady state, all the dependent variables must be periodic in time. Periodicity in the dependent variables is the governing constraint in time.

2.2.4 Plasma-dielectric barrier boundary condition

We now consider the case where the electron emitting electrode is covered with a dielectric material of a non-negligible thickness, compared to the inter-electrode spacing. The gas discharge process in this configuration is called silent discharge. The dielectric slab is often referred to as the dielectric barrier. The geometry of the electrode model is shown in Figure 1.1.

There is no free charge inside the dielectric, i.e., $n_e = n_{ion} = 0$. Consequently, the equations of the model, (2.37)–(2.42), simply reduce to the Laplace equation for the electric potential in this region

$$\nabla_r^2 \Phi_D = 0. \tag{2.58}$$

In this case, the interest lies at the plasma-dielectric interface, in particular, how the discontinuity in the gradient of the electric potential and the charge accumulation on the dielectric barrier affect the characteristics and response behavior of the plasma to the driving force. The normal component of the electric displacement vector at the plasma-dielectric interface is discontinuous by the amount of free charge deposited on the surface of the dielectric. See the textbook of Lorrain and Corson [86], chapter 4. In terms of the unit vector normal to the surface enclosing the plasma, $\hat{\boldsymbol{S}}$, defined by Figure 2.1 a condition on the normal components of the electric field on either side of the interface is obtained according to Gauss's law:

$$\epsilon_r \boldsymbol{E_D} \cdot \hat{\boldsymbol{S}} - \boldsymbol{E} \cdot \hat{\boldsymbol{S}} = \frac{e}{\epsilon_0}(\sigma_{ion} - \sigma_e), \tag{2.59}$$

where we used the assumption that the dielectric barrier is a dielectric of class A with ϵ_r the relative permittivity constant. In terms of the electric potential, the condition becomes

$$\hat{\boldsymbol{S}} \cdot \boldsymbol{\nabla_r} \Phi - \epsilon_r \hat{\boldsymbol{S}} \cdot \boldsymbol{\nabla_r} \Phi_D = \frac{e}{\epsilon_0}(\sigma_{ion} - \sigma_e). \tag{2.60}$$

We need a mechanism for charge accumulation on the surface of the dielectric. This will give boundary conditions at the plasma-dielectric interface for the electrons and ions. If the net electron flux is directed toward the dielectric barrier, i.e., $\boldsymbol{J}_e \cdot \hat{\boldsymbol{S}} > 0$, then the electron attachment to the dielectric surface will occur at a given rate k_e^σ. The inverse mechanism, i.e., secondary emission of electrons from the dielectric barrier into the plasma due to ion impact on the barrier is considered if $\boldsymbol{J}_{ion} \cdot \hat{\boldsymbol{S}} > 0$. These boundary conditions are similar to

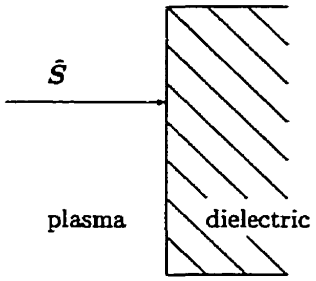

Figure 2.1: Definition of the unit vector normal to the surface enclosing the plasma.

those used at the electrodes; the dielectric barrier can be simultaneously both an absorbing and an emitting surface. The boundary condition for the electron density at the plasma-dielectric barrier interface is then

$$\boldsymbol{J}_e \cdot \hat{\boldsymbol{S}} = k_e^\sigma n_e - \gamma^\sigma \boldsymbol{J}_{ion} \hat{\boldsymbol{S}}, \tag{2.61}$$

where γ^σ is the electron secondary emission coefficient. The ion boundary condition is the same as at the electrodes, see equation (2.46). The arguments for using a drift only ion flux at the dielectric barrier are the same as that used for the electrodes. Furthermore, this condition gives good numerical stability.

Governing equations for the surface densities, σ_e and σ_{ion}, are required to complement the boundary equations. Continuity-type equations are formulated for σ_e and σ_{ion} based on surface charge balance:

$$\frac{\partial \sigma_e}{\partial t} = \boldsymbol{J}_e \cdot \hat{\boldsymbol{S}} - k_r^\sigma \sigma_e \sigma_{ion}, \tag{2.62}$$

and

$$\frac{\partial \sigma_{ion}}{\partial t} = \boldsymbol{J}_{ion} \cdot \hat{\boldsymbol{S}} - k_r^\sigma \sigma_e \sigma_{ion}. \tag{2.63}$$

Using the boundary condition for n_e given by equation (2.61) in equation (2.62), followed by using $\boldsymbol{E} = -\boldsymbol{\nabla}_r \Phi$ gives

$$\frac{\partial \sigma_e}{\partial t} = k_e^\sigma n_e + \gamma^\sigma \mu_{ion} n_{ion} \hat{\boldsymbol{S}} \cdot \boldsymbol{\nabla}_r \Phi - k_r^\sigma \sigma_e \sigma_{ion}. \tag{2.64}$$

The first term on the right-hand-side is a source term for the surface charge that exists if $\boldsymbol{J}_e \cdot \hat{\boldsymbol{S}} > 0$; the second term is a loss term which exists if $\boldsymbol{J}_{ion} \cdot \hat{\boldsymbol{S}} > 0$; and, the last term is a loss term which represents electron-ion recombination at the dielectric surface. Similarly using equation (2.46) in the governing equation for σ_{ion}, equation (2.63), gives:

$$\frac{\partial \sigma_{ion}}{\partial t} = -\mu_{ion} n_{ion} \hat{\boldsymbol{S}} \cdot \nabla_r \Phi - k_r^\sigma \sigma_e \sigma_{ion}. \tag{2.65}$$

The first term on the right-hand-side is the source term for the surface charge that exists if $\boldsymbol{J}_{ion} \cdot \hat{\boldsymbol{S}} > 0$ and the second term is the loss term due to electron-ion recombination.

The periodicity in time of the dependent variable may be broken due to surface charge accumulation if recombination during one cycle does not equal the amount of charges accumulated during that cycle.

All kinematic parameters of the plasma at the boundaries are given in Table 2.2.

k_e^σ	Electron attachment rate at dielectric surface	$\mathrm{cm\,s^{-1}}$
k_r^σ	Electron-ion recombination rate on dielectric surface	$\mathrm{cm^2\,s^{-1}}$
γ	Secondary electron emission coefficient at cathode	
γ^σ	Secondary electron emission coefficient at dielectric barrier	
ϵ_r	Dielectric barrier relative permittivity constant	

Table 2.2: Plasma kinematic parameters at electrodes and dielectric barrier boundaries with their units.

2.3 Non-dimensional form of the model's equations

The equations of the model must be put in a non-dimensional form to be more tractable for obtaining numerical solutions. The scaling factors found in Table 2.3 are used to define the dimensionless variables of Table 2.4. The scaling factors are chosen so as to render the dimensionless variables in the range of zero to unity. The equations of the model, equations (2.37)–(2.42),

N	Background gas density	cm^{-3}
N_o	Average charge particle density	cm^{-3}
d	Inter-electrodes gap length	cm
V_o	Electric potential scaling factor	V
ν	Frequency of applied voltage	s^{-1}
T_e^{av}	Electron temperature scaling factor	eV

Table 2.3: Plasma scaling factors with their units.

may be recast using the dimensionless variables as:

$$\Gamma \frac{\partial n^-}{\partial \tau} + \nabla \cdot \boldsymbol{J}^- = S_z \tag{2.66}$$

$$\Gamma \beta \frac{\partial n^+}{\partial \tau} + \nabla \cdot \boldsymbol{J}^+ = \beta S_z \tag{2.67}$$

$$\frac{3}{5} \Gamma \frac{\partial \left(n^- T^-\right)}{\partial \tau} + \nabla \cdot \boldsymbol{q}^- - J_o \boldsymbol{J}^- \cdot \nabla \phi = -H_z S_z - \sum_{Z=1}^{n_Z} H_Z S_Z \tag{2.68}$$

$$\nabla^2 \phi + Q \left(n^+ - n^-\right) = 0 \tag{2.69}$$

The corresponding dimensionless constitutive relations are

$$\boldsymbol{J}^- = -\nabla n^- + M^- n^- \nabla \phi, \tag{2.70}$$

$$\boldsymbol{J}^+ = -\nabla n^+ - M^+ n^+ \nabla \phi, \tag{2.71}$$

$$\boldsymbol{q}^- = T^- \boldsymbol{J}^- - K \nabla T^-, \tag{2.72}$$

$$K = n^- T^-, \tag{2.73}$$

$$S_z = A_z n^- F_z(T^-), \text{ and } S_Z = A_Z n^- F_Z(T^-). \tag{2.74}$$

The dimensionless ratios M^-, M^+, A_z, and A_Z are all constants defined in Table 2.5. Huang and Kushner [80] considered the electron distribution function to be non-Maxwellian and computed the electron diffusion rate and mobility as well as the energy transfer function to be functions of electron temperature using a Monte Carlo simulation technique. The calculated electron kinetic coefficients were used in a fluid model to obtain the distribution of the self-consistent electric field, the electron distribution, and the electron temperature

$\boldsymbol{x}$	Dimensionless spatial coordinate	$\boldsymbol{r}/d$
τ	Dimensionless time	νt
n^+	Ion density	n_{ion}/N_o
T^-	Electron temperature	T_e/T_e^{av}
ϕ	Electric potential in discharge space	Φ/V_o
ϕ_D	Electric potential in dielectric barrier	Φ_D/V_o
σ^-	Electron surface density	$\sigma_e/(N_o\, d)$
σ^+	Ion surface density	$\sigma_{ion}/(N_o\, d)$

Table 2.4: Dimensionless variables characterizing the plasma with their definitions.

over geometric space. In this present work, only the energy transfer function is considered to be significantly affected by the non-Maxwellian nature of the electron distribution function. The dimensionless energy transfer function for ionization and other inelastic collisions by electron impact on neutral molecules, F_z and F_Z respectively, are both approximated using a similar analytical function:

$$F_z = \begin{cases} F_{z0} & \text{if } T^- < T_L^- \\ \exp\left(\frac{E_1}{T^-} + \frac{E_2}{(T^-)^2} + \frac{E_3}{(T^-)^3} + \frac{E_4}{(T^-)^4}\right) & \text{if } T^- > T_L^- \end{cases} \tag{2.75}$$

The dimensionless ratios used in the above equations are defined in Table 2.5. Using the numerical method developed in the following chapter, it would be straightforward to represent all the kinematic coefficients as functions of temperature. Further, the kinematic coefficients for the ions could be represented as functions of the electric field. The relative importance of each term is now indicated by the dimensionless ratio. This will be discussed in section 4.2.1. The equation for the electron temperature, equation (2.68), is manipulated to remove the divergence of the electron density flux vector by using the equation of motion for the electron density. The divergence of the electron heat flux is

$$\begin{aligned} \nabla\cdot\boldsymbol{q}^- &= \nabla\cdot\left(T^-\boldsymbol{J}^- - K\,\nabla T^-\right) && (2.76) \\ &= T^-\nabla\cdot\boldsymbol{J}^- + \boldsymbol{J}^-\cdot\nabla T^- - \nabla\cdot\left(K\,\nabla T^-\right). && (2.77) \end{aligned}$$

Γ	Electron characteristic diffusion time	$\nu d^2/D_e$
M^-	Electron mobility to diffusivity ratio	$\mu_e V_o/D_e$
M^+	Ion mobility to diffusivity ratio	$\mu_{ion} V_o/D_{ion}$
β	Electron to ion diffusivity ratio	D_e/D_{ion}
Q	Characteristic electric field strength	$eN_o d^2/(\epsilon_0 V_o)$
J_o	Characteristic potential to electron thermal energy ratio	$2eV_o/(5T_e^{av})$
A_z	Ionization coefficient	$Nk_z d^2/D_e$
A_Z	Inelastic process coefficient	$2Nk_Z d^2/(5T_e^{av} D_e)$
E_1	Activation energy to T_e^{av} ratio	$\tilde{E}_1/T_e^{av}$
E_2	Activation energy to T_e^{av2} ratio	$\tilde{E}_2/T_e^{av2}$
E_3	Activation energy to T_e^{av3} ratio	$\tilde{E}_3/T_e^{av3}$
E_4	Activation energy to T_e^{av4} ratio	$\tilde{E}_4/T_e^{av4}$
H_z	Energy loss to T_e^{av} ratio per ionization	$2\tilde{H}_z/(5kT_e^{av})$
H_Z	Energy loss to T_e^{av} ratio per inelastic process	$2\tilde{H}_Z/(5kT_e^{av})$

Table 2.5: Dimensionless ratios used in plasma equations with their definitions.

If the $\nabla \cdot \boldsymbol{J}^-$ term is replaced using equation (2.66), then the divergence of the electron heat flux becomes:

$$\nabla \cdot \boldsymbol{q}^- = -\Gamma T^- \frac{\partial n^-}{\partial \tau} + T^- S_z + \boldsymbol{J}^- \cdot \nabla T^- - \nabla \cdot \left(K \, \nabla T^- \right). \tag{2.78}$$

Substituting equation (2.78) into the governing equation for the electron temperature, equation (2.68), gives

$$\frac{3\Gamma}{5} n^- \frac{\partial T^-}{\partial \tau} - \frac{2\Gamma}{5} T^- \frac{\partial n^-}{\partial \tau} + \boldsymbol{J}^- \cdot \left(\nabla T^- - J_o \nabla \phi \right) = \nabla \cdot \left(K \, \nabla T^- \right) - T^- S_z - \sum_{Z=1}^{n_Z} H_Z S_Z. \tag{2.79}$$

In this form the boundary condition at the anode for the electron temperature, following the discussion of section 2.2.3, becomes evident.

2.3.1 Boundary conditions

The boundary conditions at the electrodes for the electric potential, as given by equation (2.45), scale into the dimensionless form,

$$\phi = \phi^{A/C}(\tau) = \Phi^{A/C}(t)/V_o. \tag{2.80}$$

Similarly, the boundary condition for the ion density, equation (2.46), becomes

$$\boldsymbol{J}^+ \cdot \hat{\boldsymbol{S}} = -M^+ n^+ \hat{\boldsymbol{S}} \cdot \boldsymbol{\nabla}\phi. \tag{2.81}$$

The boundary conditions for the electron density at the electrodes, as given by equations (2.47) and (2.50), become:

$$\boldsymbol{J}^- \cdot \hat{\boldsymbol{S}} = -\gamma/\beta\, \boldsymbol{J}^+ \cdot \hat{\boldsymbol{S}} \tag{2.82}$$

at the cathode, and

$$\boldsymbol{J}^- \cdot \hat{\boldsymbol{S}} = k_R n^- \left(T^-\right)^{1/2} \tag{2.83}$$

at the anode. The electron temperature boundary condition at the cathode is

$$T^- = T^{-C}, \tag{2.84}$$

and at the anode, using equation (2.56), is

$$\boldsymbol{\nabla} T^- = J_o \boldsymbol{\nabla}\phi. \tag{2.85}$$

Please see Table 2.6 for the definitions of the dimensionless ratios for the boundary conditions.

k_R	Electron recombination rate to D_e ratio at anode	$\sqrt{3d^2T_e^{av}/(D_e^2m_e)}$
k_-^σ	Electron attachment rate to D_e ratio at dielectric surface	$k_e^\sigma d/D_e$
k_R^σ	Electron-ion recombination rate to D_e ratio on dielectric	$N_o k_r^\sigma d^3/D_e$
γ	Secondary electron emission coefficient at cathode	
γ^σ	Secondary electron emission at dielectric barrier	
ϵ_r	Dielectric barrier relative permittivity constant	
$T^{-D/C}$	Electron temperature at dielectric/cathode surface	$T_e^{D/C}/T_e^{av}$

Table 2.6: Dimensionless ratios used for the boundary conditions with their definitions.

At the plasma-dielectric interface, the boundary condition for the electric potential, equation (2.60), becomes

$$\hat{\boldsymbol{S}} \cdot \boldsymbol{\nabla}\phi - \epsilon_r \hat{\boldsymbol{S}} \cdot \boldsymbol{\nabla}\phi_D = Q(\sigma^+ - \sigma^-). \tag{2.86}$$

The electron density boundary condition, equation (2.61), becomes

$$\boldsymbol{J}^- \cdot \hat{\boldsymbol{S}} = k^\sigma_- \, n^- - \gamma^\sigma / \beta \, \boldsymbol{J}^+ \cdot \hat{\boldsymbol{S}}, \tag{2.87}$$

where the electron attachment to the dielectric surface term, $k^\sigma_- \, n^-$ is considered when the electron flux is directed towards the dielectric surface, i.e., $\boldsymbol{J}^- \cdot \hat{\boldsymbol{S}} > 0$. The electron secondary emission term, $-\gamma^\sigma / \beta \, \boldsymbol{J}^+ \cdot \hat{\boldsymbol{S}}$, is considered when the ion flux is directed towards the dielectric surface, i.e., $\boldsymbol{J}^+ \cdot \hat{\boldsymbol{S}} > 0$.

The ion density boundary condition at the dielectric surface is the same as that at the electrode, which is given by equation (2.81). The electron temperature at the dielectric surface is assumed to be known:

$$T^- = T^{-D} = T^D_e / T^{av}_e. \tag{2.88}$$

The equations of motion for the surface charge, equations (2.64) and (2.65), described in terms of the dimensionless variables are

$$\Gamma \frac{\partial \sigma^-}{\partial \tau} - k^\sigma_- \, n^- - \gamma^\sigma / \beta \, M^+ n^+ \hat{\boldsymbol{S}} \cdot \boldsymbol{\nabla} \phi + k^\sigma_R \, \sigma^- \, \sigma^+ = 0 \tag{2.89}$$

and

$$\Gamma \beta \frac{\partial \sigma^+}{\partial \tau} + M^+ n^+ \hat{\boldsymbol{S}} \cdot \boldsymbol{\nabla} \phi + \beta k^\sigma_R \, \sigma^- \, \sigma^+ = 0. \tag{2.90}$$

The electron attachment term, the second term of equation (2.89), is a source term for σ^- and is considered if $\boldsymbol{J}^- \cdot \hat{\boldsymbol{S}} > 0$. The third term of equation (2.89) is a sink term for σ^-, which is taken into account if $\boldsymbol{J}^+ \cdot \hat{\boldsymbol{S}} > 0$.

In the next chapter a finite element formulation is given to obtain an approximate solution to the two-fluid model equations, given by (2.66), (2.67), (2.69), and (2.79). The boundary conditions at the electrodes for the electric potential, the ion and electron densities, and electron temperature are given by the equations (2.80) to (2.85). At the plasma-dielectric interface, the boundary conditions for the electric potential, the electron density, and the electron temperature are given by equations (2.86), (2.87), and (2.88) respectively. The equations of motion for the surface charge are (2.89) and (2.90).

Chapter 3

Finite element formulation of the model

In this chapter a finite element formulation is given to obtain an approximate solution to the two-fluid model equations. The differential equations of the model are recast into integral equations using a Galerkin weighted residual method in section 3.1. To overcome the difficulties associated with the highly non-linear nature of the equations, new universal matrices are developed in section 3.2. This is an adaptation of a paper [87] presented at the *Third international conference on computation in electromagnetics* held at the University of Bath, UK, April 1996.

In section 3.3 the procedure for assembling the contributions to the residuals from each element into the global matrix is reduced to finding sums and products of universal matrices in a manner independent of element shape, dimensionality, and order. The solution in the time domain, which is also based on the Galerkin method, is presented in section 3.4.

3.1 Weighted residuals of the model's equations

A solution to the governing equations of the model, equations (2.37)–(2.41), together with the associated boundary conditions can be found numerically using a classical finite difference scheme based on a discretization of the differential operators $\frac{\partial}{\partial t}$ and ∇_r. Such a direct method, sometimes called a strong formulation, does not provide great flexibility in mesh discretization, and more importantly for the present work, tends to complicate the inclusion of complex boundary conditions. Another way to find a numerical solution to the governing equations is to use a weak formulation which consists of replacing the differential equations, as in the weighted residual method, by integral equations. The finite element method consists of subdividing the domain of interest into a set of subdomains, called finite elements, and applying a variational or a weighted residual method over each finite element. We used the Galerkin weighted residual method, which is widely used in engineering. The textbook of Lapidus and Pinder [88] presents a thorough treatment with comparisons to finite difference methods. Application of the finite element method in fluid dynamics is found in the textbook of Reddy and Gartling [89].

In this section we apply the Galerkin method to find an approximate solution over the spatial domain only, the solution over time domain will be discussed in section 3.4. The weighted residuals, for an element of volume V, of the Poisson equation for the electric potential, and the electron, ion and electron temperature continuity equations are:

$$R^{\phi}_{\alpha} = \frac{1}{V_o d} \int_V \left[-\nabla_r^2 \Phi - \frac{e}{\epsilon} \left(n_{ion} - n_e \right) \right] W_\alpha d\boldsymbol{r}, \tag{3.1}$$

$$R^{-}_{\alpha} = \frac{1}{N_o D_e d} \int_V \left[\frac{\partial n_e}{\partial t} + \boldsymbol{\nabla}_r \cdot \boldsymbol{J}_e - \tilde{S}_z \right] W_\alpha d\boldsymbol{r}, \tag{3.2}$$

$$R^{+}_{\alpha} = \frac{1}{N_o D_{ion} d} \int_V \left[\frac{\partial n_{ion}}{\partial t} + \boldsymbol{\nabla}_r \cdot \boldsymbol{J}_{ion} - \tilde{S}_z \right] W_\alpha d\boldsymbol{r}, \text{ and} \tag{3.3}$$

$$R^{T}_{\alpha} = \frac{2}{5kT_e^{av} N_o D_e d} \int_V \left[\frac{3k}{2} \frac{\partial \left(n_e T_e \right)}{\partial t} + \boldsymbol{\nabla}_r \cdot \boldsymbol{q}_e + e\boldsymbol{J}_e \cdot \boldsymbol{E} \right. \\ \left. + \tilde{H}_z \tilde{S}_z + \sum_{Z=1}^{nz} \tilde{H}_Z \tilde{S}_Z \right] W_\alpha d\boldsymbol{r} \tag{3.4}$$

respectively. For the case in which the element is inside the dielectric barrier, the particle densities vanish and the electron temperature is set to zero, therefore the respective residuals are dropped.

The weighted residuals of the equations of motion for the electron and ion surface charge densities, equations (2.64) and (2.65), are:

$$R_\alpha^{\sigma^-} = \frac{1}{N_o D_e d} \int_{S_D} \left[\frac{\partial \sigma_e}{\partial t} - k_e^\sigma n_e + \gamma^\sigma \boldsymbol{J}_{ion} \cdot \hat{\boldsymbol{S}} + k_r^\sigma \sigma_e \sigma_{ion} \right] W_\alpha dS, \text{ and} \tag{3.5}$$

$$R_\alpha^{\sigma^+} = \frac{1}{N_o D_{ion} d} \int_{S_D} \left[\frac{\partial \sigma_{ion}}{\partial t} - \boldsymbol{J}_{ion} \cdot \hat{\boldsymbol{S}} + k_r^\sigma \sigma_e \sigma_{ion} \right] W_\alpha dS \tag{3.6}$$

respectively, where S_D is the area of the element on the plasma-dielectric surface. The scaling factors multiplying the integrals in equations (3.1) to (3.6) scale the residuals to dimensionless form. Using the dimensionless coordinate system and dimensionless dependent variables, the residuals become:

$$R_\alpha^\phi = \int_\Omega \left[-\nabla^2 \phi - Q \left(n^+ - n^- \right) \right] W_\alpha d\Omega, \tag{3.7}$$

$$R_\alpha^- = \int_\Omega \left[\Gamma \frac{\partial n^-}{\partial \tau} + \boldsymbol{\nabla} \cdot \boldsymbol{J}^- - S_z \right] W_\alpha d\Omega, \text{ and} \tag{3.8}$$

$$R_\alpha^+ = \int_\Omega \left[\Gamma \beta \frac{\partial n^+}{\partial \tau} + \boldsymbol{\nabla} \cdot \boldsymbol{J}^+ - \beta S_z \right] W_\alpha d\Omega \tag{3.9}$$

and the integral form of equation (2.79) for the dimensionless electron temperature is:

$$\begin{aligned} R_\alpha^T = \int_\Omega & \left[\frac{3\Gamma}{5} n^- \frac{\partial T^-}{\partial \tau} - \frac{2\Gamma}{5} T^- \frac{\partial n^-}{\partial \tau} + \boldsymbol{J}^- \cdot \left(\boldsymbol{\nabla} T^- - J_o \boldsymbol{\nabla} \phi \right) - \right. \\ & \left. \boldsymbol{\nabla} \cdot \left(K \boldsymbol{\nabla} T^- \right) + T^- S_z + H_z S_z + \sum_{Z=1}^{n_Z} H_Z S_Z \right] W_\alpha d\Omega. \end{aligned} \tag{3.10}$$

The volume of the element in the dimensionless coordinate system is denoted by Ω. We remove the divergence terms in the above integrals by use of integration-by-parts followed by the divergence theorem. Performing integration-by-parts on the first term of the residual for the electric potential, equation (3.7), gives

$$\begin{aligned} -\int_\Omega \nabla^2 \phi \, W_\alpha d\Omega &= -\int_\Omega \left[\boldsymbol{\nabla} \cdot (\phi W_\alpha) - \boldsymbol{\nabla} \phi \cdot \boldsymbol{\nabla} W_\alpha \right] d\Omega \\ &= -\oint_{\partial\Omega} \hat{\boldsymbol{S}} \cdot \boldsymbol{\nabla} \phi \, W_\alpha dS + \int_\Omega \boldsymbol{\nabla} \phi \cdot \boldsymbol{\nabla} W_\alpha d\Omega \end{aligned} \tag{3.11}$$

where the divergence theorem was used on the first term on the right-hand-side. The surface which bounds the element of volume Ω is denoted by $\partial\Omega$.

The same procedure is followed for the divergence terms $\boldsymbol{\nabla}\cdot\boldsymbol{J}^-$, $\boldsymbol{\nabla}\cdot\boldsymbol{J}^+$, and $\boldsymbol{\nabla}\cdot(K\ \boldsymbol{\nabla}T^-)$ of equations (3.8), (3.9), and (3.10) respectively:

$$R_\alpha^- = \int_\Omega \left[\frac{\partial n^-}{\partial \tau} W_\alpha - \boldsymbol{J}^- \cdot \boldsymbol{\nabla} W_\alpha - S_z W_\alpha\right] d\Omega + \oint_{\partial\Omega} \boldsymbol{J}^- \cdot \hat{\boldsymbol{S}}\, W_\alpha dS \tag{3.12}$$

$$R_\alpha^+ = \int_\Omega \left[\Gamma\beta\frac{\partial n^+}{\partial \tau} W_\alpha - \boldsymbol{J}^+ \cdot \boldsymbol{\nabla} W_\alpha - \beta S_z W_\alpha\right] d\Omega + \oint_{\partial\Omega} \boldsymbol{J}^+ \cdot \hat{\boldsymbol{S}}\, W_\alpha dS \tag{3.13}$$

$$\begin{aligned} R_\alpha^T &= \int_\Omega \Bigg[\frac{3\Gamma}{5} n^- \frac{\partial T^-}{\partial \tau} W_\alpha - \frac{2\Gamma}{5} T^- \frac{\partial n^-}{\partial \tau} W_\alpha + \\ &\quad \boldsymbol{J}^- \cdot \left(\boldsymbol{\nabla} T^- - J_o \boldsymbol{\nabla}\phi\right) W_\alpha + K\, \boldsymbol{\nabla} T^- \cdot \boldsymbol{\nabla} W_\alpha + T^- S_z W_\alpha + \\ &\quad \left(H_z S_z + \sum_{Z=1}^{nz} H_Z S_Z\right) W_\alpha\Bigg] d\Omega - \oint_{\partial\Omega} K\, \hat{\boldsymbol{S}} \cdot \boldsymbol{\nabla} T^- W_\alpha dS. \end{aligned} \tag{3.14}$$

3.1.1 Surface terms of the residuals

Each adjacent element has the same surface contribution but with an opposite sign, except at the plasma-dielectric boundary, due to the discontinuity in the dependent variables, and at the electrodes since they represent the outer boundary of the problem space. Therefore, the net contributions from all surface integrals come from the surfaces at the plasma-dielectric interface and at the electrodes.

Define $R_\alpha^{\phi,D}$ and $R_\alpha^{\phi_D,D}$ as the residuals associated with the common edge or face of two adjacent elements, one just inside the plasma where the electric potential is ϕ and the other just inside the dielectric barrier where the electric potential is ϕ_D. The net contribution $R_\alpha^{\phi,D} + R_\alpha^{\phi_D,D}$ is:

$$R_\alpha^{\phi,D} + R_\alpha^{\phi_D,D} = -\int_{\Sigma_D} \left[\hat{\boldsymbol{S}} \cdot \boldsymbol{\nabla}\phi - \hat{\boldsymbol{S}} \cdot \boldsymbol{\nabla}\phi_D\right] W_\alpha d\Sigma \tag{3.15}$$

where Σ_D is the common face of the two elements. As defined previously, $\hat{\boldsymbol{S}}$ is a unit vector normal to the surface enclosing the plasma, c.f., Figure 2.1. Using the boundary condition for the electric potential at the plasma-dielectric boundary, equation (2.86), gives:

$$R_\alpha^{\phi,D} + R_\alpha^{\phi_D,D} = -\int_{\Sigma_D} \left[\frac{\epsilon_r - 1}{\epsilon_r}\hat{\boldsymbol{S}} \cdot \boldsymbol{\nabla}\phi + \frac{Q}{\epsilon_r}(\sigma^+ - \sigma^-)\right] W_\alpha d\Sigma. \tag{3.16}$$

Define $R_\alpha^{+,E}$ as an element's surface term for the ion density continuity equation residual along the edge Σ_E on an electrode:

$$R_\alpha^{+,E} = \int_{\Sigma_E} \boldsymbol{J}^+ \cdot \hat{\boldsymbol{S}}\, W_\alpha d\Sigma, \tag{3.17}$$

using the boundary condition given by equation (2.81) we get:

$$R_\alpha^{+,E} = -M^+ \int_{\Sigma_E} n^+ \hat{\boldsymbol{S}} \cdot \boldsymbol{\nabla}\phi\, W_\alpha d\Sigma. \tag{3.18}$$

A similar expression is obtained for the residual at the surface of the plasma-dielectric barrier. Define $R_\alpha^{-,E}$ as the counterpart for the electron density:

$$R_\alpha^{-,E} = \int_{\Sigma_E} \boldsymbol{J}^- \cdot \hat{\boldsymbol{S}}\, W_\alpha d\Sigma. \tag{3.19}$$

Using the boundary condition for $\boldsymbol{J}^-$ at the anode, equation (2.83), the residual becomes:

$$R_\alpha^{-,A} = k_R \int_{\Sigma_A} n^- \left(T^-\right)^{1/2} W_\alpha d\Sigma. \tag{3.20}$$

At the cathode, the boundary condition for $\boldsymbol{J}^-$, equation (2.82), relates the surface term of the residual for the electron density to the one for the ion density:

$$R_\alpha^{-,C} = -\gamma/\beta\, R_\alpha^{+,C}. \tag{3.21}$$

Using the plasma-dielectric interface boundary condition for electron flux density, equation (2.61), the surface contribution to the residual, equation (3.19), is:

$$R_\alpha^{-,D} = \int_{\Sigma_D} \left(k_-^\sigma n^- + \gamma^\sigma M^+/\beta n^+ \hat{\boldsymbol{S}} \cdot \boldsymbol{\nabla}\phi\right) W_\alpha d\Sigma. \tag{3.22}$$

Also define $R^{T,A}$ as the surface term of the residual for the electron temperature continuity equation for an element with the face Σ_A on the anode:

$$R_\alpha^{T,A} = -\int_{\Sigma_A} K\, \hat{\boldsymbol{S}} \cdot \boldsymbol{\nabla} T^- W_\alpha d\Sigma. \tag{3.23}$$

Using the boundary condition given by equation (2.85) we obtain:

$$R_\alpha^{T,A} = -J_o \int_{\Sigma_A} n^- T^- \hat{\boldsymbol{S}} \cdot \boldsymbol{\nabla}\phi W_\alpha d\Sigma. \tag{3.24}$$

The weighted residuals of the equations of motion for the electron and ion surface charge densities, equations (3.5) and (3.6), expressed in terms of dimensionless ratios and dependent variables are:

$$R_\alpha^{\sigma^-} = \int_{\Sigma_D} \left[\Gamma \frac{\partial \sigma^-}{\partial \tau} - k_-^\sigma n^- - \gamma^\sigma \beta^{-1} M^+ n^+ \hat{\boldsymbol{S}} \cdot \boldsymbol{\nabla} \phi + k_R^\sigma \sigma^- \sigma^+ \right] W_\alpha d\Sigma, \text{ and} \tag{3.25}$$

$$R_\alpha^{\sigma^+} = \int_{\Sigma_D} \left[\Gamma \beta \frac{\partial \sigma^+}{\partial \tau} + M^+ n^+ \hat{\boldsymbol{S}} \cdot \boldsymbol{\nabla} \phi + k_R^\sigma \beta \sigma^- \sigma^+ \right] W_\alpha d\Sigma. \tag{3.26}$$

3.2 Universal matrices for an n-dimensional element

Many engineering problems, including gas discharge physics, using the finite element method require the integration of various combinations of space-dependent functions, which include the unknown fields. These integrals may be recast into integrals over a generic element so that elemental integration matrices can be computed once and for all. Methods for deriving such *universal matrices* were presented by Silvester and Ferrari [90] and results were given for various well-known matrices, including the Dirichlet matrix and the metric matrix. This section presents new universal matrices suited to non-linear problems and to problems with material properties and source terms dependent on spatial position, fields and their derivatives. Assembling the contributions to the residual from each element into the global matrix can be reduced to finding sums and products of universal matrices. This formulation requires the use of simplex elements with a single family of polynomial interpolation functions for all quantities depending on space: source terms, material properties, and unknown fields. The integrals contributing to the residual are most conveniently computed in the local coordinates system (simplex coordinates) of the element. The Jacobian of the transformation from the global geometric coordinates to simplex coordinates depends on the geometry of the element but not on the coordinates. Therefore the Jacobian, and all other quantities dependent on the geometry, can be factored out of the integrals.

Universal matrices are defined as functions of spatial dimensionality and the polynomial order of the interpolation functions. The procedure of assembling an element's contribution to the global matrix is then identical for any element shape: line, triangle, rectangle, tetrahedron, etc. – even brick or hexahedron. In the following section, universal matrices are presented for computing integrals involving integrands composed of multiple products of space-dependent functions. These integrals are reduced to integrals of products of the polynomial interpolation functions. Differentiation operators in the integrand are replaced by differentiation matrices, another type of universal matrix, which are also factored out of the integrals. Geometric coefficients and node numbering for the line, triangle, and tetrahedral elements are given.

3.2.1 Universal matrices

In the finite element formulation, the spatial domain of interest is subdivided into small elements of a given geometry. Each element has N_b nodes at which the unknown fields, and all other quantities depending on spatial coordinates, are either computed or known in advance. For simplex elements, the nodal values are interpolated within the element using polynomial basis functions of order N_p, e.g.,

$$\phi(\boldsymbol{r}) = \sum_{\alpha=1}^{N_b} W_\alpha(\boldsymbol{r})\ \phi_\alpha. \tag{3.27}$$

The basis functions W_α form an orthonormal basis,

$$W_\alpha(\boldsymbol{r})|_{\text{at node } \beta} = \delta_{\alpha\beta} \tag{3.28}$$

therefore in equation (3.27) ϕ_α is the value of function $\phi(\boldsymbol{r})$ at node α.

A typical member of the set of basis functions, $W_\alpha(\boldsymbol{r})$, can be written in terms of a product of the basic polynomials $R_{\alpha_i}(N_p, \xi_i)$ introduced by Silvester and Ferrari [90]:

$$W_\alpha(\xi_0 \ldots \xi_n) = \prod_{i=0}^{n} R_{\alpha_i}(N_p, \xi_i), \tag{3.29}$$

where n is the spatial dimensionality. The number of basis functions is $N_b = (N_p + n)!/(n!\,N_p!)$. The advantage of using the basic polynomials $R_{\alpha_i}(N_p, \xi_i)$

resides in the uniformity in the expression of the basis functions $W_\alpha(\boldsymbol{r})$ with respect to spatial dimensionality.

Associated with each node of the element, denoted here by α, there is a set of $n+1$ indices α_i indicating the value of the simplex coordinate ξ_i at the node α;

$$\xi_i = \alpha_i / N_p \text{ at node } \alpha. \tag{3.30}$$

The indices α_i can be generated automatically for a simplex element in an n-dimensional space using the following pseudo-algorithm:

```
k = 0
loop $k_0 = N_p$ to 0, step -1
    loop $k_i = N_p$ - $k_{i-1}$ to 0, step -1 ($i = 1, n$-2)
        ⋮
        loop $k_{n-1} = N_p$ - $\sum_{l=0}^{n-2} k_l$ to 0, step -1
            k = k + 1
            $\alpha$ = k
            $\alpha_i = k_{i-1}$ ($i = 0, n$)
            $\alpha_{n+1} = N_p - \sum_{i=0}^{n} \alpha_i$
        end loop
            ⋮
    end loop
end loop
```

This pseudo-algorithm is easily implemented using a recursive function. Equation (3.29) has the following closure relations

$$\sum_{i=0}^{n} \alpha_i = N_p \text{ and } \sum_{i=0}^{n} \xi_i = 1. \tag{3.31}$$

The second closure relation is used in equation (3.29) to eliminate ξ_0:

$$W_\alpha (\xi_1 \ldots \xi_n) = R_{\alpha_i} \left(N_p, 1 - \sum_{i=1}^{n} \xi_i \right) \prod_{i=1}^{n} R_{\alpha_i} (N_p, \xi_i) \, . \tag{3.32}$$

The basic polynomials $R_{\alpha_i}(N_p, \xi_i)$ are

$$R_m(N,\xi) = \begin{cases} 1/m! \prod_{k=0}^{m-1}(N\xi - k) & m > 0 \\ 1 & m = 0 \end{cases} . \tag{3.33}$$

Computing the contribution to the residual for a particular element generally consists of computing integrals of products of functions depending on space. These functions are projected onto the basis functions, as in equation (3.27), thereby reducing the integrand to a product of basis functions. The resulting integrals are best computed in the local element coordinates. Figure 3.1 shows the transformation of coordinates for the case of a triangular element. For simplex elements the Jacobians $\mathcal{J}$ depend on the geometry of the element but not on the coordinates. The Jacobians are given by:

$$\mathcal{J} = \left| \frac{\partial(x_1 \ldots x_n)}{\partial(\xi_1 \ldots \xi_n)} \right| . \tag{3.34}$$

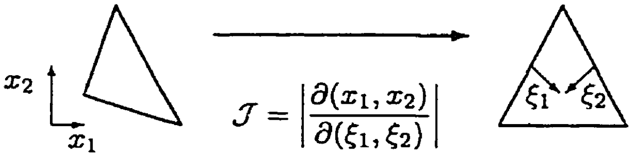

Figure 3.1: Transformation from global coordinate system to local coordinate system for triangular element.

A set of universal matrices can be defined for the integration of products of two to four basis functions. The *double-product matrix* is defined as

$$T_{\alpha\beta} = \mathcal{J}^{-1} \int_V W_\alpha W_\beta \, dV = \int_\Omega W_\alpha W_\beta \, d\Omega, \tag{3.35}$$

the *triple-product matrix* is defined as

$$\begin{aligned} Q_{\alpha\beta\gamma} &= \mathcal{J}^{-1} \int_V W_\alpha W_\beta W_\gamma \, dV \\ &= \int_\Omega W_\alpha W_\beta W_\gamma \, d\Omega, \end{aligned} \tag{3.36}$$

and the *quadruple-product matrix* is defined as

$$\begin{aligned} V_{\alpha\beta\gamma\sigma} &= \mathcal{J}^{-1} \int_V W_\alpha W_\beta W_\gamma W_\sigma \, dV \\ &= \int_\Omega W_\alpha W_\beta W_\gamma W_\sigma \, d\Omega. \end{aligned} \tag{3.37}$$

Here V is the element volume in geometric coordinates while Ω is the element volume in simplex coordinates. Note that all the above matrices are symmetric under the permutation of any index, therefore the number of independent elements to compute per matrix is $(N_b + N_w - 1)!/(N_w!\,(N_b - 1)!)$, where N_w is the number of basis functions in the integrand.

In the above integrals, derivatives of the space-dependent functions are often found in the integrand. The derivatives with respect to spatial coordinates operate on the basis functions: $\boldsymbol{\nabla}\phi(\boldsymbol{r}) = \sum_{i=1}^{N_b} \boldsymbol{\nabla} W_i(\boldsymbol{r})\ \phi_i$. Differentiation of the basis functions of order N_p will give polynomials of order $N_p - 1$. Since a polynomial of order $N_p - 1$ can be written in terms of all the polynomials of order N_p, Silvester [91] introduced the differentiation matrices

$$\frac{\partial W_\alpha}{\partial x_i} = \sum_{\beta=1}^{N_b} \sum_{j=1}^{n} c_{ij} D^j_{\alpha\beta} W_\beta. \tag{3.38}$$

Using the orthonormal property of the basis functions and equation (3.28), the differentiation matrices are given by

$$D^i_{\alpha\beta} = \left.\frac{\partial W_\alpha}{\partial \xi_i}\right|_{\text{node } \beta} \quad \text{and } c_{ij} = \frac{\partial \xi_j}{\partial x_i}. \tag{3.39}$$

From the construction of the basis polynomial function W_α, equation (3.32), the derivative of $W(\boldsymbol{r})$ with respect to ξ_i is

$$\frac{\partial W_\alpha}{\partial \xi_i} = \left[R_{\alpha_0}(N_p, \xi_0) \frac{\partial R_{\alpha_i}(N_p, \xi_i)}{\partial \xi_i} - \left.\frac{\partial R_{\alpha_0}(N_p, \xi)}{\partial \xi}\right|_{\xi=\xi_0} R_{\alpha_i}(N_p, \xi_i) \right] \cdot \prod_{\substack{j=1 \\ j\neq i}}^{n} R_{\alpha_j}(N_p, \xi_j) \tag{3.40}$$

where $\xi_0 = 1 - \sum_{i=1}^{n} \xi_i$ by the closure relation. Derivatives of the basic polynomials $R_{\alpha_i}(N_p, \xi_i)$ are obtained by differentiation of equation (3.33):

$$\frac{\partial R_m(N,\xi)}{\partial \xi} = \begin{cases} N/m! \sum_{l=0}^{m-1} \prod_{\substack{k=0 \\ k\neq l}}^{m-1} (N\xi - k) & m > 1 \\ N/m! & m = 1 \\ 0 & m = 0 \end{cases} . \tag{3.41}$$

By substituting equation (3.40) into equation (3.39) and using equation (3.30) to evaluate the simplex coordinates at nodes, the differentiation matrices become:

$$D^i_{\alpha\beta} = \left.\frac{\partial R_{\alpha_i}(N_p,\xi_i)}{\partial \xi_i}\right|_{\xi_i=\beta_i/N_p} \prod_{\substack{j=0 \\ j\neq i}}^{n} R_{\alpha_j}(N_p,\beta_j/N_p) . \tag{3.42}$$

For a given spatial dimensionality and polynomial order of the basis functions, the differentiation matrices need only be computed once for all the elements; they form a set of universal matrices. The particular geometry of an element is taken into account by the Jacobians and the c_{ij} coefficients when any one particular element is formed. These are element specific: they depend on the geometry of the element and on the polynomial order of the basis functions, but not on the coordinates. As a consequence, no element specific integrals need to be computed.

The transformation from global geometric coordinates to simplex coordinates and the set of $\{\alpha_i,\ i = 0 \ldots n\}$ for each node of the element is all that is required to compute the above universal matrices and geometric coefficients ($\mathcal{J}$ and c_{ij}). Details are given in the following subsections for the line and triangle elements.

Line element

The spatially one-dimensional case ($n = 1$) is the line element. Figure 3.2 illustrates a typical element. The transformation between the geometric coordinates to the local coordinates is

$$\xi_1 = \frac{1}{a_1 - a_0}(-a_0 + x_1) . \tag{3.43}$$

The Jacobian of this transformation is the element length; $\mathcal{J} = (a_1 - a_0)$. The basis functions given by equation (3.29) are

$$W_\alpha(\xi_1) = R_{\alpha_0}(N_p, 1-\xi_1) R_{\alpha_1}(N_p,\xi_1) , \tag{3.44}$$

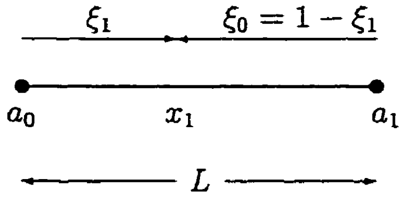

Figure 3.2: Typical spatially one-dimensional element. The element size is L; a_0 and a_1 are the end points of the element; x_1 and ξ_1 are the geometric and simplex coordinates respectively.

where the closure relation given by equation (3.31) has been used to eliminate ξ_0. Table 3.1 defines α_0 and α_1 at each node. The number of basis functions is $N_b = N_p + 1$.

nodes α	polynomial order $N_p = 1$ (α_0, α_1)	 $N_p = 2$ (α_0, α_1)	 $N_p = 3$ (α_0, α_1)
1	1,0	2,0	3,0
2	0,1	1,1	2,1
3		0,2	1,2
4			0,3

Table 3.1: Node numbering for the line element. At each node α the pair (α_0, α_1) indicates the values of the simplex coordinates ξ_0 and ξ_1 respectively.

Triangle element

The triangle element is taken for the spatially two-dimensional case ($n = 2$). This element shape can be used to decompose a polygon of any shape. Figure 3.3 illustrates a typical element. The transformation between the geometric coordinates and the local coordinates is

$$\begin{pmatrix} \xi_1 \\ \xi_2 \end{pmatrix} = \mathcal{J}^{-1} \begin{pmatrix} y_{10} & y_{11} & y_{12} \\ y_{20} & y_{21} & y_{22} \end{pmatrix} \begin{pmatrix} 1 \\ x_1 \\ x_2 \end{pmatrix} \tag{3.45}$$

where

$$\begin{aligned} y_{10} &= a_2 b_0 - a_0 b_2, \\ y_{11} &= b_2 - b_0, \; y_{12} = a_0 - a_2, \\ y_{20} &= a_0 b_1 - a_1 b_0, \\ y_{21} &= b_0 - b_1, \; y_{22} = a_1 - a_0. \end{aligned}$$

The Jacobian of the transformation is twice the element area; $\mathcal{J} = 2A$, which

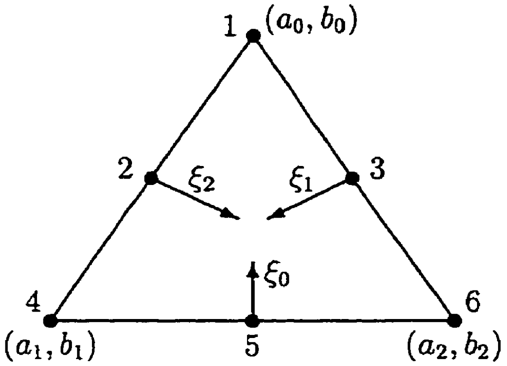

Figure 3.3: Typical triangular element. The edges of the triangle are (a_i, b_i), (i=0 to 2) in the geometric coordinates (x_1, x_2). Nodes are shown for the case of interpolation polynomials of order 2 ($N_p = 2$).

is computed as

$$A = \frac{1}{2!} \begin{vmatrix} 1 & a_0 & b_0 \\ 1 & a_1 & b_1 \\ 1 & a_2 & b_2 \end{vmatrix} .$$

The basis functions given by equation (3.29), after using the closure relation given by equation (3.31) to eliminate ξ_0, are

$$\begin{aligned} W_\alpha(\xi_1, \xi_2) &= R_{\alpha_0}(N_p, 1 - \xi_1 - \xi_2) \\ & \quad R_{\alpha_1}(N_p, \xi_1) R_{\alpha_2}(N_p, \xi_2) . \end{aligned} \tag{3.46}$$

The number of basis functions is $N_b = (N_p + 1)(N_p + 2)/2$.

Table 3.2 defines α_0, α_1 and α_2 at each node. The differentiation matrix $D^2_{\alpha\beta}$ can be obtained from $D^1_{\alpha\beta}$ by application of a permutation operator P

$$\mathrm{D}^2 = \mathrm{P}\ \mathrm{D}^1\ \mathrm{P}^T . \tag{3.47}$$

nodes	polynomial order		
	$N_p = 1$	$N_p = 2$	$N_p = 3$
α	$(\alpha_0, \alpha_1, \alpha_2)$	$(\alpha_0, \alpha_1, \alpha_2)$	$(\alpha_0, \alpha_1, \alpha_2)$
1	1,0,0	2,0,0	3,0,0
2	0,1,0	1,1,0	2,1,0
3	0,0,1	1,0,1	2,0,1
4		0,2,0	1,2,0
5		0,1,1	1,1,1
6		0,0,2	1,0,2
7			0,3,0
8			0,2,1
9			0,1,2
10			0,0,3

Table 3.2: Node numbering for the triangular element. At each node α the triple $(\alpha_0, \alpha_1, \alpha_2)$ indicates the values of the simplex coordinates ξ_0, ξ_1 and ξ_2 respectively.

Simplex elements possess topological symmetries that can be used to reduce the number of matrices that must be computed, as identified by Silvester [92]. The permutation operator transforms the node $\alpha(\alpha_0, \alpha_1, \alpha_2)$ into the node $\alpha'(\alpha_0, \alpha_2, \alpha_1)$ corresponding to a "flipover" of the triangle shown in Figure 3.3. The permutation operator P is block diagonal, each block being left-diagonal of increasing size. The permutation matrix for basis functions of polynomial order N_p is the sub-matrix that comprises the first N_b rows and columns of the permutation matrix for basis functions of polynomial order $N_p + 1$. For basis functions of polynomial order one and two, the permutation operators are

$$\mathrm{P} = \begin{pmatrix} 1 & & \\ & 0 & 1 \\ & 1 & 0 \end{pmatrix} \text{ and } \mathrm{P} = \begin{pmatrix} 1 & & & & & \\ & 0 & 1 & & & \\ & 1 & 0 & & & \\ & & & 0 & 0 & 1 \\ & & & 0 & 1 & 0 \\ & & & 1 & 0 & 0 \end{pmatrix} \tag{3.48}$$

respectively. For polynomial order three, the permutation matrix is given by

$$\mathrm{P} = \begin{pmatrix} 1 &&&&&&&&& \\ & 0 & 1 &&&&&&& \\ & 1 & 0 &&&&&&& \\ &&& 0 & 0 & 1 &&&& \\ &&& 0 & 1 & 0 &&&& \\ &&& 1 & 0 & 0 &&&& \\ &&&&&& 0 & 0 & 0 & 1 \\ &&&&&& 0 & 0 & 1 & 0 \\ &&&&&& 0 & 1 & 0 & 0 \\ &&&&&& 1 & 0 & 0 & 0 \end{pmatrix}. \tag{3.49}$$

The multiple-product universal matrices for two dimensions are given by

$$T_{\alpha\beta} = \int_{\xi_2=0}^{1} \int_{\xi_1=0}^{1-\xi_2} W_\alpha W_\beta \; d\xi_1 d\xi_2,$$

and similarly for the $Q_{\alpha\beta\gamma}$ and $V_{\alpha\beta\gamma\sigma}$ matrices defined by equations (3.36) and (3.37) respectively.

Tetrahedral element

The tetrahedral element is taken for the spatially three-dimensional case ($n = 3$). Figure 3.4 illustrates a typical element. The transformation between the geometric coordinates and the local coordinates is

$$\begin{pmatrix} \xi_1 \\ \xi_2 \\ \xi_3 \end{pmatrix} = \mathcal{J}^{-1} \begin{pmatrix} y_{10} & y_{11} & y_{12} & y_{13} \\ y_{20} & y_{21} & y_{22} & y_{23} \\ y_{30} & y_{31} & y_{32} & y_{33} \end{pmatrix} \begin{pmatrix} 1 \\ x_1 \\ x_2 \\ x_3 \end{pmatrix}. \tag{3.50}$$

The matrix elements of the transformation matrix are:

$$\begin{aligned}
y_{10} &= (a_3 b_2 - a_2 b_3)c_0 + (a_0 b_3 - a_3 b_0)c_2 + (a_2 b_0 - a_0 b_2)c_3 \\
y_{11} &= (b_3 - b_2)c_0 + (b_0 - b_3)c_2 + (b_2 - b_0)c_3 \\
y_{12} &= (a_2 - a_3)c_0 + (a_3 - a_0)c_2 + (a_0 - a_2)c_3 \\
y_{13} &= (a_3 - a_2)b_0 + (a_0 - a_3)b_2 + (a_2 - a_0)b_3 \\
y_{20} &= (a_1 b_3 - a_3 b_1)c_0 + (a_3 b_0 - a_0 b_3)c_1 + (a_0 b_1 - a_1 b_0)c_3 \\
y_{21} &= (b_1 - b_3)c_0 + (b_3 - b_0)c_1 + (b_0 - b_1)c_3 \\
y_{22} &= (a_3 - a_1)c_0 + (a_0 - a_3)c_1 + (a_1 - a_0)c_3 \\
y_{23} &= (a_1 - a_3)b_0 + (a_3 - a_0)b_1 + (a_0 - a_1)b_3 \\
y_{30} &= (a_2 b_1 - a_1 b_2)c_0 + (a_0 b_2 - a_2 b_0)c_1 + (a_1 b_0 - a_0 b_1)c_2 \\
y_{31} &= (b_2 - b_1)c_0 + (b_0 - b_2)c_1 + (b_1 - b_0)c_2 \\
y_{32} &= (a_1 - a_2)c_0 + (a_2 - a_0)c_1 + (a_0 - a_1)c_2 \\
y_{33} &= (a_2 - a_1)b_0 + (a_0 - a_2)b_1 + (a_1 - a_0)b_2
\end{aligned}$$

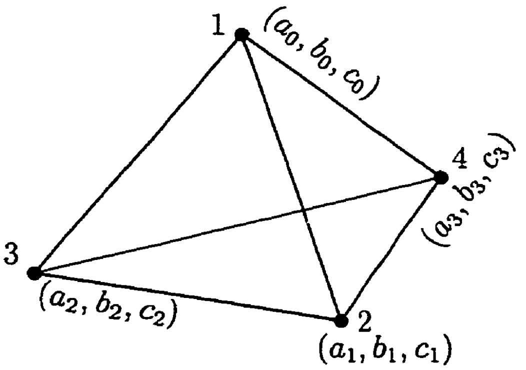

Figure 3.4: Typical tetrahedral element. The edges of the element are (a_i, b_i, c_i), (i=0 to 3) in the geometric coordinates (x_1, x_2, x_3). Nodes are shown for the case of linear interpolation ($N_p = 1$).

The Jacobian of the transformation is twice the element volume; $\mathcal{J} = 2V$, which is

$$V = \frac{1}{3!}\begin{vmatrix} 1 & a_0 & b_0 & c_0 \\ 1 & a_1 & b_1 & c_1 \\ 1 & a_2 & b_2 & c_2 \end{vmatrix}$$

The basis functions, which are given by equation (3.29) using the closure relation given by equation (3.31) for eliminating ξ_0, are

$$\begin{aligned} W_\alpha(\xi_1, \xi_2, \xi_3) &= R_{\alpha_0}(N_p, 1 - \xi_1 - \xi_2 - \xi_2)\, R_{\alpha_1}(N_p, \xi_1) \\ &\quad R_{\alpha_2}(N_p, \xi_2)\, R_{\alpha_3}(N_p, \xi_3)\,. \end{aligned} \tag{3.51}$$

The number of basis functions is $N_b = (N_p + 1)(N_p + 2)(N_p + 3)/6$.

Table 3.3 defines α_0, α_1, α_2 and α_3 at each node. The differentiation matrices $D^2_{\alpha\beta}$ and $D^3_{\alpha\beta}$ can be obtained from $D^1_{\alpha\beta}$ by application of permutation operators P^{12} and P^{13} respectively:

$$\mathrm{D}^2 = \mathrm{P}^{12}\, \mathrm{D}^1\, \mathrm{P}^{12^T} \text{ and } \mathrm{D}^3 = \mathrm{P}^{13}\, \mathrm{D}^1\, \mathrm{P}^{13^T}. \tag{3.52}$$

nodes	polynomial order $N_p = 1$	$N_p = 2$	$N_p = 3$
α	$(\alpha_0, \alpha_1, \alpha_2, \alpha_3)$	$(\alpha_0, \alpha_1, \alpha_2, \alpha_3)$	$(\alpha_0, \alpha_1, \alpha_2, \alpha_3)$
1	1,0,0,0	2,0,0,0	3,0,0,0
2	0,1,0,0	1,1,0,0	2,1,0,0
3	0,0,1,0	1,0,1,0	2,0,1,0
4	0,0,0,1	1,0,0,1	2,0,0,1
5		0,2,0,0	1,2,0,0
6		0,1,1,0	1,1,1,0
7		0,1,0,1	1,1,0,1
8		0,0,2,0	1,0,2,0
9		0,0,1,1	1,0,1,1
10		0,0,0,2	1,0,0,2
11			0,3,0,0
12			0,2,1,0
13			0,2,0,1
14			0,1,2,0
15			0,1,1,1
16			0,1,0,2
17			0,0,3,0
18			0,0,2,1
19			0,0,1,2
20			0,0,0,3

Table 3.3: Node numbering for the tetrahedral element. At each node α the quadruple $(\alpha_0, \alpha_1, \alpha_2, \alpha_3)$ indicates the value of the simplex coordinates ξ_0, ξ_1, ξ_2 and ξ_3 respectively.

The permutation operator P^{12} is defined to transform the node $\alpha(\alpha_0, \alpha_1, \alpha_2, \alpha_3)$ into the node $\alpha'(\alpha_0, \alpha_2, \alpha_1, \alpha_3)$, similarly the permutation operator P^{13} is defined to transform the node $\alpha(\alpha_0, \alpha_1, \alpha_2, \alpha_3)$ into the node $\alpha'(\alpha_0, \alpha_3, \alpha_2, \alpha_1)$. The permutation operators are block diagonal, each block being of increasing size.

As for the triangle element, the permutation matrix for the basis functions of polynomial order N_p is the sub-matrix made of the first N_b rows and columns of the permutation matrix for basis functions of polynomial order $N_p + 1$. For polynomial order up to three, the permutation matrix P^{12} is given by

$$
\mathrm{P}^{12} = \left(\begin{array}{cccccccccccccccccccc}
1 & & & & & & & & & & & & & & & & & & & \\
 & 0 & 1 & 0 & & & & & & & & & & & & & & & & \\
 & 1 & 0 & 0 & & & & & & & & & & & & & & & & \\
 & 0 & 0 & 1 & & & & & & & & & & & & & & & & \\
 & & & & 0 & 0 & 0 & 1 & 0 & 0 & & & & & & & & & & \\
 & & & & 0 & 1 & 0 & 0 & 0 & 0 & & & & & & & & & & \\
 & & & & 0 & 0 & 0 & 0 & 1 & 0 & & & & & & & & & & \\
 & & & & 1 & 0 & 0 & 0 & 0 & 0 & & & & & & & & & & \\
 & & & & 0 & 0 & 1 & 0 & 0 & 0 & & & & & & & & & & \\
 & & & & 0 & 0 & 0 & 0 & 0 & 1 & & & & & & & & & & \\
 & & & & & & & & & & 0 & 0 & 0 & 0 & 0 & 0 & 1 & 0 & 0 & 0 \\
 & & & & & & & & & & 0 & 0 & 0 & 1 & 0 & 0 & 0 & 0 & 0 & 0 \\
 & & & & & & & & & & 0 & 0 & 0 & 0 & 0 & 0 & 0 & 1 & 0 & 0 \\
 & & & & & & & & & & 0 & 1 & 0 & 0 & 0 & 0 & 0 & 0 & 0 & 0 \\
 & & & & & & & & & & 0 & 0 & 0 & 0 & 1 & 0 & 0 & 0 & 0 & 0 \\
 & & & & & & & & & & 0 & 0 & 0 & 0 & 0 & 0 & 0 & 0 & 1 & 0 \\
 & & & & & & & & & & 1 & 0 & 0 & 0 & 0 & 0 & 0 & 0 & 0 & 0 \\
 & & & & & & & & & & 0 & 0 & 1 & 0 & 0 & 0 & 0 & 0 & 0 & 0 \\
 & & & & & & & & & & 0 & 0 & 0 & 0 & 0 & 1 & 0 & 0 & 0 & 0 \\
 & & & & & & & & & & 0 & 0 & 0 & 0 & 0 & 0 & 0 & 0 & 0 & 1
\end{array}\right). \tag{3.53}
$$

3.2.2 Integrals on surfaces

An inherent strength of the finite element method is the simplicity and rigor in the application of the boundary conditions. These are generally auxiliary equations for the unknown fields at the surface enclosing the spatial domain of the problem. The universal matrices defined in the previous section can be used for the evaluation of the surface integrals arising in most weak formulations.

An important property of the simplex elements is that an element of spatial dimensionality n has its boundary made of $n+1$ elements of spatial dimensionality $n-1$. This property follows directly from the construction of the polynomial basis functions $W_\alpha(\boldsymbol{r})$ chosen. Recall a typical member of the set of basis functions, equation (3.29):

$$
W_\alpha(\xi_0, \ldots, \xi_n) = \prod_{i=0}^{n} R_{\alpha_i}\left(N_p, \xi_i\right). \tag{3.54}
$$

As shown in Figures 3.2 and 3.3, the simplex coordinate ξ_i corresponds to the distance from an internal point $\boldsymbol{P}$ to the surface i of the element [1]. Define Σ_i as the surface i for which every point on that surface has $\xi_i = 0$. The non-zero basis functions on that surface are those having $\alpha_i = 0$ since $R_{\alpha_i}(N_p, 0) = \delta_{\alpha_i 0}$ where $\delta_{\alpha\beta}$ is the Kronecker delta. As a result, the member α of the basis functions defined for the n-dimensional element evaluated on the surface Σ_i of the element is:

$$W_\alpha|_{\Sigma_i} = \prod_{\substack{j=0 \\ j\neq i}}^{n} R_{\alpha_j}(N_p, \xi_i) = W_{\alpha'}^{(n-1)} \tag{3.55}$$

where $W_{\alpha'}^{(n-1)}$ is the member α' of the basis functions defined for the $(n-1)$-dimensional element. Lookup tables are defined in Tables 3.4 and 3.5 to relate α' to α as functions of the surface Σ_i for the case $n = 2$ and $n = 3$ respectively. These tables are constructed by inspection of the node numbering tables, Tables 3.1, 3.2, and 3.3, for the respective elements.

$N_p = 1$				$N_p = 2$				$N_p = 3$			
α on surface				α on surface				α on surface			
Σ_0	Σ_1	Σ_2	α'	Σ_0	Σ_1	Σ_2	α'	Σ_0	Σ_1	Σ_2	α'
2	1	1	1	4	1	1	1	7	1	1	1
3	3	2	2	5	3	2	2	8	3	2	2
				6	6	4	3	9	6	4	3
								10	10	7	4

Table 3.4: Lookup tables for equation (3.55), they relate triangle element's nodes α on faces Σ_i, $i = 0$ to 2, to corresponding nodes α' of the line element.

Consider the integration of a product of two basis functions on a surface or face Σ_i of an n-dimensional element:

$$\mathcal{J}_{\Sigma_i}^{-1} \int_{\Sigma_i} W_\alpha W_\beta \, d\Sigma = \int_\Omega W_{\alpha'}^{(n-1)} W_{\beta'}^{(n-1)} \, d\Omega = T_{\alpha'\beta'}^{(n-1)}. \tag{3.56}$$

Here Σ_i is the surface i of the n-dimensional element in geometric coordinates while Ω is the volume of the $(n-1)$-dimensional element in simplex coordinates.

---

[1] In this section, the terms *surface* and *volume* are used in a generalized sense. The volume of a n-dimensional elements is the region delimited by the surfaces making the boundary of the element.

The relation between α' and α, as well β' and β, is given in Tables 3.4 and 3.5 as functions of the surface Σ_i. The matrix $T^{(n-1)}_{\alpha'\beta'}$ is the double-product matrix, equation (3.35), for the $(n-1)$-dimensional element. For the case where $n = 1$ the integral reduces trivially to $T^{(0)}_{\alpha\beta} = \delta_{\alpha\beta}$. The Jacobian $\mathcal{J}^{-1}_{\Sigma_i}$ corresponds to the (generalized) area of the surface in the n-dimensional space.

$N_p = 1$					$N_p = 2$					$N_p = 3$				
α on surface				α'	α on surface				α'	α on surface				α'
Σ_0	Σ_1	Σ_2	Σ_3		Σ_0	Σ_1	Σ_2	Σ_3		Σ_0	Σ_1	Σ_2	Σ_3	
2	1	1	1	1	5	1	1	1	1	11	1	1	1	1
3	3	2	2	2	6	3	2	2	2	12	3	2	2	2
4	4	4	3	3	7	4	4	3	3	13	4	4	3	3
					8	8	5	5	4	14	8	5	5	4
					9	9	7	6	5	15	9	7	6	5
					10	10	10	8	6	16	10	10	8	6
										17	17	11	11	7
										18	18	13	12	8
										19	19	16	14	9
										20	20	20	17	10

Table 3.5: Lookup tables for equation (3.55), they relate tetrahedral element's nodes α on surfaces Σ_i, $i = 0$ to 2, to corresponding nodes α' of the triangle element.

Consider a parallelogram in three dimensional space having $\boldsymbol{A}$ and $\boldsymbol{B}$ as coterminal sides. Its area is given by $\|\boldsymbol{A} \times \boldsymbol{B}\|$, writing

$$\boldsymbol{A} \times \boldsymbol{B} = \begin{vmatrix} \boldsymbol{e}_1 & a_1 & b_1 \\ \boldsymbol{e}_2 & a_2 & b_2 \\ \boldsymbol{e}_3 & a_3 & b_3 \end{vmatrix}$$

where $\boldsymbol{e}_i$ is the unit vector in the direction i in the geometric coordinate, $\boldsymbol{A} = \sum_{i=1}^{3} a_i \boldsymbol{e}_i$, and $\boldsymbol{B} = \sum_{i=1}^{3} b_i \boldsymbol{e}_i$. This can be generalized to n dimensions. The Jacobian is $\mathcal{J}_\Sigma = (n-1)! A_n$ where the area A_n can be computed as the n-norm of the vector:

$$A_n = \frac{1}{(n-1)!} \begin{vmatrix} \boldsymbol{e}_1 & a_1^1 - a_1^0 & a_1^2 - a_1^0 & \dots & a_1^{n-1} - a_1^0 \\ \boldsymbol{e}_2 & a_2^1 - a_2^0 & a_2^2 - a_2^0 & \dots & a_2^{n-1} - a_2^0 \\ \vdots & \vdots & \vdots & & \vdots \\ \boldsymbol{e}_n & a_n^1 - a_n^0 & a_n^2 - a_n^0 & \dots & a_n^{n-1} - a_n^0 \end{vmatrix} \tag{3.57}$$

where the surface is defined using n nodes each having n coordinates, e.g., node i is defined with coordinates $(a^i_1, a^i_2, \ldots, a^i_n)$, i=0 to $n-1$.

In practical applications, the surface integrals often involve the gradient normal to the surface of the unknown field. As an example, consider the following surface integral:

$$\int_{\Sigma_i} \hat{\boldsymbol{S}} \cdot \nabla W_\alpha \; W_\beta \, d\Sigma = \mathcal{J}_{\Sigma_i} \sum_{\delta}^{\text{on } \Sigma_i} \sum_{i,j=1}^{n} \hat{S}_i c_{ij} D^j_{\alpha\delta} \int_\Omega W^{(n-1)}_{\alpha'} W^{(n-1)}_{\beta'} \, d\Omega \tag{3.58}$$

where $\hat{\boldsymbol{S}}$ is a unit vector normal to the surface pointing outward from the enclosed element defined in the global coordinate system, its components are defined as $\hat{S}_i = \hat{\boldsymbol{S}} \cdot \boldsymbol{e}_i$. We used the differentiation matrices defined in equation (3.38). Using the double-product matrix for the $(n-1)$-dimensional element we get:

$$\int_{\Sigma_i} \hat{\boldsymbol{S}} \cdot \nabla W_\alpha \; W_\beta \, d\Sigma = \mathcal{J}_{\Sigma_i} \sum_{\delta}^{\text{on } \Sigma_i} \sum_{i,j=1}^{n} \hat{S}_i c_{ij} D^j_{\alpha\delta} T^{(n-1)}_{\alpha'\beta'}. \tag{3.59}$$

3.3 Weighted residuals using universal matrices

The spatial domain of the dependent variables is projected onto the polynomial basis function of order N_p (see section 3.2.1):

$$\begin{aligned} \phi(\boldsymbol{x},\tau) &= \sum_{\alpha=1}^{N_b} W_\alpha(\boldsymbol{x}) \; \phi_\alpha(\tau), \\ n^+(\boldsymbol{x},\tau) &= \sum_{\alpha=1}^{N_b} W_\alpha(\boldsymbol{x}) \; n^+_\alpha(\tau), \\ n^-(\boldsymbol{x},\tau) &= \sum_{\alpha=1}^{N_b} W_\alpha(\boldsymbol{x}) \; n^-_\alpha(\tau), \text{ and} \\ T^-(\boldsymbol{x},\tau) &= \sum_{\alpha=1}^{N_b} W_\alpha(\boldsymbol{x}) \; T^-_\alpha(\tau), \end{aligned} \tag{3.60}$$

where each spatial element has N_b nodes at which the unknown fields are computed. Here the unknown fields are still time-dependent. To lighten the notation we will use ϕ_α to indicate the time-dependent unknown field $\phi(\boldsymbol{x},\tau)$ at spatial node α.

The new expression for the electric potential residual R^{ϕ}_{α}, equation (3.11), after projection of dependent variables, is given by:

$$R^{\phi}_{\alpha} = \sum_{\delta=1}^{N_b} \left[\phi_\delta \int_{\Omega} \nabla W_\delta \cdot \nabla W_\alpha d\Omega - Q \left(n^{+}_{\delta} - n^{-}_{\delta} \right) \int_{\Omega} W_\delta W_\alpha d\Omega \right], \tag{3.61}$$

where the surface integral has been omitted (the surface terms will be discussed in the next section). Transforming the integral into the element's local coordinate system and using the differentiation matrix for the derivative of the basis functions as in equation (3.38), and using the double-product matrix defined by the equations (3.35) gives:

$$R^{\phi}_{\alpha} = \mathcal{J} \sum_{\delta,\eta,\kappa=1}^{N_b} \phi_\delta \sum_{i,j,k=1}^{n} c_{ij} c_{ik} D^{j}_{\delta\eta} D^{k}_{\alpha\kappa} T_{\eta\kappa} - \mathcal{J} Q \sum_{\delta=1}^{N_b} \left(n^{+}_{\delta} - n^{-}_{\delta} \right) T_{\delta\alpha}. \tag{3.62}$$

The same procedure is used for the residuals R^{-}_{α}, R^{+}_{α}, and R^{T}_{α}, equations (3.12), (3.13), and (3.14) respectively. Substituting the expression for the electron flux, equation (2.70), into the residual R^{-}_{α}, equation (3.12), we get:

$$R^{-}_{\alpha} = \int_{\Omega} \left[\Gamma \frac{\partial n^{-}}{\partial \tau} W_\alpha + \left(\nabla n^{-} - M^{-} n^{-} \nabla \phi \right) \cdot \nabla W_\alpha - A_z n^{-} F_z W_\alpha \right] d\Omega. \tag{3.63}$$

We project the unknown fields, as in equation (3.60), and using the universal matrices, the residual becomes:

$$\begin{aligned} R^{-}_{\alpha} \quad = \quad & \mathcal{J} \Gamma \sum_{\delta=1}^{N_b} \frac{\partial n^{-}_{\delta}}{\partial \tau} T_{\delta\alpha} + \mathcal{J} \sum_{\delta,\eta,\kappa=1}^{N_b} n^{-}_{\delta} \sum_{i,j,k=1}^{n} c_{ij} c_{ik} D^{j}_{\delta\eta} D^{k}_{\alpha\kappa} T_{\eta\kappa} - \\ & \mathcal{J} \sum_{\delta,\eta,\kappa,\lambda=1}^{N_b} M^{-} n^{-}_{\delta} \phi_\eta \sum_{i,j,k=1}^{n} c_{ij} c_{ik} D^{j}_{\eta\kappa} D^{k}_{\alpha\lambda} Q_{\delta\kappa\lambda} - \\ & \mathcal{J} A_z \sum_{\delta,\eta=1}^{N_b} n^{-}_{\delta} F^{z}_{\eta} Q_{\delta\eta\alpha}. \end{aligned} \tag{3.64}$$

The same procedure is repeated for the residual of the ion density continuity equation, (3.13):

$$\begin{aligned} R^{+}_{\alpha} \quad = \quad & \mathcal{J} \Gamma \beta \sum_{\delta=1}^{N_b} \frac{\partial n^{+}_{\delta}}{\partial \tau} T_{\delta\alpha} + \mathcal{J} \sum_{\delta,\eta,\kappa=1}^{N_b} n^{+}_{\delta} \sum_{i,j,k=1}^{n} c_{ij} c_{ik} D^{j}_{\delta\eta} D^{k}_{\alpha\kappa} T_{\eta\kappa} + \\ & \mathcal{J} M^{+} \sum_{\delta,\eta,\kappa,\lambda=1}^{N_b} n^{+}_{\delta} \phi_\eta \sum_{i,j,k=1}^{n} c_{ij} c_{ik} D^{j}_{\eta\kappa} D^{k}_{\alpha\lambda} Q_{\delta\kappa\lambda} - \\ & \mathcal{J} A_z \beta \sum_{\delta,\eta=1}^{N_b} n^{-}_{\delta} F^{z}_{\eta} Q_{\delta\eta\alpha}. \end{aligned} \tag{3.65}$$

Similarly for the electron temperature residual, equation (3.14), using equation (2.70) for the electron flux density, equation (2.73) for the electron thermal conductivity, and equation (2.74) for the energy transfer function, residual R_α^T becomes:

$$\begin{aligned}
R_\alpha^T \;=\; & \mathcal{J}\Gamma \sum_{\delta,\eta=1}^{N_b} \left(\frac{3}{5} n_\delta^- \frac{\partial T_\eta^-}{\partial \tau} - \frac{2}{5} \frac{\partial n_\delta^-}{\partial \tau} T_\eta^- \right) Q_{\delta\eta\alpha} - \\
& \mathcal{J} \sum_{\delta,\eta,\kappa,\lambda=1}^{N_b} n_\delta^- \left(T_\kappa^- - J_o \phi_\kappa \right) \sum_{i,j,k=1}^{n} c_{ij} c_{ik} D_{\delta\eta}^j D_{\kappa\lambda}^k Q_{\eta\lambda\alpha} + \\
& \mathcal{J} M^- \sum_{\delta,\eta,\kappa,\lambda,\rho=1}^{N_b} n_\delta^- \phi_\eta \left(T_\lambda^- - J_o \phi_\lambda \right) \sum_{i,j,k=1}^{n} c_{ij} c_{ik} D_{\eta\kappa}^j D_{\lambda\rho}^k V_{\delta\kappa\rho\alpha} + \\
& \mathcal{J} \sum_{\delta,\eta,\kappa,\lambda,\rho=1}^{N_b} n_\delta^- T_\eta^- T_\lambda^- \sum_{i,j,k=1}^{n} c_{ij} c_{ik} D_{\lambda\kappa}^j D_{\alpha\rho}^k V_{\delta\eta\kappa\rho} + \\
& \mathcal{J} A_z \sum_{\delta,\eta,\kappa=1}^{N_b} n_\delta^- T_\eta^- F_\kappa^z V_{\delta\eta\kappa\alpha} + \mathcal{J} A_Z \sum_{\delta,\eta=1}^{N_b} n_\delta^- \sum_{Z=1}^{nz} H_Z F_\eta^Z Q_{\delta\eta\alpha}, \qquad (3.66)
\end{aligned}$$

where n is the spatial dimensionality and N_b is the number of basis functions: $N_b = (N_p + n)!/(n!\, N_p!)$. The weighted residuals, equations (3.11), (3.13), (3.12), and (3.14), are integrals of various products of space-dependent functions. These integrals are replaced by sums and products of matrices, as per equations (3.62), (3.65), (3.64), and (3.66) respectively, without having to specify the element shape, dimensionality, or order. Therefore, mixing elements of various shapes with the same order would be straightforward. The particular geometry of an element is considered by the Jacobian, $\mathcal{J}$, and the coefficients c_{ij}, while the differentiation matrices $D_{\alpha\beta}^k$ and the multiple-product matrices, $T_{\alpha\beta}$, $Q_{\alpha\beta\sigma}$, and $V_{\alpha\beta\sigma\tau}$ are each universal for all elements of a given shape and order.

In the following section the surface terms of the residuals are expressed in terms of the universal matrices.

3.3.1 Surface terms using universal matrices

The surface integrals are computed using the multiple-product universal matrices for simplex elements of dimensionality $n - 1$ as presented in section 3.2.2.

The surface terms arising in the residuals R_α^ϕ and $R_\alpha^{\phi_D}$, equation (3.16), projected on the polynomial basis functions with the integrals replaced by universal matrices give:

$$R_\alpha^{\phi,D} + R_\alpha^{\phi_D,D} = -\mathcal{J}_{\Sigma_k} \frac{\epsilon_r - 1}{\epsilon_r} \sum_{\substack{\delta,\eta=1 \\ (\eta \text{ on } \Sigma_k)}}^{N_b} \phi_\delta \sum_{i,j=1}^{n} \hat{S}_i c_{ij} D^j_{\delta\eta} T^{(n-1)}_{\eta'\alpha'} - \frac{Q}{\epsilon_r} \sum_{\delta}^{\text{on } \Sigma_k} (\sigma_\delta^+ - \sigma_\delta^-) T^{(n-1)}_{\delta'\alpha'}, \tag{3.67}$$

where: $\mathcal{J}_{\Sigma_k}$ is the Jacobian of the transformation between the global coordinates and the local coordinates of the surface Σ_k; k is the face number of the surface; and the lookup tables for $\eta' = \eta'(\Sigma_k, \eta)$ (and all other indexes marked with a prime) are given by Tables 3.4 and 3.5. The components of the projected unit normal vector of the surface, $\hat{\boldsymbol{S}}$, on the global coordinate i, are $\hat{S}_i = \hat{\boldsymbol{S}} \cdot \boldsymbol{e}_i$. Note that the normal vector to the surface is $S_i = \mathcal{J}_{\Sigma_k} \hat{\boldsymbol{S}} \cdot \boldsymbol{e}_i$, see section 3.2.2.

The surface terms of the residual of the ion continuity equation, equation (3.18), are given in terms of the universal matrices as:

$$R_\alpha^{+,\Sigma} = -\mathcal{J}_\Sigma M^+ \sum_{\substack{\delta,\eta,\kappa=1 \\ (\delta,\kappa \text{ on } \Sigma)}}^{N_b} n_\delta^+ \phi_\eta \sum_{i,j=1}^{n} \hat{S}_i c_{ij} D^j_{\eta\kappa} Q^{(n-1)}_{\delta'\kappa'\alpha'}, \tag{3.68}$$

where Σ is a surface that encloses the plasma, including the electrodes and the dielectric barrier interface.

The surface integral contribution to the electron continuity equation residual, equation (3.20), is:

$$R_\alpha^{-,A} = \mathcal{J}_{\Sigma_A} k_R \sum_{\delta,\gamma}^{\text{on } \Sigma_A} n_\delta^- \left(T_\gamma^-\right)^{1/2} Q^{(n-1)}_{\delta'\gamma'\alpha'} \tag{3.69}$$

at the anode. At the cathode the surface integral $R_\alpha^{-,C}$, equation (3.21), remains proportional to $R_\alpha^{+,C}$. At the dielectric barrier surface the integral $R_\alpha^{-,D}$, equation (3.22), becomes:

$$R_\alpha^{-,D} = \mathcal{J}_{\Sigma_D} k_-^\sigma \sum_{\delta}^{\text{on } \Sigma_D} n_\delta^- T^{(n-1)}_{\delta'\alpha'} + \mathcal{J}_{\Sigma_D} \gamma^\sigma M^+ \beta^{-1} \sum_{\substack{\delta,\eta,\kappa=1 \\ (\delta,\kappa \text{ on } \Sigma_D)}}^{N_b} n_\delta^+ \phi_\eta \sum_{i,j=1}^{n} \hat{S}_i c_{ij} D^j_{\eta\kappa} Q^{(n-1)}_{\delta'\kappa'\alpha'}. \tag{3.70}$$

The electron attachment to the dielectric surface (term proportional to k_{-}^{σ}) is considered when the electron flux is directed towards the dielectric surface, i.e., $\boldsymbol{J}^{-} \cdot \hat{\boldsymbol{S}} > 0$, and the secondary electron detachment (term proportional to n^{+}) is considered when $\boldsymbol{J}^{+} \cdot \hat{\boldsymbol{S}} > 0$.

The surface contribution to the residual of the electron temperature continuity equation, $R_{\alpha}^{T,A}$, given by equation (3.24), becomes:

$$R_{\alpha}^{T,A} = -\mathcal{J}_{\Sigma_A} J_o \sum_{\substack{\delta,\eta,\kappa,\lambda=1 \\ (\delta,\kappa,\lambda \text{ on } \Sigma_A)}}^{N_b} n_{\delta}^{-} T_{\kappa}^{-} \phi_{\eta} \sum_{i,j=1}^{n} \hat{S}_i c_{ij} D_{\eta\lambda}^{j} V_{\delta'\kappa'\lambda'\alpha'}^{(n-1)}. \tag{3.71}$$

The residuals of the equations of motion for the electron and ion surface charge densities, $R_{\alpha}^{\sigma^-}$ and $R_{\alpha}^{\sigma^+}$ respectively, are also written using the universal matrices after projecting the dependent variables onto the polynomial basis:

$$\begin{aligned} R_{\alpha}^{\sigma^-} \;=\; & \mathcal{J}_{\Sigma_D} \Gamma \sum_{\delta}^{\text{on } \Sigma_D} \frac{\partial \sigma_{\delta}^{-}}{\partial \tau} T_{\delta'\alpha'}^{(n-1)} - \mathcal{J}_{\Sigma_D} k_{-}^{\sigma} \sum_{\delta}^{\text{on } \Sigma_D} n_{\delta}^{-} T_{\delta'\alpha'}^{(n-1)} - \\ & \mathcal{J}_{\Sigma_D} \gamma^{\sigma} M^{+} \beta^{-1} \sum_{\substack{\delta,\eta,\kappa=1 \\ (\delta,\kappa \text{ on } \Sigma_D)}}^{N_b} n_{\delta}^{+} \phi_{\eta} \sum_{i,j=1}^{n} \hat{S}_i c_{ij} D_{\eta\kappa}^{j} Q_{\delta'\kappa'\alpha'}^{(n-1)} + \\ & \mathcal{J}_{\Sigma_D} k_{R}^{\sigma} \sum_{\delta,\eta}^{\text{on } \Sigma_D} \sigma_{\delta}^{-} \sigma_{\eta}^{+} Q_{\delta'\eta'\alpha'}^{(n-1)}. \end{aligned} \tag{3.72}$$

Similarly the integral $R_{\alpha}^{\sigma^+}$, equation (3.26), becomes:

$$\begin{aligned} R_{\alpha}^{\sigma^+} \;=\; & \mathcal{J}_{\Sigma_D} \Gamma \beta \sum_{\delta}^{\text{on } \Sigma_D} \frac{\partial \sigma_{\delta}^{+}}{\partial \tau} T_{\delta'\alpha'}^{(n-1)} + \\ & \mathcal{J}_{\Sigma_D} M^{+} \sum_{\substack{\delta,\eta,\kappa=1 \\ (\delta,\kappa \text{ on } \Sigma_D)}}^{N_b} n_{\delta}^{+} \phi_{\eta} \sum_{i,j=1}^{n} \hat{S}_i c_{ij} D_{\eta\kappa}^{j} Q_{\delta'\kappa'\alpha'}^{(n-1)} + \\ & \mathcal{J}_{\Sigma_D} k_{R}^{\sigma} \beta \sum_{\delta,\eta}^{\text{on } \Sigma_D} \sigma_{\delta}^{-} \sigma_{\eta}^{+} Q_{\delta'\eta'\alpha'}^{(n-1)}. \end{aligned} \tag{3.73}$$

3.4 Time domain solution

A straightforward use of the universal matrices developed in section 3.2 to obtain a finite element formulation in time and in geometric space, as developed by Argyris and Schapf [93], was attempted without success. The stiffness of the two-fluid model equations is the cause of the failure, as is discussed in more detail in section 4.2.1. The stiffness of the equations is mainly due to the significantly different time scales of the ion and electron dynamics. An effective approach to avoid instability is to use independent basis functions in time and in geometric space for the interpolation of nodal values within an element:

$$\phi(\boldsymbol{x},\tau) = \sum_{i=1}^{N_p} \sum_{k=1}^{N_p^\tau} W_i(\boldsymbol{x}) W_k(\tau) \phi_{i;k} \tag{3.74}$$

where the polynomial basis function W_i of order N_p in geometric space and of order N_p^τ in time are those defined in section 3.2. In this formulation the geometric space and time domain, called space-time domain, is meshed using rectangular elements as shown in Figure 3.5. The Galerkin method can be used with $W_i(\boldsymbol{x})W_k(\tau)$ as weight functions. This method was used by Yousfi, Poinsignon, and Hamani [94] for linear interpolation in time and in geometric space. Resolving the model's equations in the time domain can be treated as a boundary value problem due to the periodicity of the forcing functions. However, in the present work, the restrictions on the time discretization are such that one cannot, for practical purposes, mesh the whole space-time domain at once. Furthermore, the charge accumulation process on the dielectric barrier breaks the periodicity in the dependent variable.

We adopt a scheme that integrates the solution in time from an initial condition. The scheme is obtained from a space-time Galerkin formulation and is based upon the work of Gardner, Gardner, and Zaki [95] for the solution of a simplified Fokker-Plank equation.

We use a linear interpolation in time and write the interpolation of the dependent variable ϕ, within a space-time element, as:

$$\phi(\boldsymbol{x},\tau) = \sum_{i=1}^{N_p} W_i(\boldsymbol{x}) \left[\phi_{i;k} + \tau\left(\phi_{i;k+1} - \phi_{i;k}\right)\right] \tag{3.75}$$

where $\phi_{i;k}$ is the nodal value of ϕ for node $\boldsymbol{x} = \boldsymbol{x}_i$ at the time step k and $\phi_{i;k+1} - \phi_{i;k}$ is the accrued increment over a time step. Since the nodal values $\phi_{i;k}$, $i = 1$ to N_p, are determined by the previous time step, the unknowns are

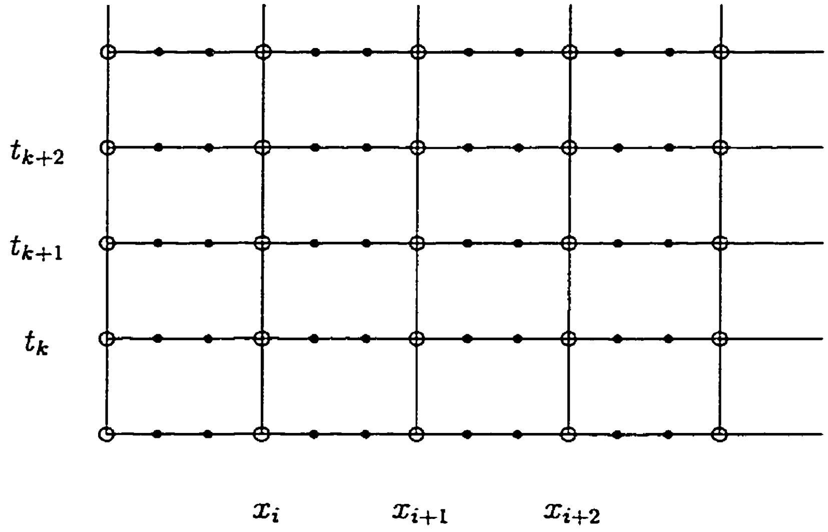

Figure 3.5: Space-time discretization, spatially one-dimensional case.

the nodal values $\phi_{i;k+1}$, $i = 1$ to N_p. The space-time Galerkin method is used to obtain an approximate solution with the N_p weight functions $W_i(\boldsymbol{x})$.

The computer memory required for this scheme corresponds to the resource needed for the geometric space problem only. This permits mesh refinement in the time domain without sacrificing mesh refinement in geometric space due to memory restrictions. Furthermore the processing time grows linearly with the number of time steps. This is significant since the number of time steps can be larger than the number of discretization points in geometric space by an order of magnitude. Increasing the dimension in the geometric space is straightforward when using the universal matrices. Figure 3.6 shows a typical mesh for the case of two spatial dimensions using this scheme.

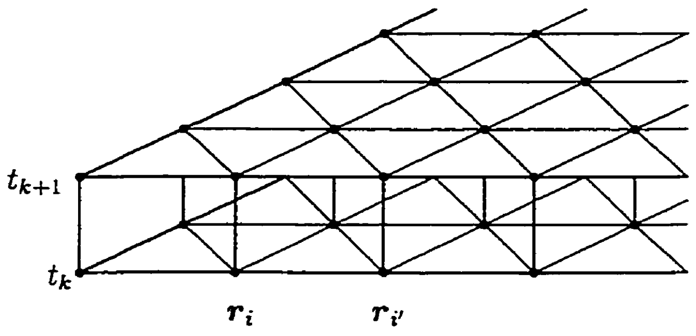

Figure 3.6: Space-time discretization for spatially two-dimensional case.

3.4.1 Validation of the method

The method was tested using the one-dimensional inhomogeneous heat equation:

$$\frac{\partial T}{\partial \tau} - c^2 \frac{\partial^2 T}{\partial^2 x} = sin(\pi x) \tag{3.76}$$

in the finite interval $0 < x < 1$, $\tau > 0$. We assumed a homogeneous initial condition $T(x,0) = 0$ and the boundary conditions $T(0,\tau) = T(1,\tau) = 0$.

The space-time Galerkin finite element method was used to obtain an approximate numerical solution to equation (3.76). The weighted residual of the equation, omitting surface terms where the solution is constrained to be zero, is:

$$R_\alpha = \int_{\tau=0}^{1} \int_{x=0}^{1} \left[\frac{\partial T}{\partial \tau} W_\alpha + c^2 \frac{\partial T}{\partial x} \frac{\partial W_\alpha}{\partial x} - \sin(\pi x) W_\alpha \right] dx d\tau. \tag{3.77}$$

Projecting the functions $T(x,\tau)$ and $\sin(\pi x)$ onto the polynomial basis functions, as in equation (3.75), we get after integration:

$$\begin{aligned} R_\alpha = {} & \sum_{\beta=1}^{N_b} \left(T_{\beta;k+1} - T_{\beta;k}\right) T_{\alpha\beta} + \\ & \frac{1}{2} \Delta\tau \sum_{\beta,\gamma,\sigma=1}^{N_b} \left(T_{\beta;k+1} + T_{\beta;k}\right) D^0_{\beta\gamma} D^0_{\alpha\sigma} T_{\gamma\sigma} - \Delta\tau \sum_{\beta=1}^{N_b} \sin(\pi x_\beta) T_{\alpha\beta} \end{aligned} \tag{3.78}$$

where $\Delta\tau$ is the time step and $T_{\alpha;k}$ is the nodal value of the dependent variable u at node $x = x_\alpha$ at time $\tau = \tau_k$. An analytical solution to equation (3.76) can be obtained, see the textbook of Zauderer [96] p. 206. By applying Duhamel's principle to the solution of the homogeneous heat equation, we get:

$$T(x,\tau) = \frac{1}{\pi}\left(1 - e^{-\pi^2\tau}\right)\sin(\pi x). \tag{3.79}$$

The numerical solution obtained by minimization of the residual, equation (3.78), is identical to the analytical solution within numerical roundoff error.

3.4.2 Stability and convergence criteria

An important aspect of the discretization of the differential operator is to assess the stability of the scheme. Gardner, Gardner, and Zaki [95] performed a stability analysis based on the Von Neumann theory. The discretization of the time differentiation operator is a fully implicit backward difference which is unconditionally stable.

Another important aspect is the condition required for the approximate solution obtained from the numerical scheme to converge to the exact solution of the differential equation as the mesh becomes increasingly refined. The electrons, being much more mobile than the ions, limit the size of the time step. The time step must be small enough to resolve the transit of the fast electrons, present in the cathode sheath, across the discharge gap:

$$\Delta t < d/u_e \tag{3.80}$$

where u_e is the electron fluid mean velocity: $u_e = |\boldsymbol{J}_e|/n_e$, and d is the discharge gap. The criterion can be written using dimensionless ratios and variables:

$$\Delta\tau < \Gamma n^- \left|\boldsymbol{J}^-\right|^{-1}. \tag{3.81}$$

Typically, a good criterion is to take the time step to be 1/10 of the smallest value of the right-hand-side of the above equation, where n^- and $\boldsymbol{J}^-$ are taken from a DC converged solution.

3.4.3 Space-time integration of the residuals

The residuals integrated in geometric space, given in section 3.3, now need to be integrated in time following the example given for the validation case in section 3.4.1.

The integration is carried out analytically using a linear interpolation in time; the dependent variables are projected as shown in equation (3.75). The resulting expressions for the residuals are too cumbersome to be given in detail. Instead, we will give typical integrals involving functions dependent on time, with and without differentiation with respect to time. These integrals are implemented as functions in the computer program.

The time step, $\Delta\tau$, is taken to be constant. The integrations of one, the product of two and three, time-dependent functions are:

$$\begin{aligned}
\int_{\tau=0}^{1} F(\tau)\,d\tau &= \frac{1}{2}\Delta\tau\,(F_{k+1}+F_k)\,, \\
\int_{\tau=0}^{1} F(\tau)G(\tau)\,d\tau &= \frac{1}{3}\Delta\tau\left\{F_{k+1}G_{k+1}+\frac{1}{2}\left(F_{k+1}G_k+F_kG_{k+1}\right)+F_kG_k\right\}, \\
\int_{\tau=0}^{1} F(\tau)G(\tau)H(\tau)\,d\tau &= \frac{1}{4}\Delta\tau\left\{F_{k+1}G_{k+1}H_{k+1}+\right. \\
&\quad \frac{1}{3}\Big(F_{k+1}G_{k+1}H_k+F_{k+1}G_kH_{k+1}+F_kG_{k+1}H_{k+1}+ \\
&\quad F_kG_{k+1}H_{k+1}+F_kG_{k+1}H_k+F_kG_kH_{k+1}\Big)+ \\
&\quad \left.F_kG_kH_k\right\}, \qquad (3.82)
\end{aligned}$$

where $F_k = F(0)$ and $F_{k+1} = F(1)$ represent the function F at the beginning and at the end of the k^{th} space-time element along the time axis. The corresponding integrals involving differentiation with respect to time are:

$$\begin{aligned}
\int_{\tau=0}^{1} \frac{\partial F(\tau)}{\partial\tau}\,d\tau &= (F_{k+1}-F_k)\,, \\
\int_{\tau=0}^{1} \frac{\partial F(\tau)}{\partial\tau}G(\tau)\,d\tau &= \frac{1}{2}\left(F_{k+1}-F_k\right)\left(G_{k+1}+G_k\right), \text{ and} \\
\int_{\tau=0}^{1} \frac{\partial F(\tau)}{\partial\tau}G(\tau)H(\tau)\,d\tau &= \frac{1}{3}\left(F_{k+1}-F_k\right) \qquad (3.83) \\
&\quad \left\{G_{k+1}H_{k+1}+\frac{1}{2}\left(G_{k+1}H_k+G_kH_{k+1}\right)+G_kH_k\right\}.
\end{aligned}$$

3.4.4 Newton's method for nonlinear equations

The residuals of the equations of the model, after discretization of the operators and projection of the dependent variables onto the polynomial basis functions, become a set of nonlinear algebraic equations which may be reduced to a set of linear algebraic equations by the use of the Newton's iterative method. The linearized equations can then be solved by the direct LU decomposition method. This procedure is fairly standard for nonlinear problems and is discussed in many textbooks, see for example the textbook of Reddy and Gartling [89]. To improve the efficiency of the LU decomposition, the nodes are numbered using the reverse Cuthill-McKee ordering algorithm for profiled matrix storage, developed by Liu and Sherman [97]. We used a LU decomposition for a profiled matrix without pivoting. The algorithm was implemented from the pseudo-algorithm given in Golub and Van Loan, §3.2.9, [98] for the full matrix.

The stiffness of the equations of the model is primarily due to two factors:

1. The large difference between the time-scales characterizing the electron and ion dynamics.
2. The strong nonlinearities present in the inelastic collision terms.

As a consequence, first-order linearization methods, such as the Picard method, generally exhibit a low rate of convergence. The advantage of Newton's method, being a second-order scheme, is its fast rate of convergence compared to first-order methods. However the radius of convergence is smaller for second-order methods than for first-order methods. Furthermore, as the stiffness of the equations increases, the radius of convergence decreases.

The most tedious part of this work was to obtain the first converged solution of the model for the DC case (constant applied potential in time). The time-dependent solution was obtained by marching forward in time to a converged DC solution.

To obtain the solution for the DC case it was necessary to relax the Newton's method by retaining only a fraction of the suggested improvement to the solution obtained at each iteration. In some cases it was necessary to retain only 1/1000 of the correction to the solution and perform over two thousand iterations before obtaining the full correction to the solution. Once inside the radius of convergence, the residuals of the equations can be reduced by ten orders of magnitude in about four to five full iterations.

In the next chapter, numerical solution of the two-fluid model equations using the Galerkin method is presented. The weighted residuals are given by equations (3.62), (3.64), (3.65), and (3.66) for Poisson's equation, the electron and ion density continuity equations, and the electron temperature continuity equation. The surface terms of the weighted residuals, where the boundary conditions are used, are given by the equations (3.67) to (3.73). The equations are integrated in time to obtain the solution for time-varying applied voltages using an implicit scheme. The integration is carried out analytically using linear interpolation as described in section 3.4.3.

Chapter 4

Results

Low pressure gas discharges, typically below 5 Torr, are widely used in thin film deposition and surface etching. So far, most of the continuum plasma models have focused on modeling low pressure radio-frequency (RF) glow discharges, due to the large application market in the manufacturing of microelectronics devices and integrated circuits, and the various film deposition technologies such as sputtering and plasma-enhanced chemical vapor deposition.

A landmark publication on low pressure continuum plasma models for DC and RF discharge is the paper by Graves and Jensen [64]. To our knowledge, it is the first model that self-consistently computes the electric potential distribution, electron and ion number densities, and electron temperature distribution from a continuum model based on a boundary value problem in a bounded region. Their formulation, like the one developed in this thesis, is based on the formulation of Chung [54] for the study of Langmuir probe characteristics. Wilcoxson and Manousiouthakis [67] reviewed the formulation of Graves and Jensen and reproduced a number of their results.

In section 4.1, the results of Wardlaw and Cohen [52] for the analysis of the photoionization chamber are reproduced. The analysis of Wardlaw and Cohen, being a simplified version of our model, can be reproduced while the simulation results presented by Graves and Jensen [64] cannot be reproduced due to the following shortcomings:

1. No numerical value, or explicit relation in terms of known parameters, is given for the electron thermal conductivity.

2. In [64], Table III presents the values of the dimensionless ratios used for obtaining the Graves and Jensen results. These ratios, defined in Table II of [64], can be calculated from the scaling parameters and gas parameters used in the simulations given in Table IV of [64]. The characteristic electric field strength, named Q in this thesis and Γ in [64], is calculated to be 195.35 based on the physical parameters of Table IV, while their numerical value is 488.9 in Table III. This is not consistent with the value of the other dimensionless ratios. This means that one cannot change the value of a physical parameter to match this value without causing other dimensionless ratios to disagree.

3. The equation for the non-dimensional electron temperature, equation (17) in [64], is missing a term proportional to the time derivative of the electron density. Using the Graves and Jensen notation, the missing term is:

$$-\frac{2}{5}T\theta_e\frac{\dot{\rho}_e}{\rho_e} \tag{4.1}$$

where T is the characteristic electron diffusion time (named Γ in this thesis), θ_e and ρ_e are the dimensionless electron temperature and number density respectively. Note that the first term in equation (17) of [64] should be written using the dimensionless electron temperature, θ_e, rather than using the (dimensional) electron enthalpy h_e. Furthermore, as seen by the missing term above, their electron temperature equation is divided by the electron density ρ_e. This is correct provided that $\rho_e \neq 0$. Their boundary condition for ρ_e at the anode is precisely $\rho_e = 0$. Therefore their dimensionless electron temperature equation is mathematically incorrect and yields to an ill-posed problem. Therefore, one must assume that this equation was not the one used in their computer program.

Simulation results equivalent to the results of Graves and Jensen [64], Graves [66], and Wilcoxson and Manousiouthakis [67] for a discharge geometry without a dielectric barrier are reported in section 4.2. The identification of the physically correct boundary conditions for the electron temperature and number density at the anode is an important contribution to the research community. As a direct result, the electron temperature near the anode no longer exhibits the non-physical behavior observed when the electron temperature is assumed to be known at the anode.

In section 4.3 simulation results for discharge with a dielectric barrier covering the cathode are presented. No model in the literature has provided a self-consistent coupling of the dielectric barrier and the plasma, as achieved in this thesis. To understand the impact of the presence of the dielectric barrier, the discharge conditions were kept identical to those of section 4.2. The results illustrate the regulating mechanism of the barrier on the discharge characteristics.

The gas discharge conditions used in the simulations presented in this chapter are given in Table 4.1. The only inelastic process used is ionization by electron impact on a neutral molecule. The parameters for the ionization rate were taken from Park and Economou [72] for low pressure gas discharge in chlorine. The parameters were obtained to equate the analytical approximation to the ionization rate given by equation (2.35) with the rate constant calculated by solving the Boltzmann transport equation. The equation was solved for different values of the reduced field, E/N, and the corresponding electron distribution function was found. The rate constant was then calculated using equation (2.32). Computer code for solving the Boltzmann transport equation is readily available at the Computer Physics Communications Program Library at Queen's University of Belfast. Morgan and Penetrante [20] developed a so-called Boltzmann solver and made it available to the CPC Program Library.

D_e	1.81×10^6	$\mathrm{cm^2\,s^{-1}}$
μ_e	3.62×10^5	$\mathrm{cm^2\,V^{-1}\,s^{-1}}$
D_{ion}	400	$\mathrm{cm^2\,s^{-1}}$
μ_{ion}	2000	$\mathrm{cm^2\,V^{-1}\,s^{-1}}$
k_{z0}	8×10^{-15}	$\mathrm{cm^3\,s^{-1}}$
T_L	1.35	eV
k_z	3.095×10^{-8}	$\mathrm{cm^3\,s^{-1}}$
$\tilde{E}_1$	-3.3403	eV
$\tilde{E}_2$	-42.105	$\mathrm{eV^2}$
$\tilde{E}_3$	81.313	$\mathrm{eV^3}$
$\tilde{E}_4$	75.338	$\mathrm{eV^4}$
$\tilde{H}_z$	11.5	eV
k_r	10^7 or equation (2.49)	$\mathrm{cm\,s^{-1}}$
k_e^σ	10^7	$\mathrm{cm\,s^{-1}}$
k_r^σ	100	$\mathrm{cm^2\,s^{-1}}$
γ	5% at electrodes, 1% at dielectric barrier	
ϵ_r	5 and 50	
$\Phi^A(t)$	0	V
Φ^C	-300 and -400 for DC simulation	V
$\Phi^C(t)$	-200 to -600, pulse and harmonic shape	V

Table 4.1: Gas discharge parameters used to obtained simulation results.

The scaling parameters used are given in Table 4.2. The gas parameters are defined in Table 2.1, while the scaling parameters are defined in Table 2.3.

4.1 Validation of the formulation

The accuracy of the implementation of the model was validated by reproducing the results of Wardlaw and Cohen [52] for the continuum analysis of the photoionization chamber.

The ionization mechanism that sustains the plasma is ionization by a light source which photoionizes the confined gas. The analysis requires computing the electron and positive ion density distributions which make up the plasma and the electric field distribution between the electrodes. The formulation of the

N	1.78×10^{16}	cm^{-3}
N_o	4×10^{9}	cm^{-3}
d	3	cm
V_o	300	V
ν	10^5 and 10^7	s^{-1}
T_e^{av}	2	eV

Table 4.2: Plasma scaling factors used to obtain simulation results.

equations governing the continuum description of the photoionization chamber, as given by Wardlaw and Cohen [52], is:

$$\begin{aligned} \nabla\cdot(-D_-\nabla N_- + \mu_- N_- \boldsymbol{E}) &= \nu N_n \\ \nabla\cdot(-D_+\nabla N_+ - \mu_+ N_+ \boldsymbol{E}) &= \nu N_n \\ \nabla\cdot\boldsymbol{E} &= -4\pi e\,(N_+ - N_-)\,, \end{aligned} \tag{4.2}$$

where N_- is the electron distribution, D_- and μ_- are the electron diffusion and mobility coefficients respectively. The corresponding quantities for the ions are N_+, D_+, and μ_+. The electric charge is e, while $\boldsymbol{E}$ is the negative of the electric field. The right-hand-side of both continuity equations for electrons and ions represents the rates of charge particle production by photoionization; ν is the ionization rate per unit time and N_n is the neutral particle density (background gas).

In the Wardlaw and Cohen formulation, recombination in the discharge space as well as at the electrodes is neglected due to the low charge particle densities that exist within a photoionization chamber. Also, as with the model presented in this thesis, the electrons and ions are assumed to have independent temperatures, as denoted by Wardlaw and Cohen as T_- and T_+ respectively.

The kinematic coefficients $D_\pm$ and $\mu_\pm$, and the temperatures $T_\pm$, are taken to be constants throughout the chamber. As a consequence, the electrons are in thermal equilibrium with the electric field while the ions are in thermal equilibrium with the background gas. Furthermore $D_\pm$ and $\mu_\pm$ obey Einstein's relation:

$$\frac{D_\pm}{\mu_\pm} = \frac{kT_\pm}{e}. \tag{4.3}$$

To establish the boundary conditions, the electrodes are considered to be perfectly absorbing: $N_- = N_+ = 0$ at the walls. Further, the electric potential across the electrodes is prescribed by:

$$\int_{-L}^{L} \boldsymbol{E} \cdot d\boldsymbol{l} = V \tag{4.4}$$

where V is the potential difference between the anode and the cathode and L is one-half the inter-electrode separation.

When the equations (4.2) are recast using dimensionless variables, following Wardlaw and Cohen's notation, integrating the particle flux equations once yields:

$$\begin{aligned} \frac{dn_-}{d\hat{x}} - \epsilon n_- \hat{E} &= -\alpha\delta\left(\hat{x} - 1 + J_-\right), \\ \frac{dn_+}{d\hat{x}} + n_+ \hat{E} &= -\alpha\delta\left(\hat{x} - 1 + J_+\right), \\ \frac{d\hat{E}}{d\hat{x}} &= n_- - n_+, \end{aligned} \tag{4.5}$$

where J_- and J_+ are integration constants and the dimensionless variables and ratios are:

$$\begin{gathered} \alpha = \frac{\nu N_n}{D_+} \frac{4\pi e^2 L^4}{kT_+}, \; \hat{x} = \frac{x}{L}, \\ n_\pm = \frac{4\pi e^2 L^2}{kT_\pm} N_\pm, \; \hat{E} = \frac{eL}{kT_+} E, \\ \epsilon = \frac{T_+}{T_-}, \; \delta = \frac{D_+}{D_-}, \; \psi = \frac{eV}{kT_+}. \end{gathered} \tag{4.6}$$

The boundary conditions for the dimensionless variables are:

$$n_\pm(\pm 1) = 0, \; \int_{-1}^{1} \hat{E} d\hat{x} = \psi. \tag{4.7}$$

The solution to equations (4.5) together with the associated boundary conditions, is greatly affected by the magnitude of the parameters α, ϵ, δ, and ψ. It is pertinent to examine their possible sizes.

In principle, the electron temperature can be equal to or greater than the ion temperature, in practice it is much greater: $10^{-3} \leq \epsilon \leq 10^{-1}$. Owing to the great difference in the masses of the electron and the ion, δ will be small: $\delta \approx 10^{-4}$. Although the applied voltage ψ can take on any value, for very large voltages collisional ionization will occur and the formulation of equations (4.2) will no longer be valid. The parameter α is related to the photoionization rate and the electrode separation length. For the ambipolar diffusion case, a sufficiently high rate of ionization is required to form a quasi-neutral region at the center of the chamber. In this case α is usually greater than 10^4.

The relations between Wardlaw and Cohen's dimensionless variables, defined by equations (4.6), and the dimensionless variables developed in this thesis, are given by:

$$\begin{gathered}
\alpha = \frac{QM^+}{14N_o} A_z \beta, \\
N_\pm = \frac{QM^+}{4} n^\pm, \ \hat{E} = -\frac{1}{2} M^+ E, \\
\epsilon = \frac{Mm}{M^+}, \ \delta = \beta^{-1}, \text{ and, } \psi = M^+ \phi^C.
\end{gathered} \tag{4.8}$$

The left-hand-side of the above equations are the dimensionless ratios and variables used by Wardlaw and Cohen while the right-hand-sides are the corresponding quantities used in this thesis. Our dimensionless constitutive equations can be recast in a form similar to equations (4.5) provided that:

$$A_z = \alpha\delta, \ \beta = \delta^{-1}, \ M^- = \epsilon, \ M^+ = 1, \ Q = 1, \text{ and } \phi^C = \psi. \tag{4.9}$$

Three simulations were presented by Wardlaw and Cohen [52] and are reproduced here. Wardlaw and Cohen's results were carefully estimated from enlargements of their graphical plots. Figure 4.1 and Figure 4.2 correspond to results presented by Wardlaw and Cohen in their Figures 7 and 8 respectively. In these cases no potential is applied across the electrodes, and as a consequence, the charged particles diffuse towards the electrodes and the distributions of the particle densities are characterized by a plane of symmetry at the center of the chamber, parallel to the electrodes. In the figures, the normalized densities and the electric field are shown according to our normalization.

Figure 4.3 illustrates the photoionization case when a non-zero potential difference is applied across the electrodes. This corresponds to Figure 9 of Wardlaw and Cohen. The large electric field in the cathode region suppresses the electron density in the vicinity due to the drift component of the particle flux. As shown in the next section, the electron temperature is no longer in thermal equilibrium with the electric field.

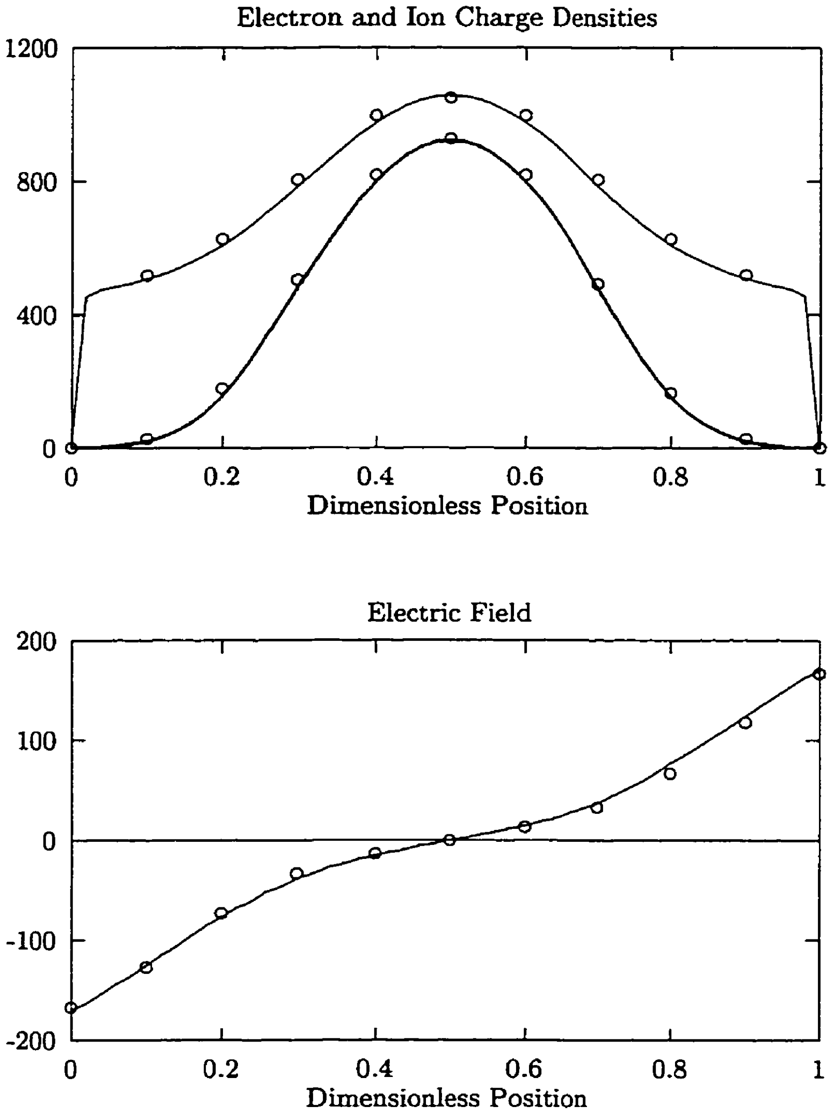

Figure 4.1: Charge densities (top) and electric field (bottom). Dimensionless electron (solid bold line) and ion (solid line) densities. Dimensionless electric field (solid line). Data points are estimates from Wardlaw and Cohen [52], Figure 7. Solid lines are simulation results. $\alpha = 10^4, \epsilon = 0.2, \psi = 0$, and $\delta = 4.48 \times 10^{-4}$.

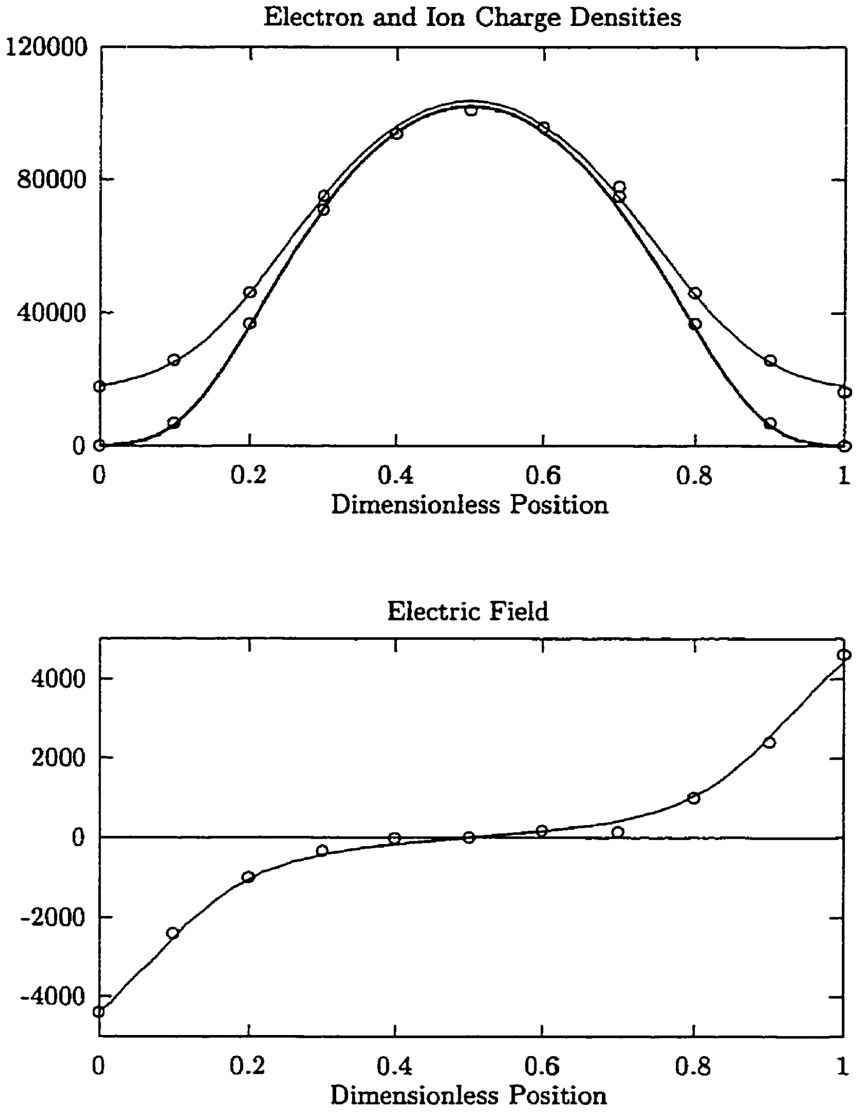

Figure 4.2: Charge densities (top) and electric field (bottom). Dimensionless electron (solid bold line) and ion (solid line) densities. Dimensionless electric field (solid line). Data points are estimates from Wardlaw and Cohen [52], Figure 8. Solid lines are simulation results. $\alpha = 10^7, \epsilon = 0.01, \psi = 0$, and $\delta = 10^{-4}$.

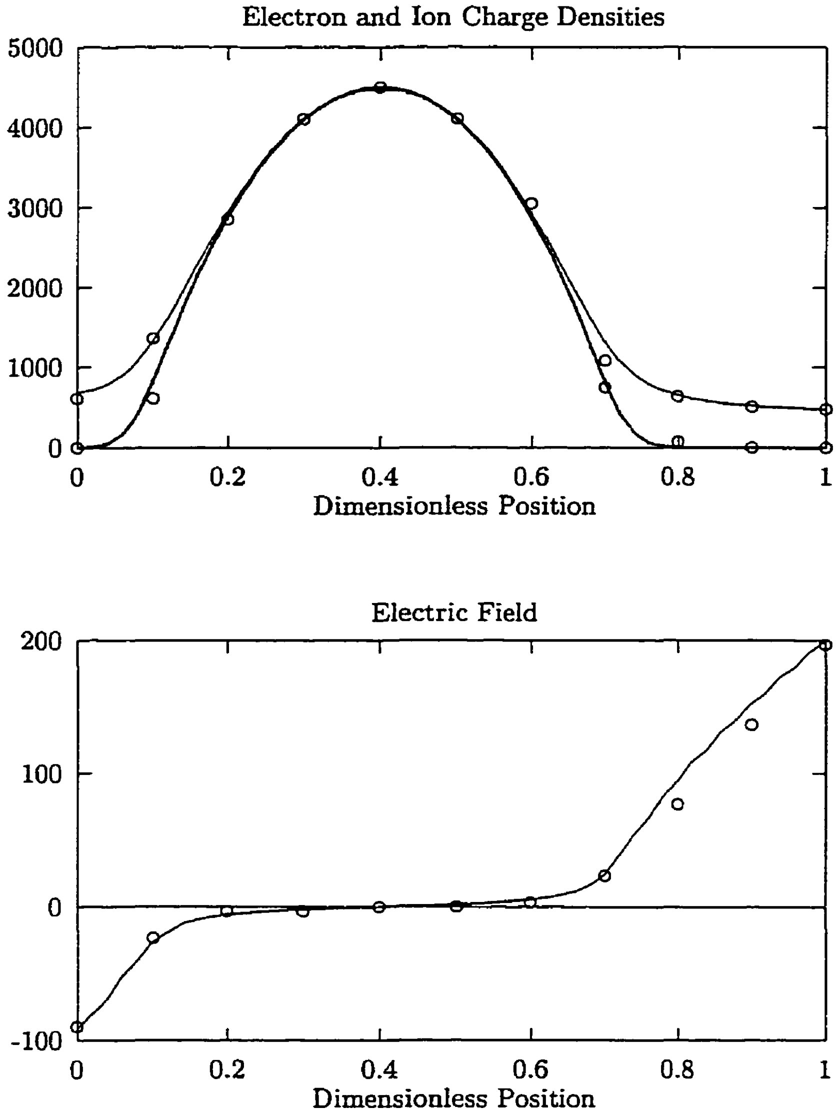

Figure 4.3: Charge densities (top) and electric field (bottom). Dimensionless electron (solid bold line) and ion (solid line) densities. Dimensionless electric field (solid line). Data points are estimates from Wardlaw and Cohen [52], Figure 9. Solid lines are simulation results. $\alpha = 10^4, \epsilon = 1, \psi = -30.2$, and $\delta = 10^{-3}$.

4.2 Geometry without dielectric barrier

Simulation results for the geometry without a dielectric barrier are presented in this section. Discharge for a constant applied voltage across the electrodes, the so called DC case, is presented in section 4.2.1. The boundary conditions for the electron number density and temperature are those used in most publications, i.e., assuming a pair of known electron temperatures at the electrodes and a known electron mean velocity at the anode. In section 4.2.2, a closer look at the electron temperature reveals the physically incorrect behavior near the anode. Simulation with the new boundary conditions developed in section 2.2.3 results in the expected physical behavior. The time-dependent simulations with applied voltages of the pulse and time-harmonic waveforms are presented in section 4.2.3. In these simulations, only the physically correct boundary conditions are used for n_e and T_e.

4.2.1 DC solution

A simulation of the DC case without dielectric material in the discharge space is presented in this section. The voltage applied at the cathode is $-300\,\mathrm{V}$ while the anode is grounded. The electron temperature is fixed to be $0.2\,\mathrm{eV}$ at the anode and $1.0\,\mathrm{eV}$ at the cathode. The electron recombination rate at anode is assumed to be $k_r = 10^7\,\mathrm{cm/s}$. These parameters are typical for a low pressure discharge of argon-like or chlorine-like gases.

The electron thermal conductivity coefficient is assumed to be independent of the electron temperature: $\tilde{K}_e = 5kD_e n_e/2$. It will be shown in the next section that if the electron thermal conductivity coefficient depends on temperature (as it should), then the results will be incompatible with the boundary condition for the electron temperature given by Graves [66], based on the heat flux balance at the cathode.

The results for the electron and ion number densities are given in Figure 4.4. As in all the figures that follow, the abscissa is the dimensionless position between the electrodes (when appropriate the dimensionless position within the period), and the ordinate is the dimensional characteristic of the plasma. The densities exhibit quasi-neutrality in the bulk region, and charge separation occurs in the plasma sheath regions. The densities increase almost linearly from the anode sheath to their maxima located near $x = 0.6$, and then decrease more rapidly approaching the cathode sheath. This is in contrast with the symmetric, or near symmetric, bell shape obtained for the photoionization case.

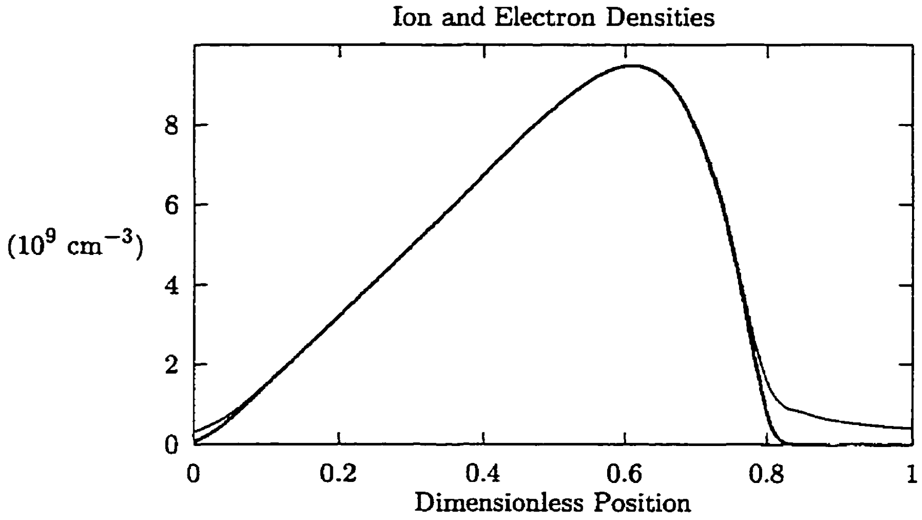

Figure 4.4: Electron (solid bold line) and ion (solid line) densities. Typical solution for DC case.

The corresponding electric potential and electric field are given in Figure 4.5. The electric field in the bulk region is very small which is characteristic of a plasma. Most of the potential drop occurs in the cathode sheath which corresponds a high electric field. Electrons emitted at the cathode by secondary emission due to ion impact are accelerated by this large electric field. These electrons attain a high temperature before entering the plasma region where their temperature then drops as they approach thermal equilibrium with the electron fluid. The electron temperature and ionization rate distribution are shown in Figure 4.6. The ionization by electron impact rate exhibits a broad peak, due to its linear dependence upon the electron density, followed by a high narrow peak due to the rapid increase in electron temperature. The ionization

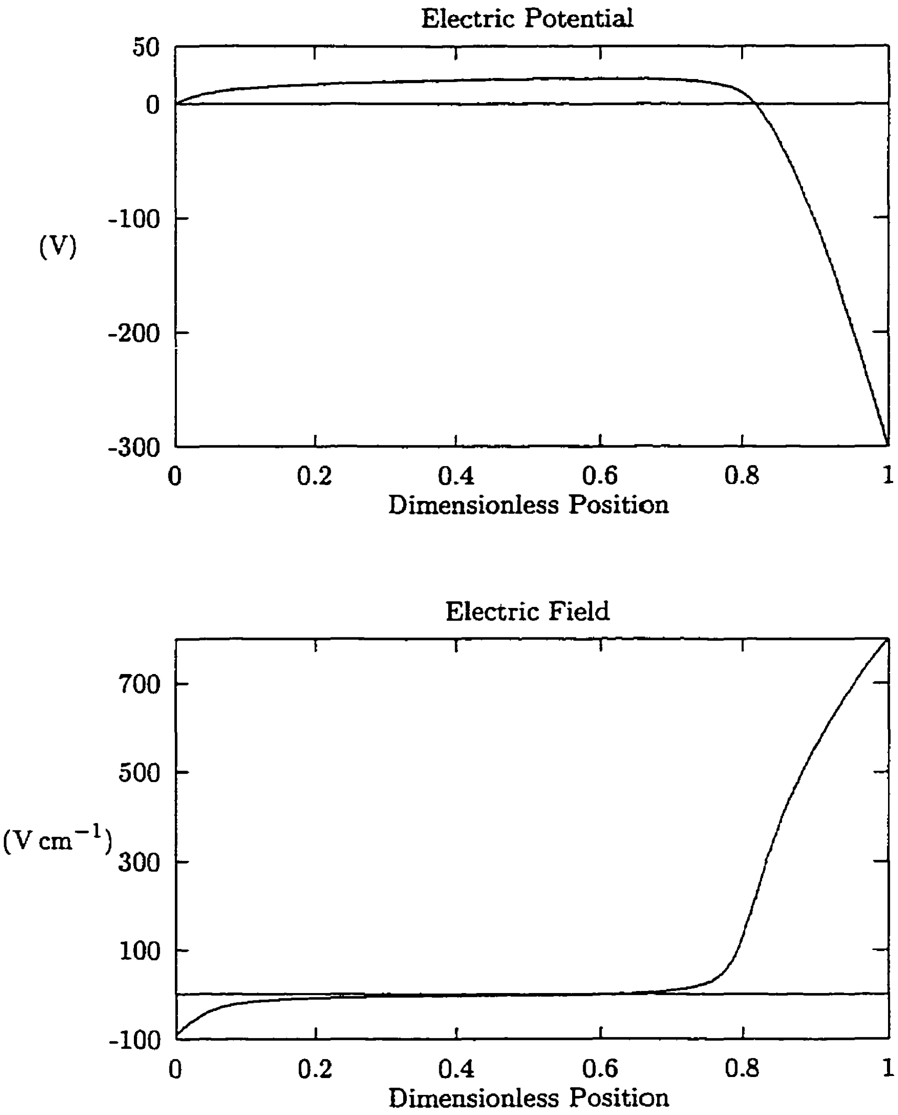

Figure 4.5: Electric potential (top) and electric field (bottom). Typical solution for DC case. For convenience, the zero-value ordinate is plotted in each case.

rate is then suppressed in the cathode sheath due to the small electron density in that region. The ionization rate depends exponentially on the temperature, which makes it very sensitive to temperature variation.

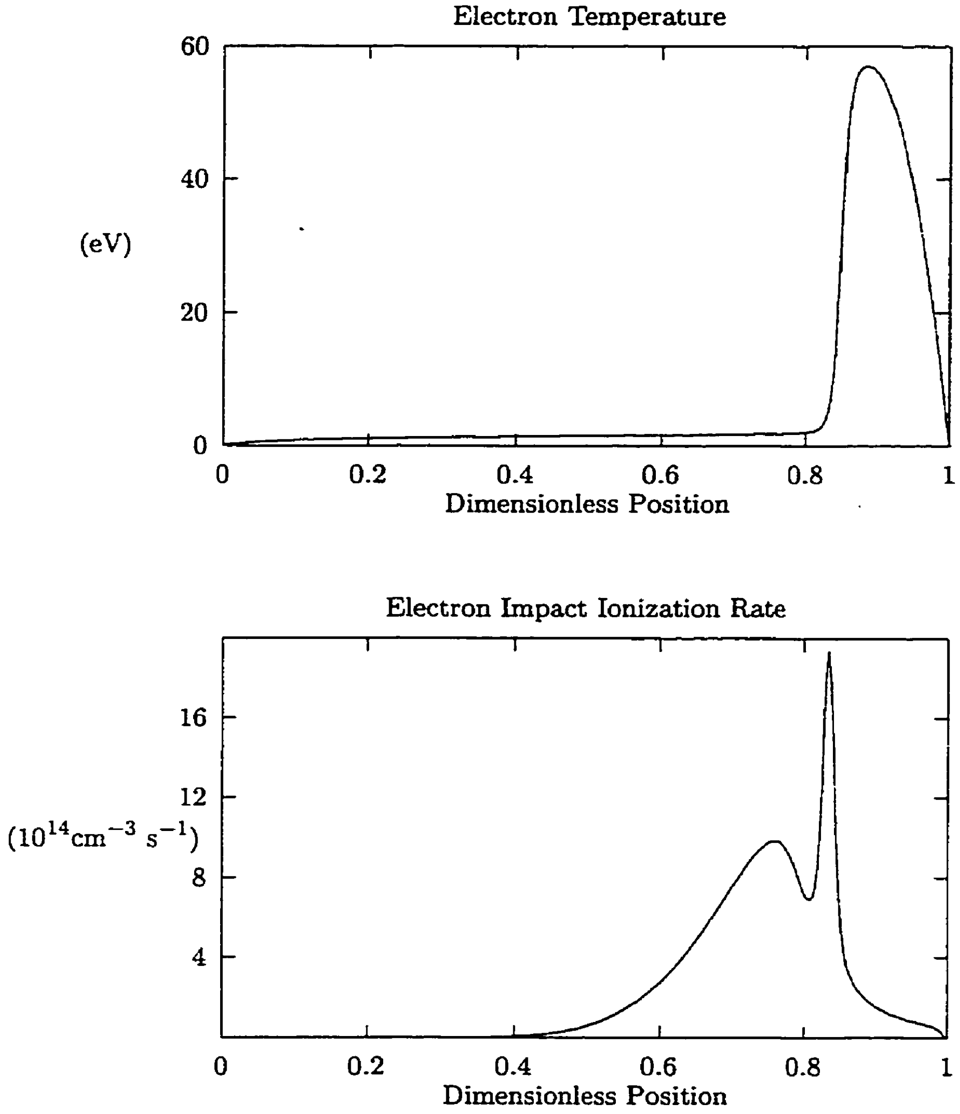

Figure 4.6: Electron temperature and electron impact ionization rate. Typical solution for DC case.

The stiffness of the equations originates in the small region, called the cathode pre-sheath, where the dependent variables experience large variations. In this region, located approximately between 0.7 and 0.85, the electron density decreases by more than 3 orders of magnitude, the electron temperature increases from 2 eV to 35 eV, and the electric field increases from 10 V/cm to 375 V/cm. In the same region the ion density decreases by only one order of magnitude due to the low mobility of the ions. This behavior, observed in the ionization shock wave present at the tip of the electron avalanche in overvolted gaps, was studied by Albright and Tidman [56] with the simplifying assumption that the electron temperature is constant throughout the shock zone. Abbas and Bayle [99] extended this work by studying the variation of the electron temperature over the whole shock zone with the assumption that the electron gas is in local equilibrium with the electric field. The cathode pre-sheath, or shock zone, is characterized by the transition between a region of relatively low electric field, low electron temperature, and high plasma density (bulk space) to a region of relatively high electric field, steep rise in electron temperature, and low plasma density (sheath region).

The dimensionless coefficient β corresponds to the ratio of the electron to the ion diffusion coefficients. In the present simulations it is 10^4. This yields a strong feedback mechanism through the ionization source term of the ion particle continuity equation, right-hand-side of equation (2.67). A small variation in the electron temperature will translate into, due to the exponential dependence, a large variation in the ionization rate. This variation will be amplified by the factor β in the ion continuity equation. The only feedback effect the ions have on the ionization rate is through the Poisson equation. In response to the change in the ionization rate, the correction in the ion density distribution will affect the electric potential, which in turn will adjust the electric force exerted on the electrons. As a consequence, the electron density and temperature will be corrected. This indirect feedback mechanism, in addition to the phase transition in the ionization shock zone, makes the two-fluid model very stiff.

The electron and ion contribution to the total current density is shown in Figure 4.7. The total conduction current is the sum of the electron and ion current densities. The electron current density is the negative of the electron particle flux density, while the ion current density corresponds to the ion particle flux density. This is due to the charge difference between the two species. The ion flux density dominates in the cathode sheath where a small electron flux density exists due to secondary electron emission. The electron flux density dominates throughout the bulk of the plasma, as well as in the anode sheath, due to the large diffusivity and mobility of the electrons.

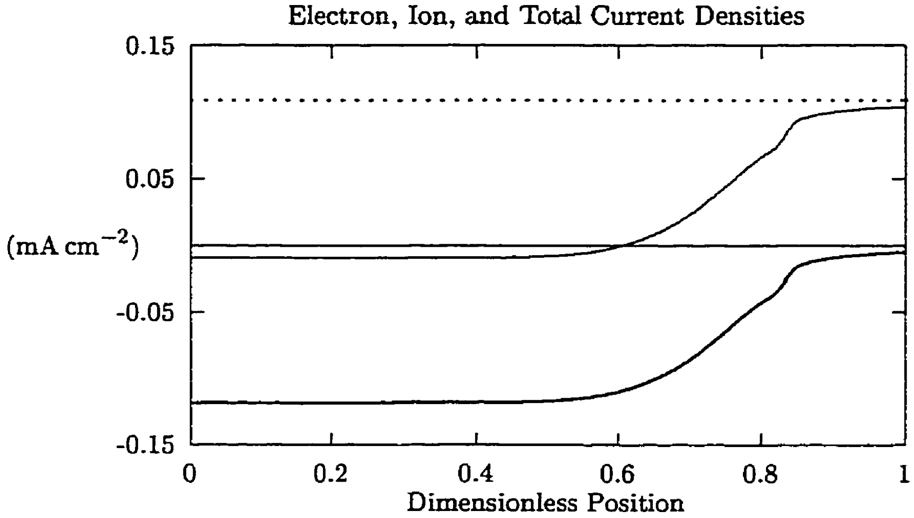

Figure 4.7: Electron (solid bold line) and ion (solid line) flux densities and total conduction current (dotted line). Typical solution for DC case. For convenience, the zero-value ordinate is plotted.

The diffusion and drift components of the electron and ion flux densities are illustrated in Figure 4.8. The electron flux density results from the cancellation of relatively large diffusion and drift terms, particularly in the shock zone. The diffusion of the ions is a negligible contribution due to their flux density. The total current density is conserved, i.e., solenoidal. This is expected since the charge creation mechanism creates an equal number of charges per event.

The electron thermal conduction and electron flux contributions to the heat flux are shown in Figure 4.9. The thermal conduction dominates in the plasma bulk region due to the relatively large electron density. The contribution due to the electron flux (enthalpy flux) dominates in the cathode sheath due to the

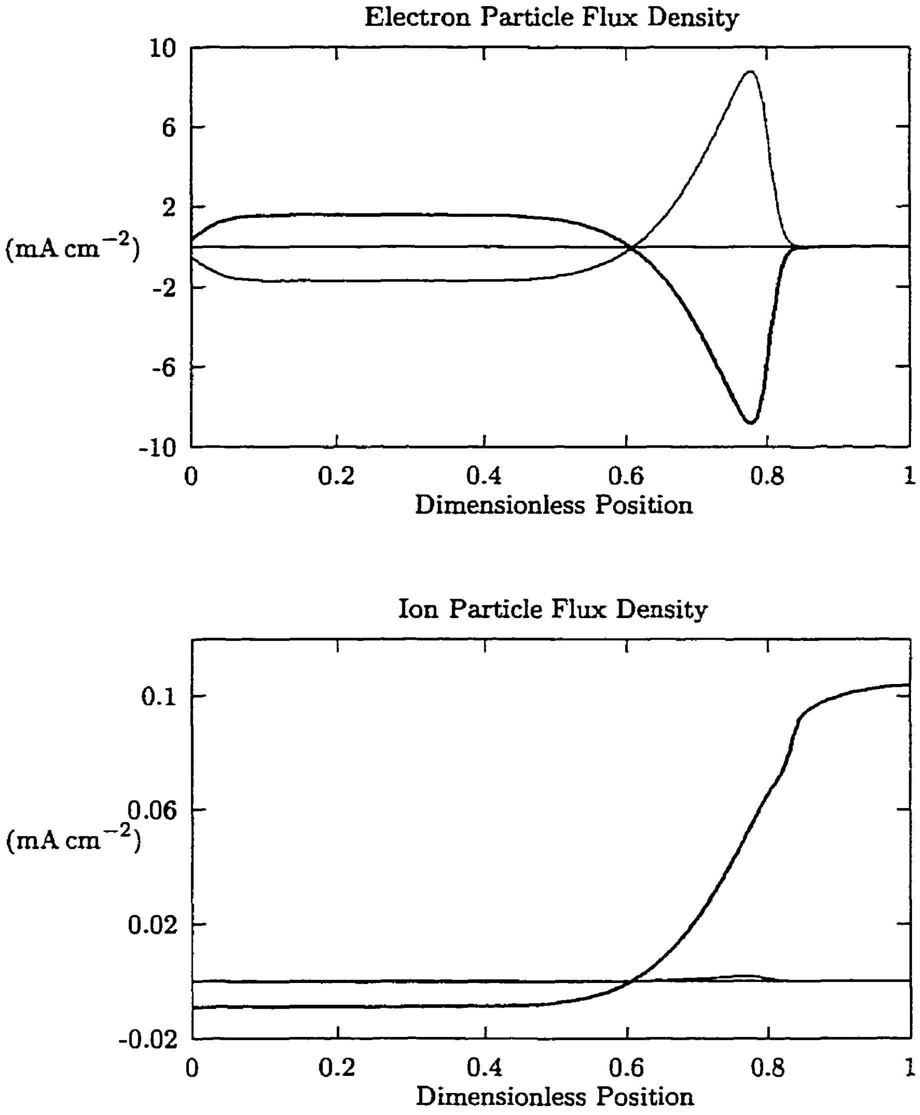

Figure 4.8: Drift (solid bold line) and diffusion (solid line) contributions to electron (top) and ion (bottom) flux densities. Typical solution for DC case. For convenience, the zero-value ordinate is plotted in each case.

high electron temperature and the nonzero electron particle flux caused by the secondary electron emission.

The electron and ion Joule effects are shown in Figure 4.9. Most of the discharge power is used for accelerating the ion gas in the cathode sheath. In the shock zone the electrons drift toward the plasma bulk region while they diffuse against the electric field. The net flux is directed toward the plasma bulk region resulting in a net heating of the electron gas. At the anode the electrons diffuse against the electric field, resulting in a cooling of the electron gas. This will be analyzed further in the next section.

4.2.2 Simulations with new boundary conditions at electrodes

Simulation results based on different boundary conditions for the electron number density and temperature at the anode are compared.

Figure 4.10 shows the electron temperature near the anode for three sets of boundary conditions. The boundary conditions developed in section 2.2.3, which are:

$$\begin{aligned} \boldsymbol{J}_e \cdot \hat{\boldsymbol{S}} &= n_e \sqrt{\frac{3k}{m_e} T_e} \\ \hat{\boldsymbol{S}} \cdot \boldsymbol{\nabla}_r T_e &= -\frac{2e}{5k} \hat{\boldsymbol{S}} \cdot \boldsymbol{E}. \end{aligned}$$

Results obtained with these boundary conditions are referred to as "new boundary conditions" in the figures of this section. Results were obtained with the simpler boundary conditions, widely used in the literature, which assume a known electron temperature and electron velocity at the anode:

$$\begin{aligned} T_e &= T_e^A \\ \boldsymbol{J}_e \cdot \hat{\boldsymbol{S}} &= k_r n_e \end{aligned}$$

Simulation results were obtained for $k_r = 10^7$ cm s^{-1} and $T_e^A = 0.2$ eV, see solid line in Figure 4.10. These are typical values for low pressure discharge. We note that in this case the electron temperature becomes constant at the

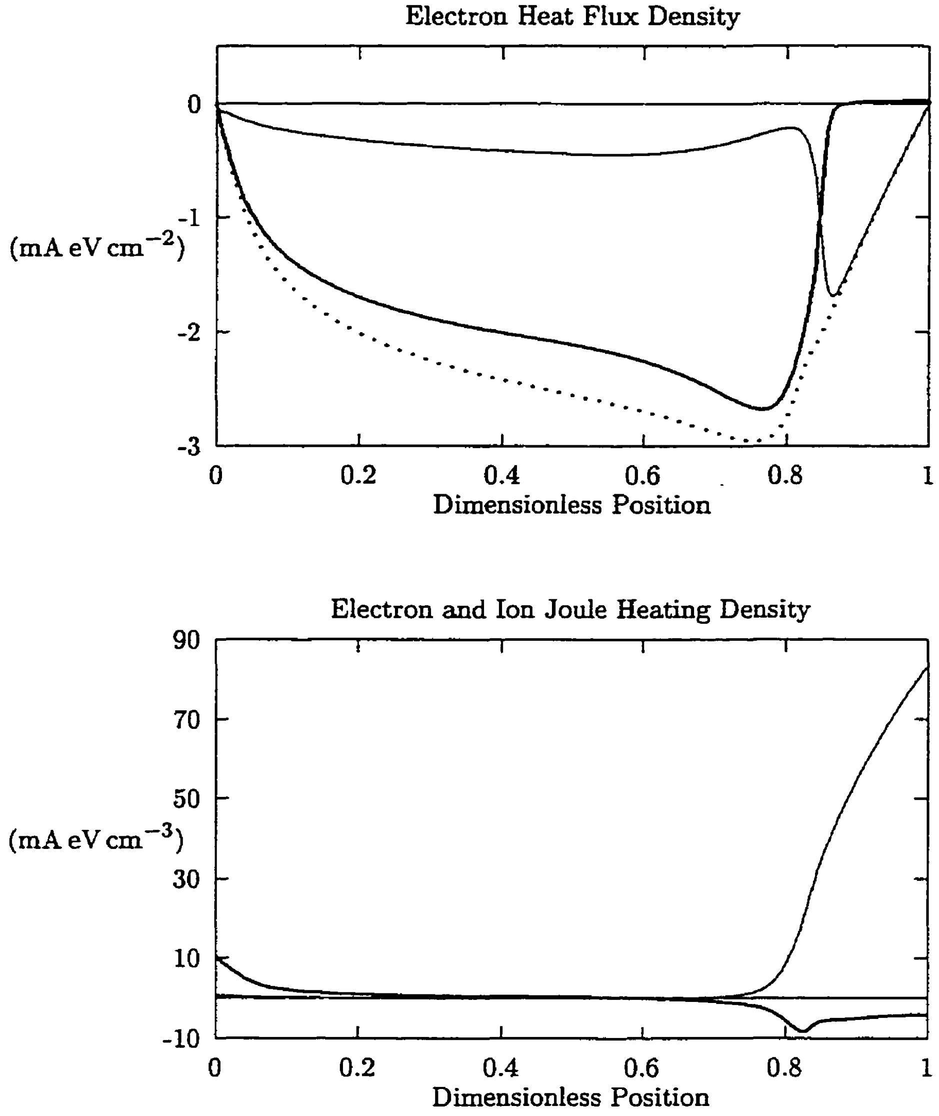

Figure 4.9: Electron thermal conduction (solid bold line) and electron flux (solid line) contributions to the electron heat flux term (dotted line) are shown in the upper plot. Electron (solid bold line) and ion (solid line) Joule heating are shown in the lower plot. Typical solution for DC case. For convenience, the zero-value ordinate is plotted in each case.

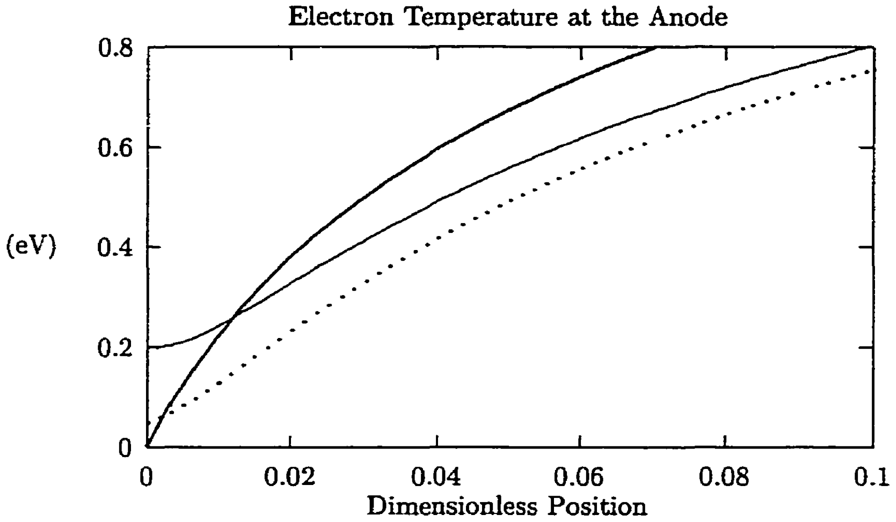

Figure 4.10: Electron temperature at anode, results using new boundary conditions (solid bold line); T_e fixed at 0.2 eV (solid line); and T_e fixed at 0.05 eV (dotted line).

anode, i.e., the electron fluid is not cooled in the small boundary layer as the electrons diffuse toward the anode. This is clearly in contradiction with the electric field obtained near the anode, see solid line of Figure 4.11. The field gradient is at its highest value at the anode and decreases towards the bulk of the plasma. Therefore the electron fluid should experience greater cooling at points closer to the anode. This is precisely the result obtained using the new boundary conditions, see solid bold line of Figure 4.10.

In order to match the assumed electron temperature with the assumed electron velocity at the anode, T_e^A computed as:

$$T_e^A = \frac{m_e}{3k} k_r^2$$

yields $T_e^A \simeq 0.05$ eV for $k_r = 10^7$ cm/s. Surprisingly many authors, such as Park and Economou [72, 65], Graves and Jensen [64], and Wilcoxson and Manousiouthakis [67], do not use a constant T_e^A and k_r that satisfy the above relation. The results obtained with matched T_e^A and k_r are improved, see dotted line of Figure 4.10, however the non-physical behavior remains in a small boundary layer near the anode.

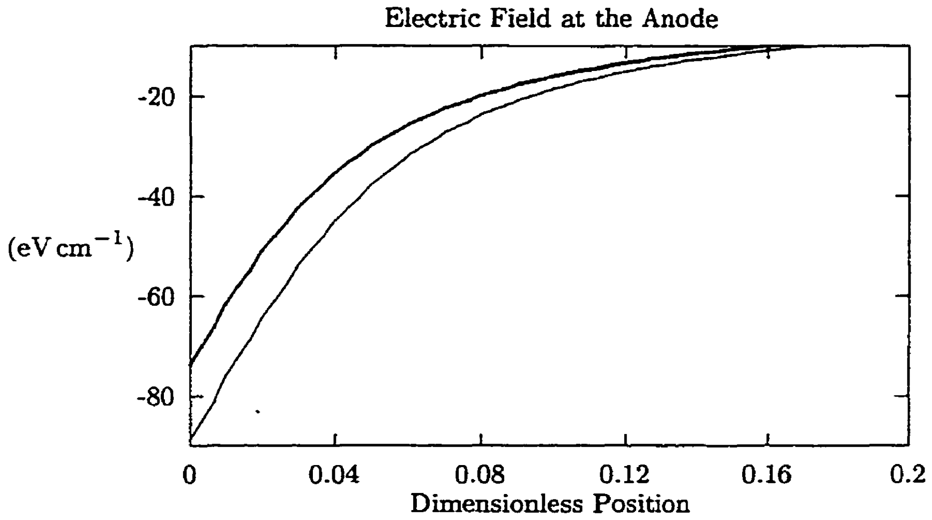

Figure 4.11: Electric Field at anode, results using new boundary conditions (solid bold line); T_e fixed at 0.2 eV (solid line).

It is important to have physically correct boundary conditions due to the strong nonlinearity of the equations of the model. The electric field in the anode sheath is affected by the choice of boundary conditions for the electron fluid as shown in Figure 4.11. This in turn will affect the particle densities distribution and electron temperature distribution throughout the plasma.

The importance of the electron thermal conductivity coefficient, $\bar{K}_e$, and its dependence on the electron temperature, is not studied in the literature. Recalling the expression for $\bar{K}_e$ given by equation (2.29):

$$\bar{K}_e = \frac{5k}{2} D_e n_e \frac{T_e}{T_e^{av}}.$$

Graves and Jensen [64] considered $\bar{K}_e$ to be dependent on both the electron density and temperature, however in a following publication, Graves [66] dropped the temperature dependence by using $T_e{=}T_e^{av}$ in $\bar{K}_e$. This simplification was not justified, however many authors, including Park and Economou [72] and more recently Lymberopoulos and Economou [85], followed this simplification.

Figure 4.12 shows the impact on the electron conductivity term of the heat flux due to the temperature dependence of $\bar{K}_e$. The thermal conductivity in the bulk of the plasma is reduced when $\tilde{K}_e$ is scaled using T_e, indicating a lower temperature in the bulk of the plasma than the average value expected using a Maxwellian distribution function for the electrons. In the cathode region, the electron conductivity becomes relatively important when $\tilde{K}_e$ is scaled with T_e due to the high temperature. As a consequence, the heat flux in the cathode region is dominated by the electron conductivity, leading to a non-negligible heat flux directed toward the anode from the plasma sheath as shown in Figure 4.13.

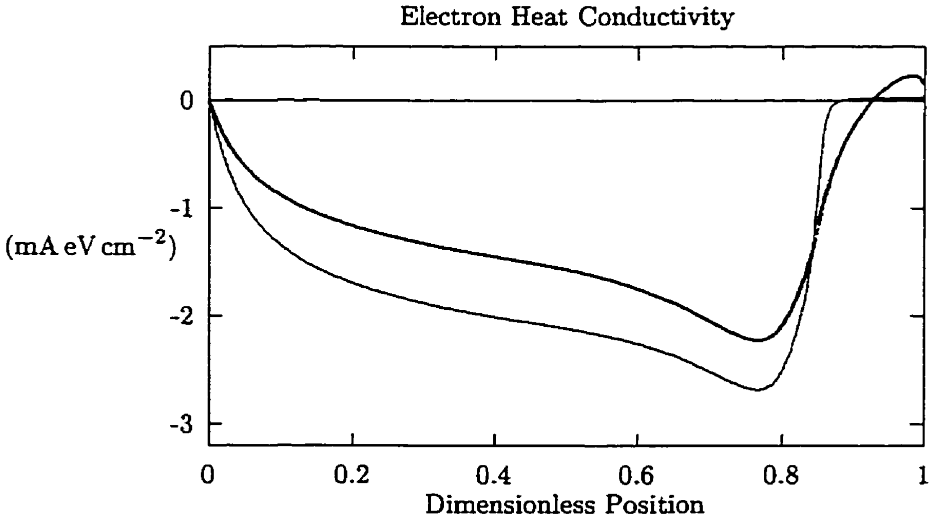

Figure 4.12: Electron conductivity term: results using the electron conductivity $\tilde{K}_e$ dependent on n_e and T_e (solid bold line); and the case where $\tilde{K}_e$ depends on n_e only (solid line). For convenience, the zero-value ordinate is plotted.

This is significant in terms of the boundary condition for the electron temperature since the cathode is an electron emitting electrode. The flux balance boundary condition for the electron temperature, used by Graves [66] and subsequently by Lymberopoulos and Economou [85], given by equation (2.51), reduces to

$$\boldsymbol{q}_e \cdot \hat{\boldsymbol{S}} = -\gamma \boldsymbol{J}_{ion} \cdot \hat{\boldsymbol{S}} \left(\frac{3}{2} k T_e^C\right)$$

for an emitting surface, which implies that the net heat flux at the cathode is due to the secondary electrons emitted at temperature T_e^C by ion impact

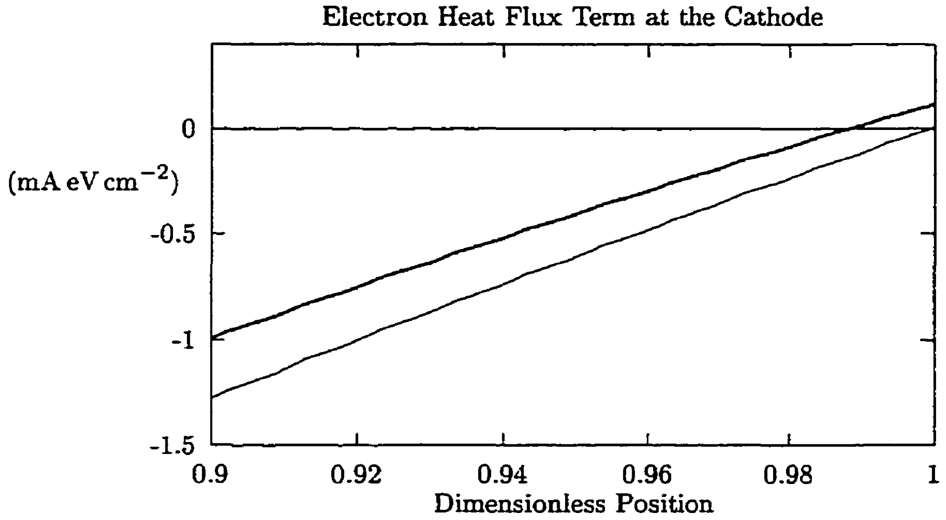

Figure 4.13: Electron heat flux at cathode: results using the electron conductivity $\tilde{K}_e$ dependent on n_e and T_e (solid bold line); and the case where $\tilde{K}_e$ depends on n_e only (solid line). For convenience, the zero-value ordinate is plotted.

on the electrode. This is in contradiction with the obtained results. It is physically unjustifiable to assume *a priori* that the net heat flux at the electrode will be dominated by the flow of particles, one has to keep in mind the fluid nature of the model when considering the boundary conditions. As discussed in section 2.2.3, we assume a known value for the electron temperature at the emitting electrode.

4.2.3 Time-dependent discharge case

Simulation results are presented in this section for time-dependent discharge over the geometry without a dielectric barrier. The applied voltage at the cathode is shown in Figure 4.14; the anode is assumed to be grounded. Plasma characteristics were studied as functions of the applied potential at the electrodes. Time-harmonic and pulse-waveform applied voltages were used with a frequency or repetition rate of 10 MHz. The results show that the plasma characteristics, averaged over the period, are not significantly affected by the shape of the applied voltage. This will no longer be the case for simulations involving a geometry with a dielectric barrier. As expected, the plasma characteristics depend significantly on the voltage difference between the anode and cathode.

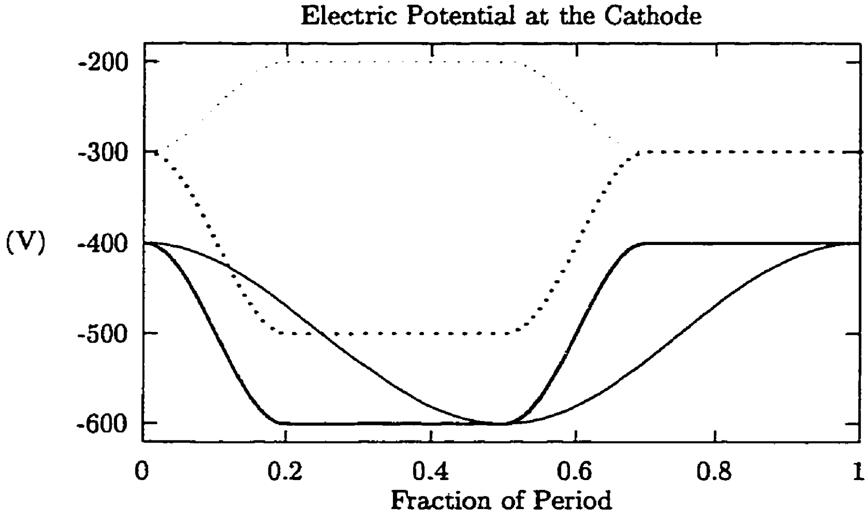

Figure 4.14: Electric potential applied at the cathode: pulse-waveform cases (solid bold, dotted, and light dotted lines); time-harmonic case (solid line). The time scale is normalized with respect to the scaling period ($1/\nu$).

The conduction currents at the cathode for pulse discharge cases are shown in Figure 4.15. Due to computer resource constraints, most of the simulations were computed for only two complete periods. However stability analyses were performed with a test case and showed good stability over 10 periods. The results are not expected to be significantly affected by the fact that periodicity was not obtained since the plasma characteristics vary much more within a period than from period to period.

As expected, the conduction current increases as the voltage between the electrodes increases.

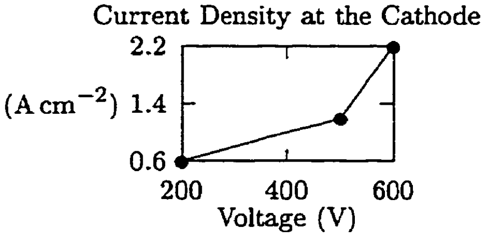

The increase of the current is not linear, as shown in the figure at left. In this figure the current density at the cathode is plotted as a function of the applied voltage at time $\tau = 0.4$ for simulations with pulse-waveform applied voltages.

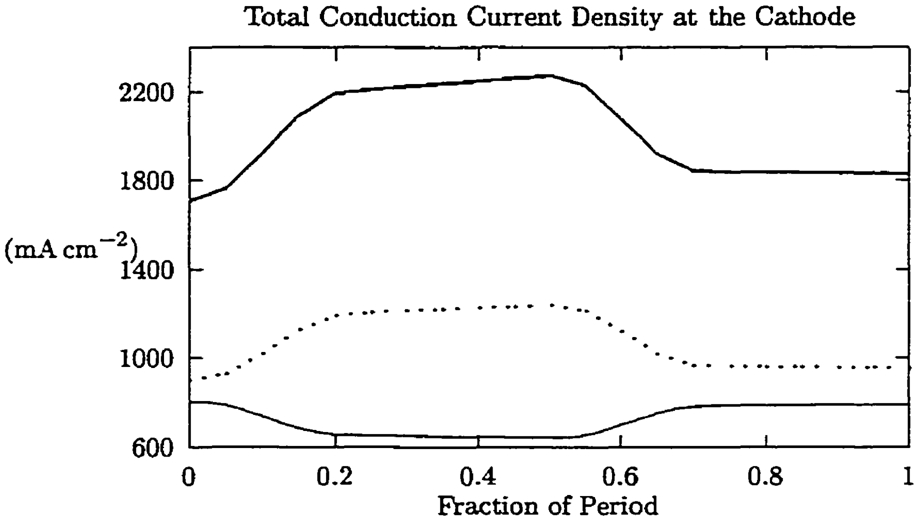

Figure 4.15: Total (electron plus ion) conduction current density at the cathode. The shape of the applied voltage is a pulse-waveform: from −400 V to −600 V (solid bold line); from −300 V to −500 V (dotted line); and from −200 V to −300 V (solid line). The time scale is normalized with respect to the scaling period ($1/\nu$).

The electric field and electron temperature are shown at four times in the period in Figure 4.16. The variation of the applied potential cause variations in the dependent variables mainly in the cathode sheath. Note that when the applied potential is maximum the electric field also reaches its maximum, as shown by the solid line in Figure 4.16, and the field in the anode sheath is at a minimum. This is related to the ambipolar diffusion mechanism discussed in section 1.1. The ion drift increases when the field increases in the cathode sheath, consequently the electric field in the anode sheath is reduced to relax the opposition of the field to the diffusion of the electrons in order to keep the plasma in quasi-neutrality.

The peak electron temperature in the cathode sheath varies considerably due to the modulation of the applied voltage. However the electron density is very small in that region, and overall, a small modulation of the electron density near the plasma sheaths is incurred by the time-varying applied potential. The ion density is practically not affected by the modulation of the

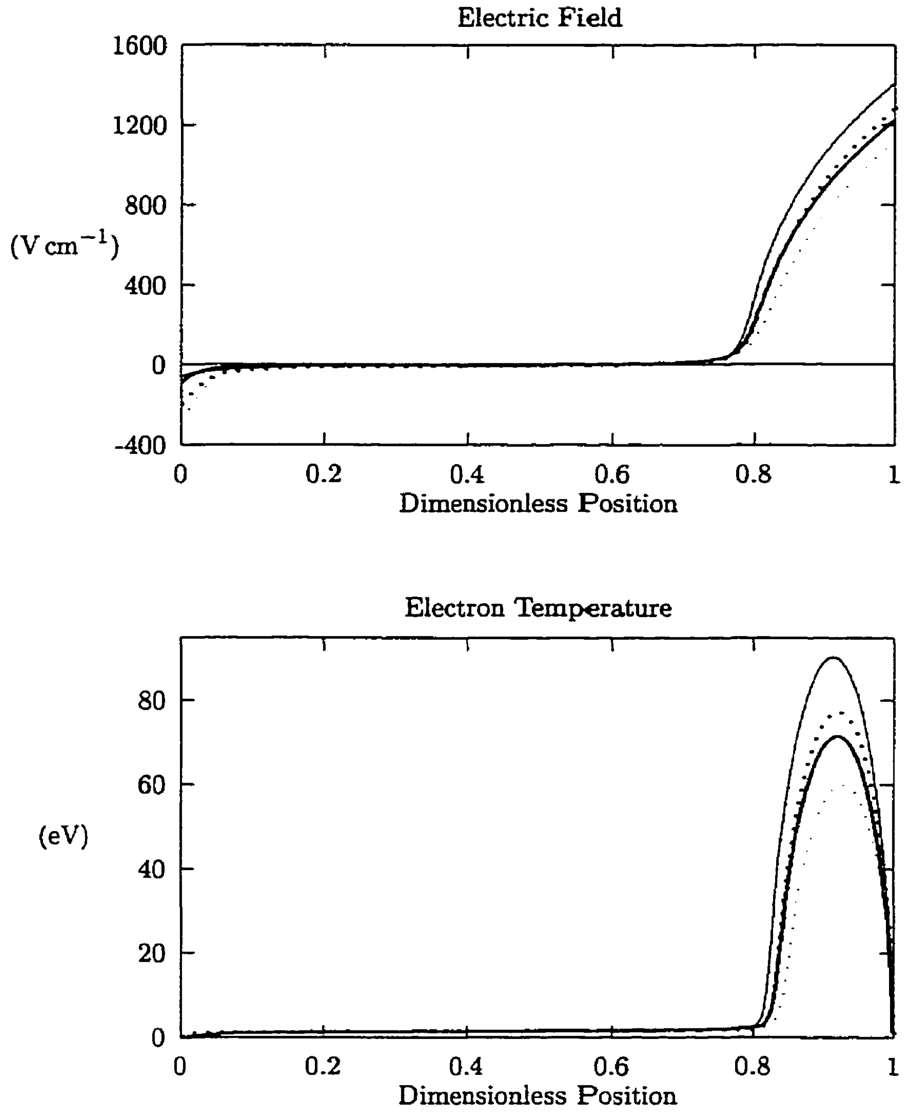

Figure 4.16: Electric field (top) and electron temperature (bottom) at different times in the period (T): 0.1 T (solid bold line); 0.4 T (solid line); 0.6 T (dotted line); and 0.9 T (light dotted line). Solution for pulse case (−400 V to −600 V). For convenience, the zero-value ordinate is plotted in the upper plot.

applied potential since it does not have time to respond at the 10 MHz frequency. Note the symmetric bell shape of the electron temperature peak in Figure 4.16, compared to the result obtained for the DC case, shown in Figure 4.6. The difference is due to the different electron thermal conductivity coefficients used, see section 4.2.2.

The electron impact ionization rate, shown in Figure 4.17, and the electron flux density, shown in Figure 4.18, show considerable modulation due to the time-varying applied voltage. Note that the electron flux is out-of-phase with the applied voltage, which denotes the capacitive nature of the discharge. The large modulation of the electron flux shows that the electrons move back and forth in the discharge space at the applied frequency. This increases their probability to experience inelastic collisions with the background gas, and translates in a greater ionization rate, by an order of magnitude, compared to the rate obtained for the DC case shown in Figure 4.6.

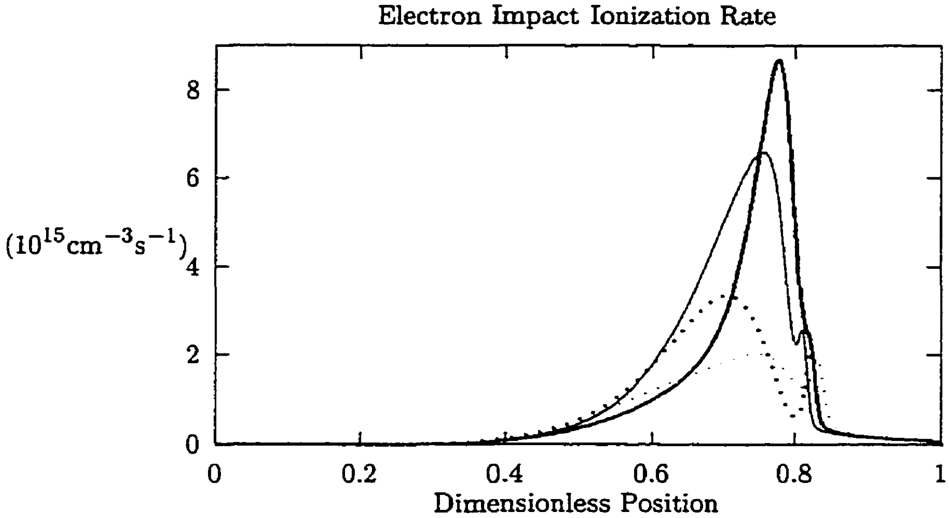

Figure 4.17: Electron impact ionization rate at different times in the period (T): 0.1 T (solid bold line); 0.4 T (solid line); 0.6 T (dotted line); and 0.9 T (light dotted line). Solution for pulse case (−400 V to −600 V).

The period-averaged plasma characteristics show little difference between the time-harmonic and pulse-waveform applied voltages. Figure 4.19 shows the

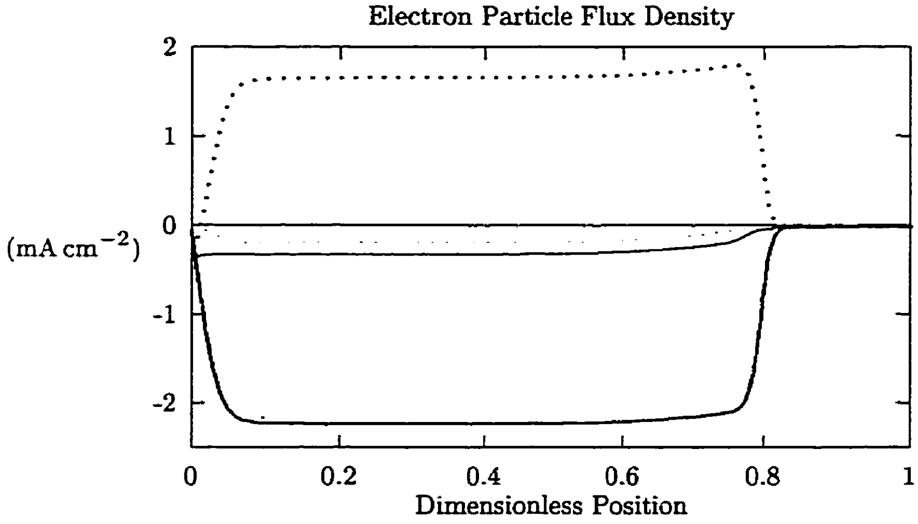

Figure 4.18: Electron flux density at different times in the period (T): 0.1 T (solid bold line); 0.4 T (solid line); 0.6 T (dotted line); and 0.9 T (light dotted line). Solution for pulse case (−400 V to −600 V). For convenience, the zero-value ordinate is plotted.

period-averaged electric field and period-integrated ionization rate obtained from simulations using time-harmonic and pulse-waveform shape applied voltages at the cathode. The other dependent variables also exhibit little difference. The rise times of the harmonic wave is 2.5 times the rise time of the pulse as seen in Figure 4.14. On one hand, the ions are not sensitive to the time-varying voltage since they are too massive to respond. On the other hand, the electrons are too mobile to be affected by the difference in the rise times between the harmonic wave and the pulse shape.

Figure 4.20 shows the period-averaged electric field and electron temperature for two simulations having the same pulse shape, but different nominal voltages. As expected, the electric field and electron temperature increase in the cathode sheath as the nominal voltage increases. However, the thickness of the plasma sheaths, the particle densities, the electric field, and the electron temperature are not appreciably changed.

The ionization rate shown in Figure 4.21 exhibits, as expected, a higher peak for the simulation having the greater applied potential at the electrodes.

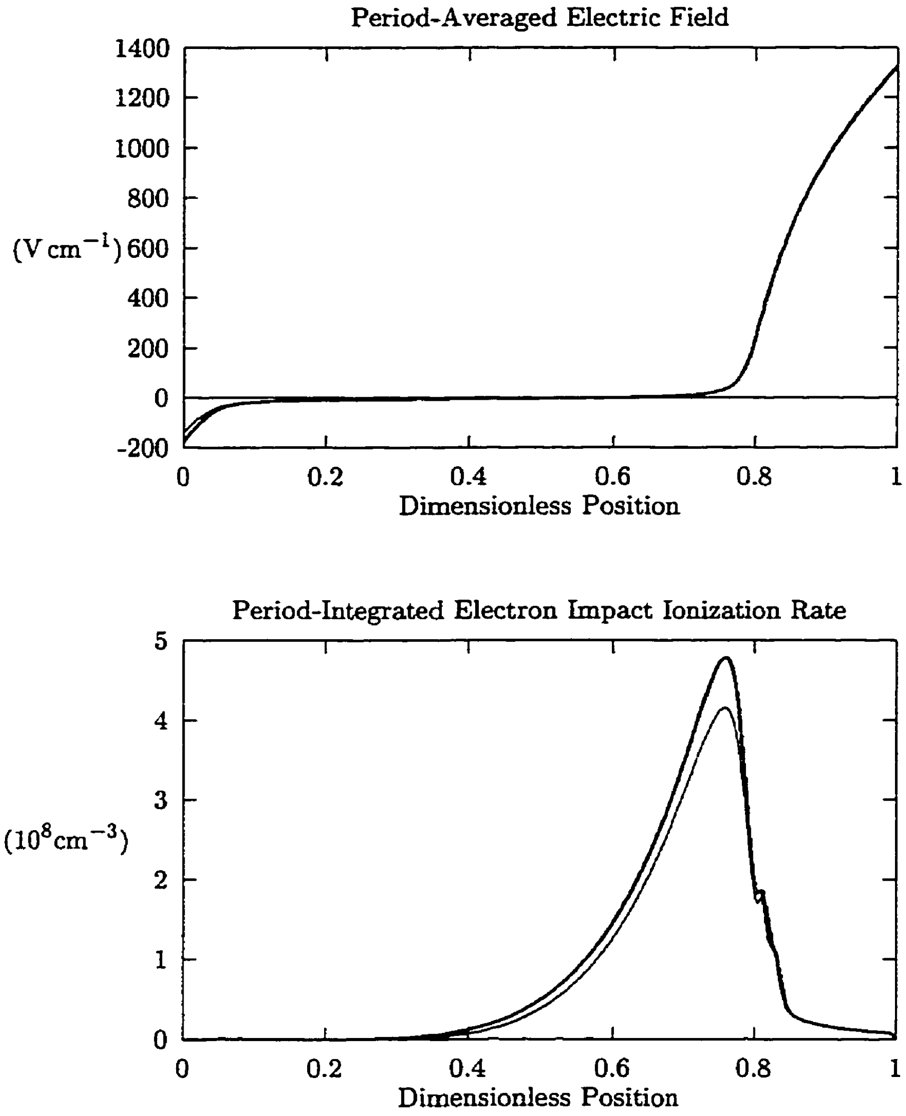

Figure 4.19: Period-averaged electric field (top) and period-integrated electron impact ionization rate (bottom), for the pulse-waveform (solid bold line) and time-harmonic (solid line) voltage cases. Solutions for applied voltage from −400 V to −600 V. For convenience, the zero-value ordinate is plotted in the upper plot.

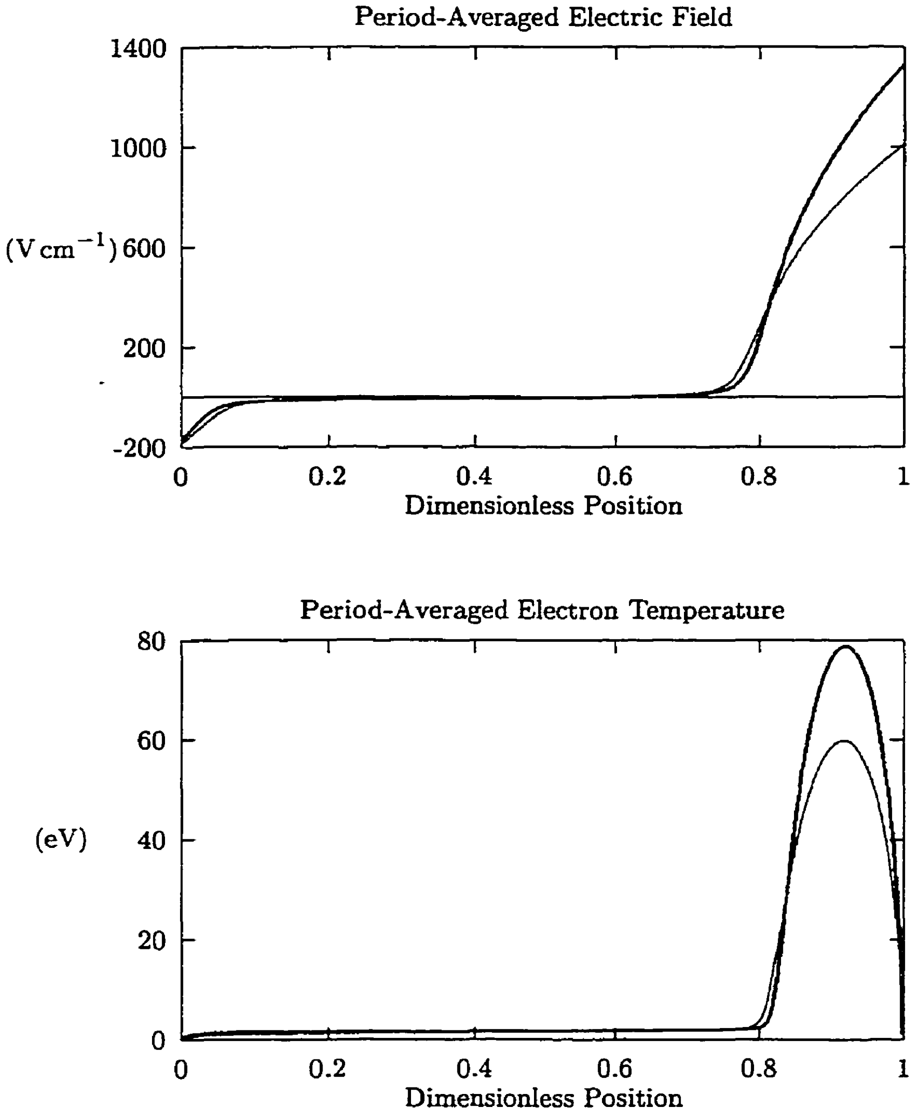

Figure 4.20: Period-averaged electric field (top) and electron temperature (bottom). The applied voltage is a pulse-waveform: from −400 V to −600 V (solid bold line); from −300 V to −500 V (solid line). For convenience, the zero-value ordinate is plotted in the upper plot.

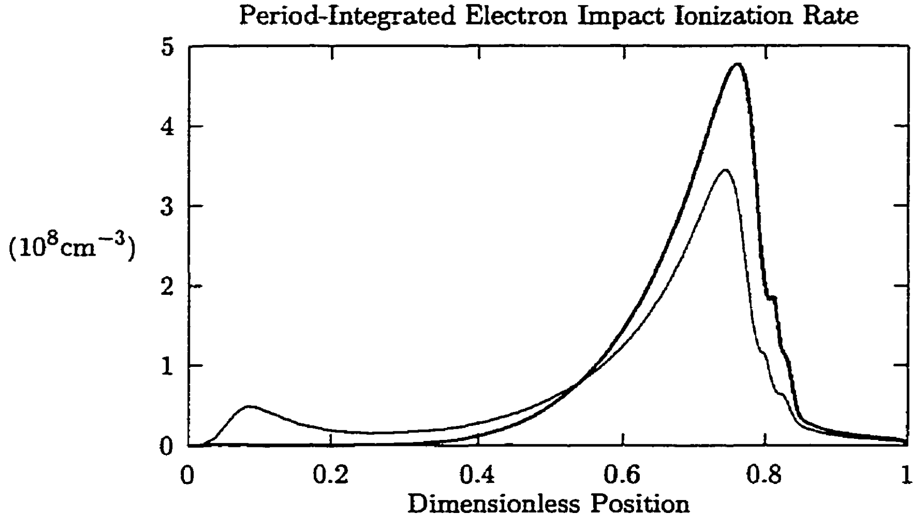

Figure 4.21: Period-integrated electron impact ionization rate. The applied voltage is a pulse-waveform: from −400 V to −600 V (solid bold line); from −300 V to −500 V (solid line).

However the smaller peak near the anode, which exists only for the lower applied voltage case, is less obvious. This secondary peak, located inside the plasma bulk near the anode sheath, results from a local heating of the electron fluid as seen by the electron Joule heating density in Figure 4.22. This region of local heating is followed by a cooling of the electrons in the anode sheath. The formation of the secondary peak results from the oscillatory motion of the electrons in the plasma, as observed by the electron flux density in Figure 4.18. The ionization mechanism, being a cumulative effect over the period, occurs when the electrons drift with the electric field (dotted line in Figure 4.18). On average, the electron flux density is dominated by the diffusion of the electrons against the electric field in that region, as seen in Figure 4.23, which is a cooling mechanism. However the modulation of the electron temperature is such that the heating of the electrons during the part of the cycle when their net motion is to drift with the electric field is more important than the cooling experienced during the part of the cycle when their diffusion against the field is the dominant transport mechanism.

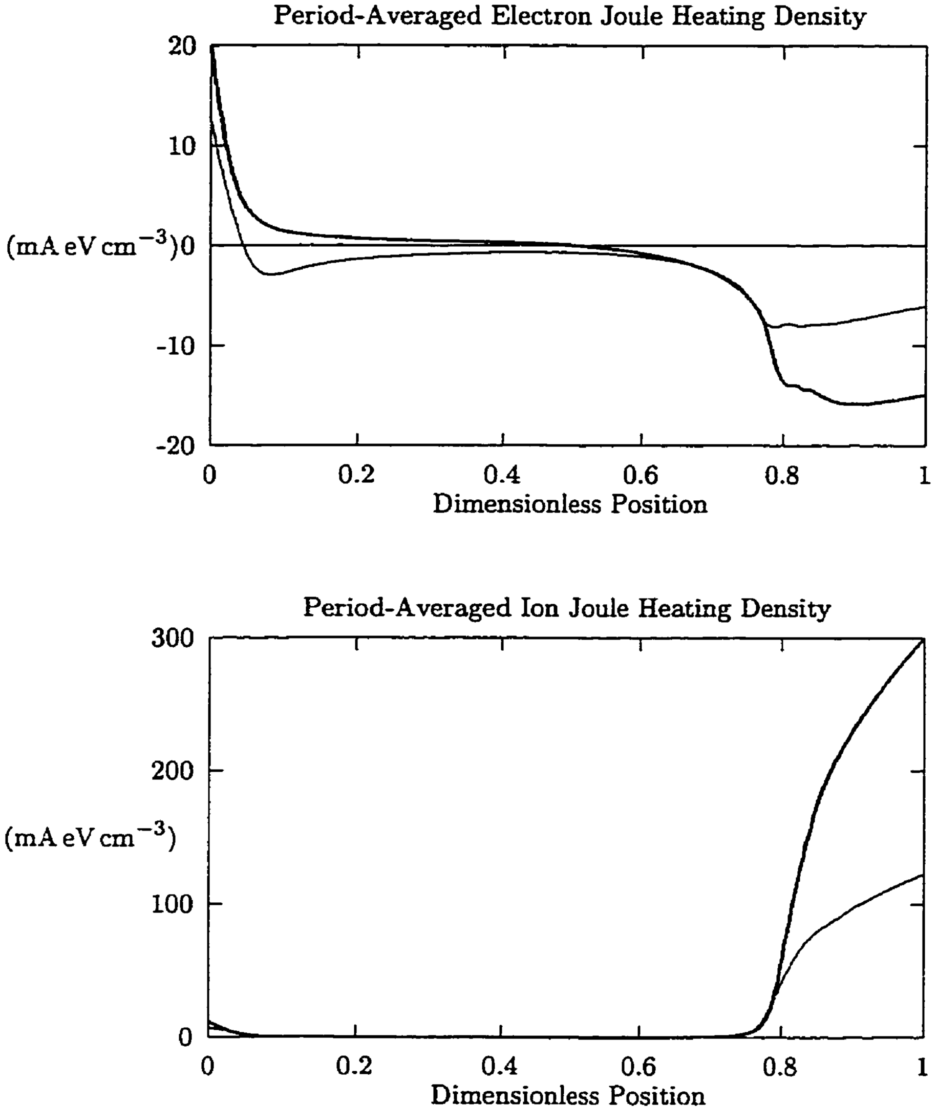

Figure 4.22: Period-averaged electron (top) and ion (bottom) Joule heating densities. The applied voltage is a pulse-waveform: from −400 V to −600 V (solid bold line); from −300 V to −500 V (solid line). For convenience, the zero-value ordinate is plotted in the upper plot.

The period-averaged total conduction current density is shown in Figure 4.23 for the two simulations with different nominal applied voltages. The total conduction current is the sum of the electron and ion current densities. The electron current density is the negative of the electron particle flux density, while the ion current density corresponds to the ion particle flux density. This is due to the charge difference between the two species. The simulation with the greater applied voltage differential across the electrodes exhibits a much larger current throughout the discharge gap. This is consistent with the observations made at the beginning of this section regarding the conduction current obtained at the cathode.

The period-averaged electron and ion Joule heating densities are shown in Figure 4.22 for two simulations obtained with different nominal applied voltages. The ion Joule heating in the cathode region is three times greater when the applied nominal voltage is increased by 33%. The applied voltage directly controls the ions' kinetic energy at the cathode, which is the desired feature for thin film deposition and surface etching. The larger ion flux at the cathode translates into a larger secondary electron emission as seen in the electron Joule heating density.

The total conduction current density and displacement current density are given at four times in the period in Figure 4.24. By its nature, the plasma contains the conduction current with a negligible displacement current. The displacement current is located in the plasma sheath. The total current density, being the sum of the conduction plus the displacement current, is conserved at all times in the period, as shown in Figure 4.25.

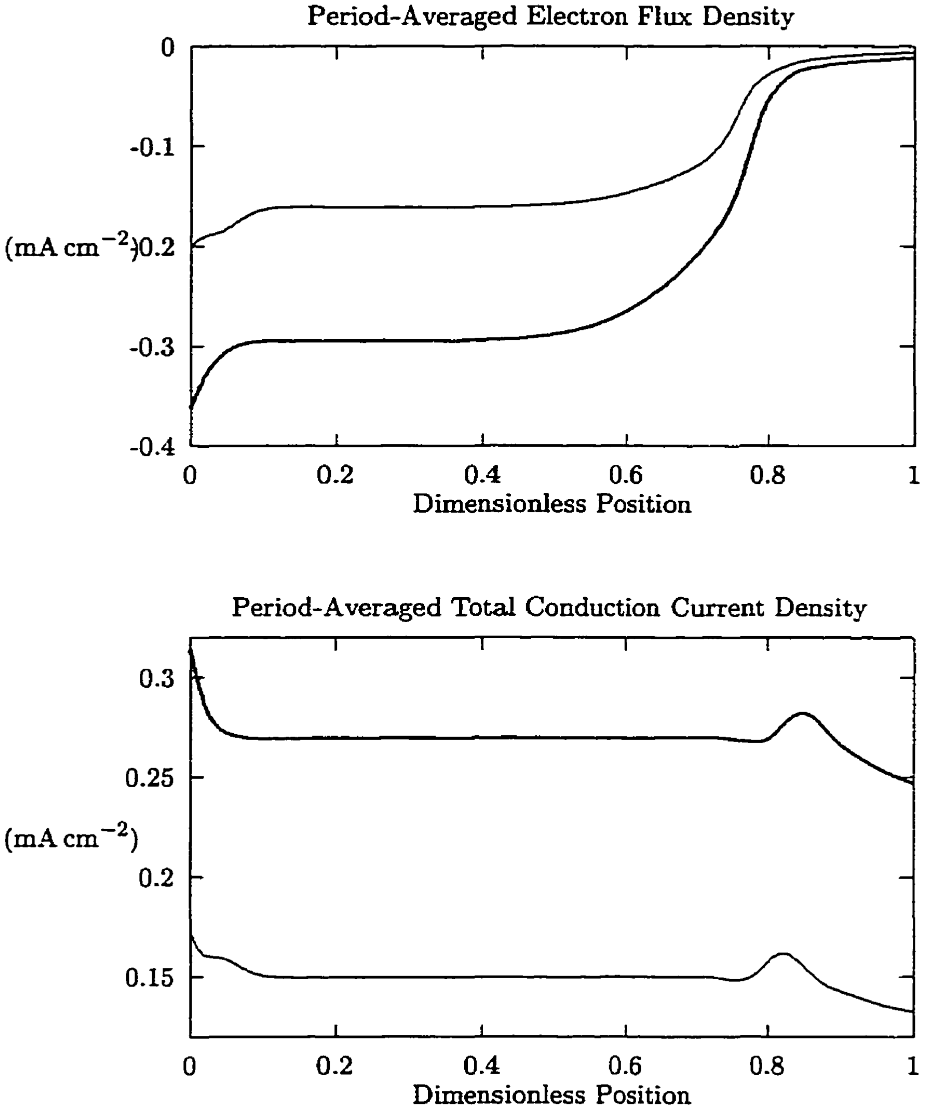

Figure 4.23: Period-averaged electron flux density (top) and period-averaged total conduction current density (bottom). The applied voltage is a pulse-waveform: from −400 V to −600 V (solid bold line); from −300 V to −500 V (solid line).

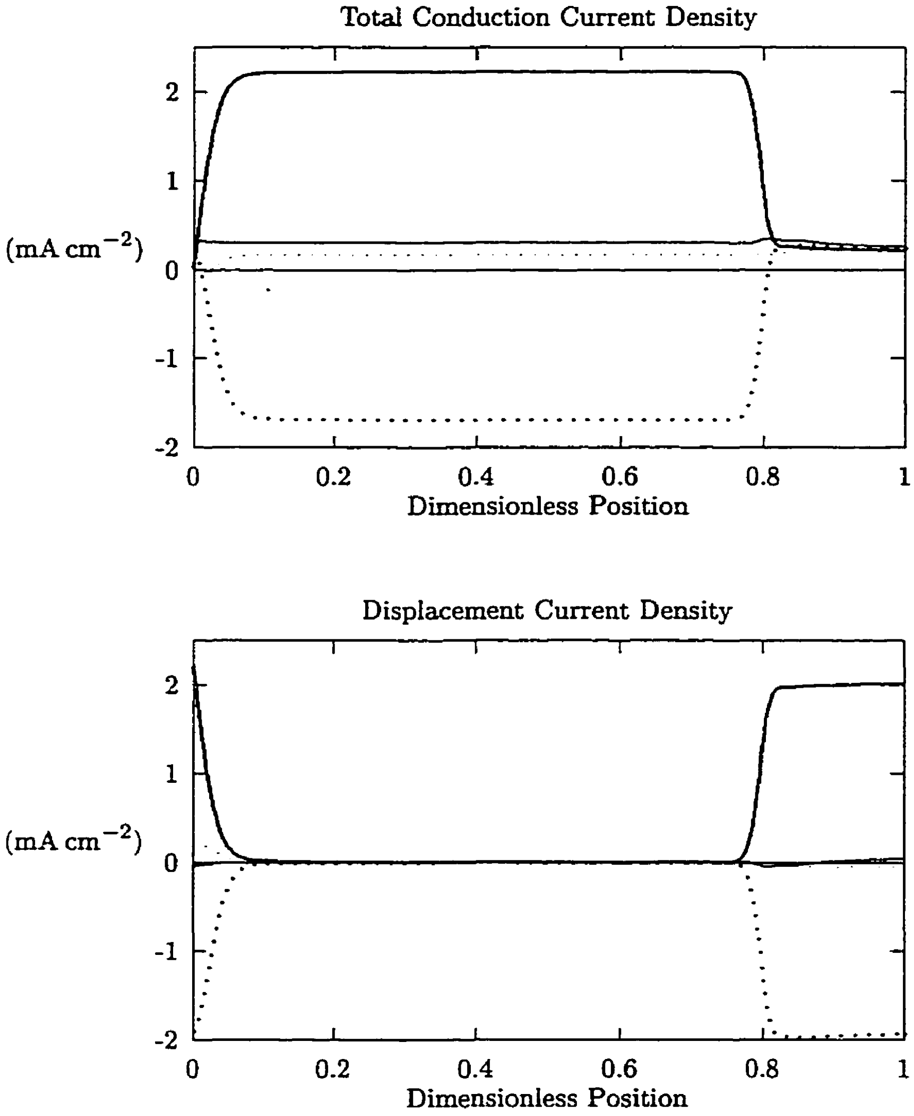

Figure 4.24: Total (electron plus ion) conduction current density (top) and displacement current density (bottom) at different times in the period (T): 0.1 T (solid bold line); 0.4 T (solid line); 0.6 T (dotted line); and 0.9 T (light dotted line). Solution for pulse-waveform case (−400 V to −600 V). For convenience, the zero-value ordinate is plotted in each case.

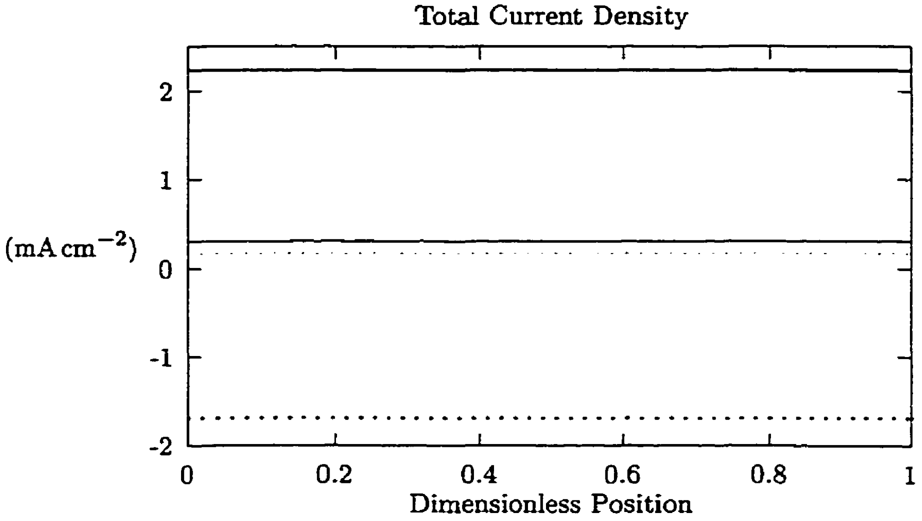

Figure 4.25: Total current density (total conduction plus displacement) at different times in the period (T): 0.1 T (solid bold line); 0.4 T (solid line); 0.6 T (dotted line); and 0.9 T (light dotted line). Solution for pulse-waveform case (−400 V to −600 V).

4.3 Geometry with dielectric barrier

The results from simulations for a discharge geometry with a 3 mm thick dielectric barrier (representing 10% of the inter-electrode space) covering the surface of the cathode are presented in this section.

A parametric study is performed to demonstrate and understand the regulating effect of the dielectric barrier on the discharge. Two permittivity constants were used, ϵ_r=5 and ϵ_r=50; and the applied voltage was set in the range of −300 to −600 V using both time-harmonic and pulse-waveform excitations. The strong nonlinear response of the plasma to the discharge conditions restricts us to vary only one parameter between simulations in order to clearly understand the effect of that parameter.

Furthermore, results are obtained from simulations which assume a static temperature for the electron fluid. Therefore, T_e is taken to be constant and uniform throughout the discharge space. As shown in section 4.2.1 this assumption cannot be justified in the ionization shock wave. However, for the purpose of this study, this assumption will permit us to focus on the effect of charge accumulation on the surface of the dielectric barrier and to show that the regulation mechanism of the barrier on the discharge originates in the modification of the thicknesses of the cathode sheath and ionization shock wave regions.

In section 4.3.1, results are presented for simulations of DC discharge assuming no charge accumulation on the surface of the dielectric. Charge accumulation is studied with a constant applied voltage: in section 4.3.2 assuming a static electron temperature; and in section 4.3.3 for a self-consistent electron temperature (full model).

Finally, discharge with a time-varying applied voltage is studied for the full two-fluid plasma model in section 4.3.4.

4.3.1 DC solution

Results from simulations for the DC case are presented in this section. The cathode is covered by a dielectric barrier occupying 10% of the discharge space.

Two permittivity constants for the dielectric material are considered, ϵ_r=5 and ϵ_r=50. In the figures, the plasma-dielectric barrier boundary is marked by an arrow (⇑).

Simulations were conducted for discharge conditions for both −300 V and −400 V applied at the cathode (with respect to grounded anode). For simulations assuming a static temperature for the electron fluid, a temperature of 1.6 eV is assumed. This constant electron temperature was used in the ionization rate equation (2.35).

The electric potential distribution is shown in Figure 4.26. Inside the dielectric barrier the potential is linear since no free charge exists. The potential distribution from simulations with a barrier of different permittivity, with all other parameters unchanged, exhibits a difference only at the plasma-dielectric boundary and inside the barrier (dotted and light dotted lines).

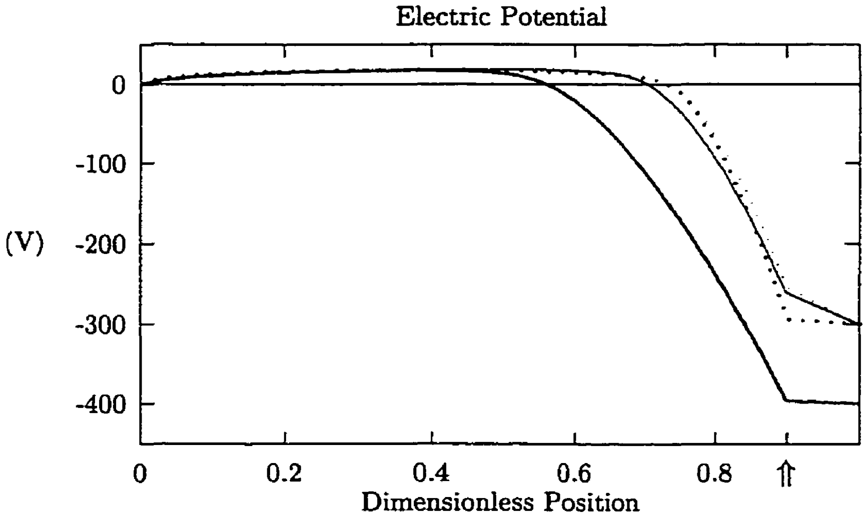

Figure 4.26: Electric potential when the cathode is covered with a dielectric barrier of 3 mm thick (⇑). Full model case with ϵ_r=50 and −400 V applied at the cathode (solid bold line); ϵ_r=5 and −300V applied at the cathode (solid line). Electron fluid with a static temperature case, ϵ_r=50, and −300 V applied at the cathode (dotted line); ϵ_r=5 and −300 V applied at the cathode (light dotted line). For convenience, the zero-value ordinate is plotted.

Results from simulations for the case with a static temperature for the electron fluid compared to the case without that assumption (full model) show a difference mainly in the cathode sheath (Figure 4.26, solid line and light dotted line). The potential distribution is more sensitive to the applied potential at the cathode than to the permittivity of the dielectric barrier.

Simulation results for an applied voltage at the cathode of −400 V compared to −300 V, using the full model, present differences not only in the dielectric barrier but also in the whole cathode sheath and, more importantly, yield different sheath thicknesses.

The electric field is shown in Figures 4.27 and 4.28. In Figure 4.27 the simulation results are shown for cases with static electron temperature and with different material permittivities (solid and dotted lines). Note the larger discontinuity in the electric field at the surface of the dielectric barrier for the higher permittivity constant. For comparison, simulations using the full model are also shown (solid bold line).

The electric field extends farther into the discharge space when the electron temperature is computed self-consistently, indicating a thicker plasma sheath. The plasma sheath increased further as the applied voltage was increased as shown in Figure 4.28.

As it was observed for results obtained with a static electron temperature, the electric field distribution in the plasma sheath is relatively unchanged when a different material permittivity is used, compared to the change in the field distribution when a different applied voltage is used. The plasma is confined in a much reduced region when the applied voltage is increased. For the geometry without a dielectric barrier, converged DC solutions could not be obtained for an applied voltage of −400 V, indicating a degeneration of the discharge towards an uncontrolled breakdown.

The electron and ion densities obtained from simulations with static electron temperature, and from the full model are shown in Figure 4.29. The much larger density distribution for the static electron temperature case is needed to sustain the discharge (the ionization rate depends linearly on the electron

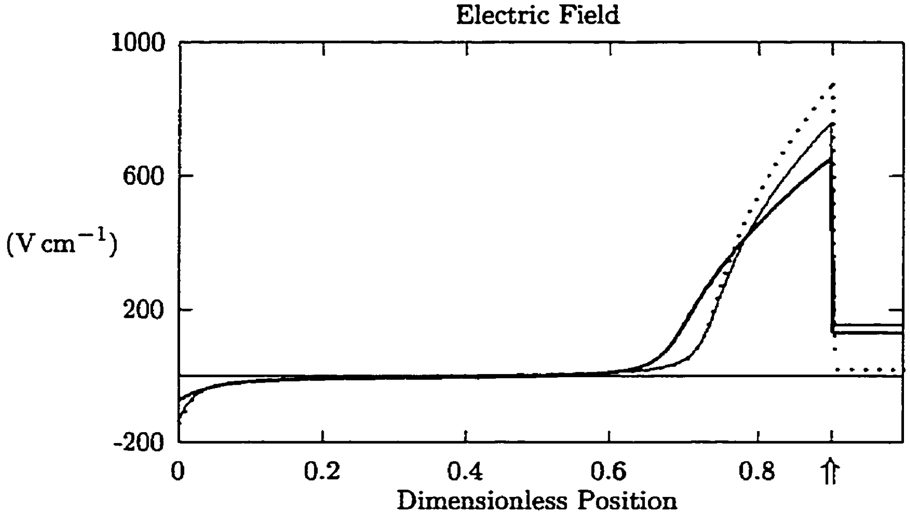

Figure 4.27: Electric field when the cathode is covered with a dielectric barrier (⇑). Full model case with ϵ_r=5 (solid bold line). Electron fluid with static temperature case, ϵ_r=5 (solid line); ϵ_r=50 (dotted line). The applied potential at the cathode is −300 V. For convenience, the zero-value ordinate is plotted.

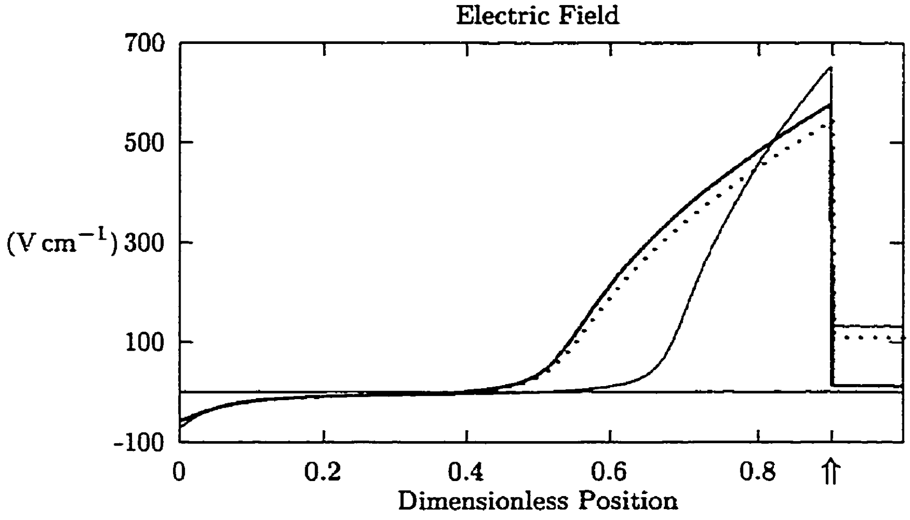

Figure 4.28: Electric field when the cathode is covered with a dielectric barrier (⇑). Full model case with ϵ_r=50 and −400 V applied at the cathode (solid bold line); ϵ_r=5 and −400 V applied at the cathode (dotted line); ϵ_r=5 and −300 V applied at the cathode (solid line). For convenience, the zero-value ordinate is plotted.

number density). The sustaining mechanism in the full model is the high temperature gradient in the ionization shock wave and the high value in the cathode sheath, see Figure 4.30.

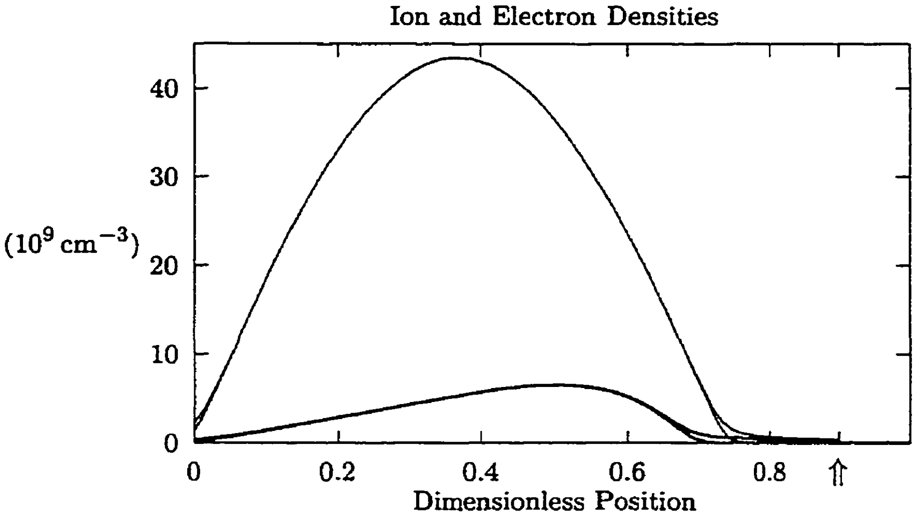

Figure 4.29: Electron and ion charge densities when the cathode is covered with a dielectric barrier with ϵ_r=5 (⇑). Full model case (solid bold line). Static electron temperature case (solid line). The applied potential at the cathode is −300 V.

The electron temperature distribution is shown in Figure 4.30. As expected, simulations with a larger electric field in the cathode sheath give a larger electron temperature peak. The increased width of the electron temperature peak is considerable when the applied voltage magnitude at the cathode is increased from −300 V to −400 V. Surprisingly, this has the opposite effect on the ionization rate as shown in Figure 4.31 (solid bold line versus solid line). This is key to the regulation mechanism of the dielectric barrier on the discharge process. Note that the main effect of the material permittivity on the temperature distribution is on the height of the peak.

The ionization rate obtained from the simulation for a discharge without a dielectric barrier (light dotted line) is shown in Figure 4.31, along with the ionization rate obtained from a simulation with the same discharge conditions

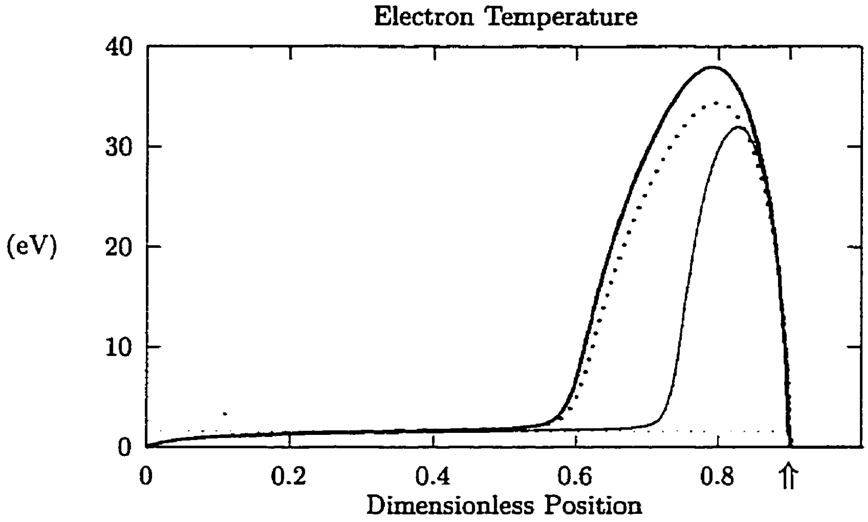

Figure 4.30: Electron temperature distribution when the cathode is covered with a dielectric barrier (⥣). Full model case with ϵ_r=50 and −400 V applied at the cathode (solid bold line); ϵ_r=5 and −400 V applied at the cathode (dotted line); ϵ_r=5 and −300 V applied at the cathode (solid line). Simulation with static electron temperature, T_e=1.6 eV throughout the discharge gap (light dotted line).

with the addition of a dielectric barrier having ϵ_r=5 (solid line). Obviously the ionization rate is shifted inward in the discharge space due to the presence of the barrier. However, which is perhaps less obvious, the ionization rate is considerably reduced. Therefore the presence of the barrier "chokes" the discharge, independent of the permittivity of the material.

Intuitively, one would imagine that by increasing the applied voltage, in order to compensate for the potential drop in the barrier, the ionization rate would recover the level obtained when no dielectric barrier is present. This is not the case, as seen by comparing the bold solid line to the solid line in Figure 4.31.

The electron and ion flux densities are shown in Figure 4.32. Note that the simulation with a higher material permittivity gives a smaller particle flux. Therefore, as it will be shown later, increasing the material permittivity does contribute to limiting the discharge current. The advantage of a higher material

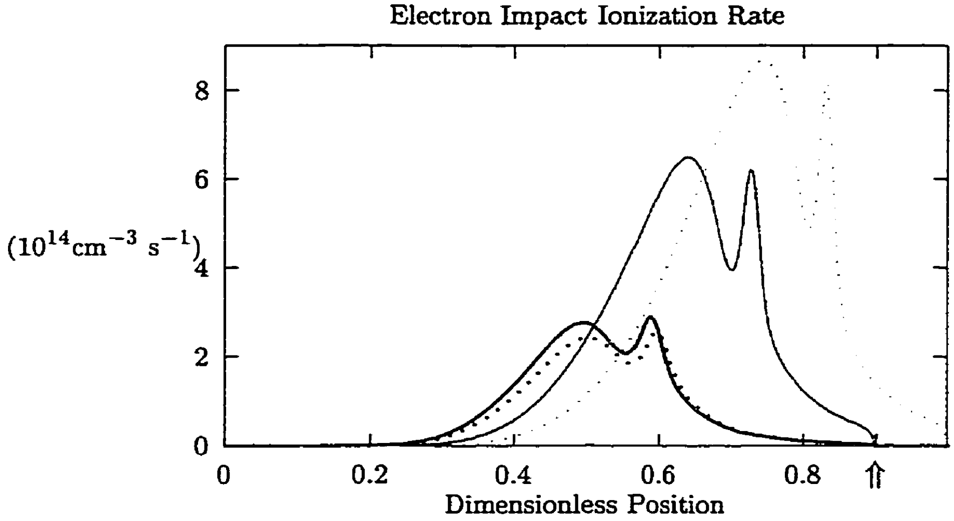

Figure 4.31: Electron impact ionization rate. The cathode is covered with a dielectric barrier (⇑): ϵ_r=50 and −400 V applied at the cathode (solid bold line); ϵ_r=5 and −400 V applied at the cathode (dotted line); ϵ_r=5 and −300 V applied at the cathode (solid line). System without dielectric barrier, using −300 V applied at the cathode (light dotted line).

permittivity will be more significant for time-dependent discharges.

Drift and diffusion contributions to the electron particle flux are shown in Figure 4.33. The drift and diffusion fluxes are qualitatively similar to those obtained without the dielectric barrier, Figure 4.8. Note, however, the increased plasma sheath thickness when the barrier is present.

The total conduction current is shown in Figure 4.34 for various applied voltages and material permittivity constants. Simulations with a static electron temperature give a higher conduction current (solid bold line and dotted line). Results obtained from simulations with the full model give a lower conduction current for equivalent discharge conditions and material properties (solid line versus solid bold line). Full model results for a higher applied voltage exhibit a lower conduction current (light dotted line and spaced dotted line). Note that one can increase the conduction current by using a material with a higher permittivity (light dotted line versus spaced dotted line).

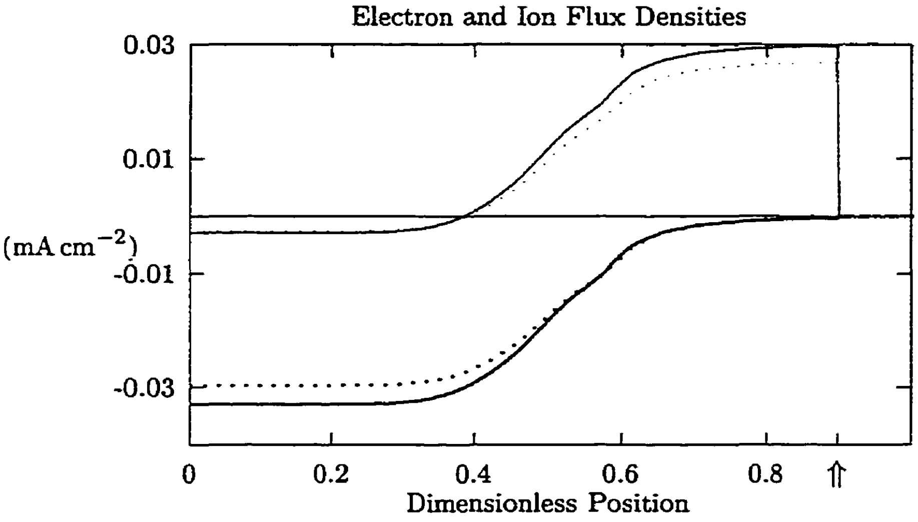

Figure 4.32: Electron and ion flux densities when the cathode is covered with a dielectric barrier (⇑). Full model case with ϵ_r=50: electron current densities (solid bold line); and ion current densities (line). Full model case with ϵ_r=5: electron current densities (dotted line); and ion current densities (light dotted line). The applied potential at the cathode is −400 V. For convenience, the zero-value ordinate is plotted.

The electron thermal conduction and enthalpy flux contributions to the electron heat flux are given in Figure 4.35 for discharge conditions with −300 V applied at the cathode. Similar results are obtained with −400 V applied at the cathode, however the heat flux peaks at −0.6 mA eV/cm^2.

Electron and ion Joule heating terms are given in Figure 4.36. The ion Joule heating for discharge conditions with −300 V applied at the cathode has a relatively high heating in the cathode sheath resulting in a considerable secondary electron emission as seen by the electron Joule heating term. These electrons are responsible for the larger ionization rate in the cathode sheath compared to the result obtained with −400 V applied at the cathode, as shown in Figure 4.31.

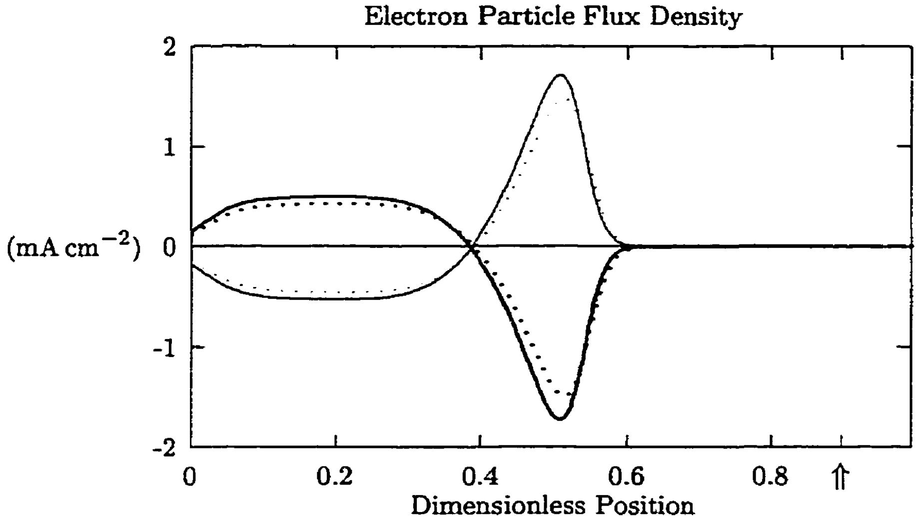

Figure 4.33: Drift and diffusion contributions to the electron flux when the cathode is covered with a dielectric barrier (⇑). Case ϵ_r=50, drift (solid bold line) and diffusion (solid line) contributions. Case ϵ_r=5, drift (dotted line) and diffusion (light dotted line) contributions. The applied potential at the cathode is −400 V. For convenience, the zero-value ordinate is plotted.

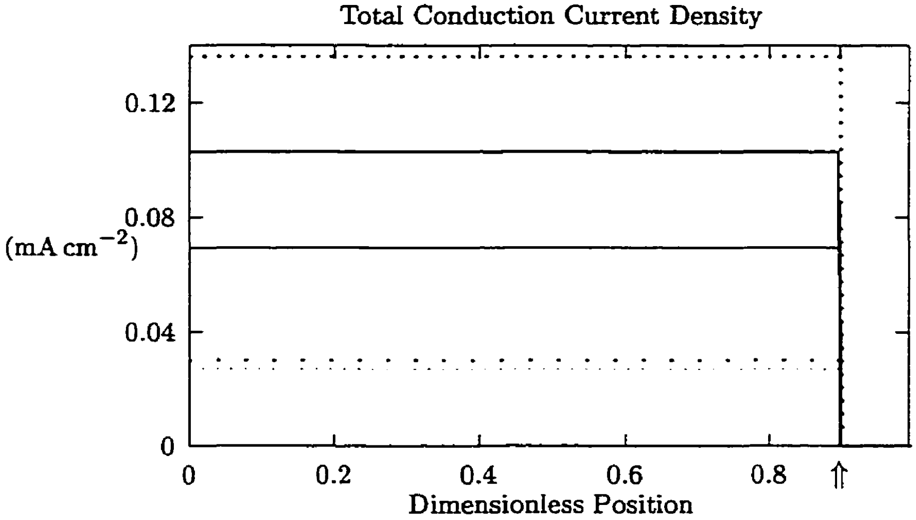

Figure 4.34: Total conduction current when the cathode is covered with a dielectric barrier (⇑). Static electron temperature case with −300 V applied at the cathode, ϵ_r=5 (solid bold line) and ϵ_r=50 (dotted line). Full model case with ϵ_r=5 and −300 V at the cathode (solid line). Full model case with −400 V at the cathode, ϵ_r=5 (light dotted line) and ϵ_r=50 (spaced dotted line).

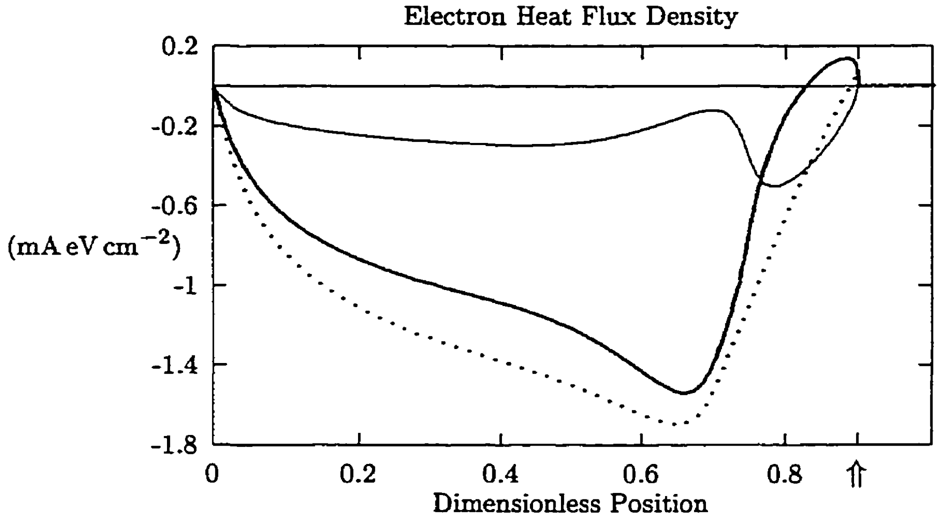

Figure 4.35: Electron heat flux density when the cathode is covered with a dielectric barrier, ϵ_r=5 (⇑). Electron thermal conduction (solid bold line) and electron flux (solid line) contributions to the electron heat flux term (dotted line). Applied potential at the cathode is −300 V. For convenience, the zero-value ordinate is plotted.

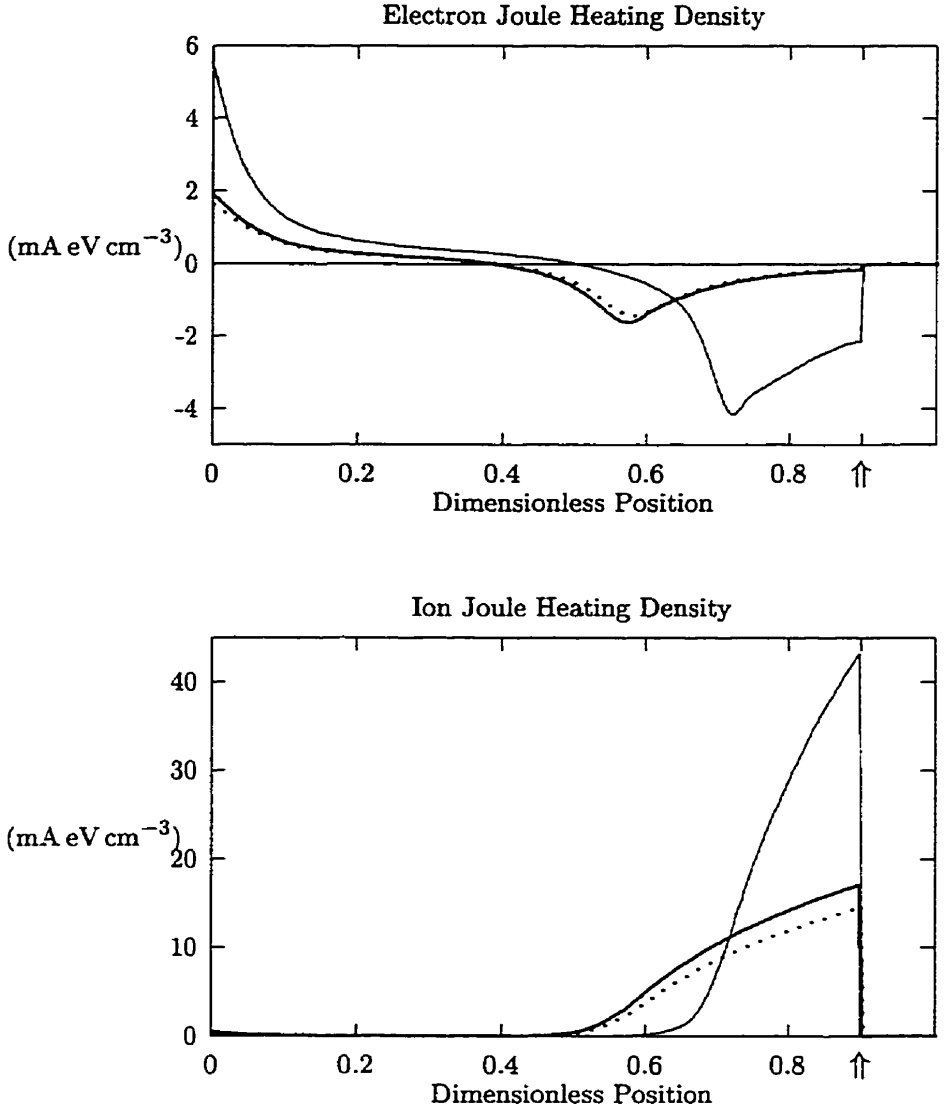

Figure 4.36: Electron and ion Joule heating are shown in the upper and lower plots respectively, for discharge with the cathode covered with a dielectric barrier (⇑). Case ϵ_r=50 and −400 V applied at the cathode (solid bold line). Case ϵ_r=5 and −400 V applied at the cathode (dotted line); −300 V applied at the cathode (solid line). For convenience, the zero-value ordinate is plotted in the upper plot.

4.3.2 Charge accumulation on dielectric barrier for electron fluid with a static temperature case.

The charge accumulation on the surface of the dielectric barrier is a self-induced time-dependent mechanism that leads to the extinction of the discharge. By its nature, it is different from the external force driven time-dependent behavior studied in section 4.2.3.

In this section we present results from simulations with the assumption of a static temperature for the electron fluid. A virtual frequency of $\nu = 0.1\,\text{MHz}$ is taken to put the equations in a non-dimensional form. Time is denoted in terms of periods of $10\,\mu s$.

The applied voltage at the cathode is $-300\,\text{V}$ (with respect to grounded anode), and constant in time. The electric field distribution is shown at three times during the charge accumulation process in Figure 4.37. The initial electric field corresponds to the DC solution presented in the previous section.

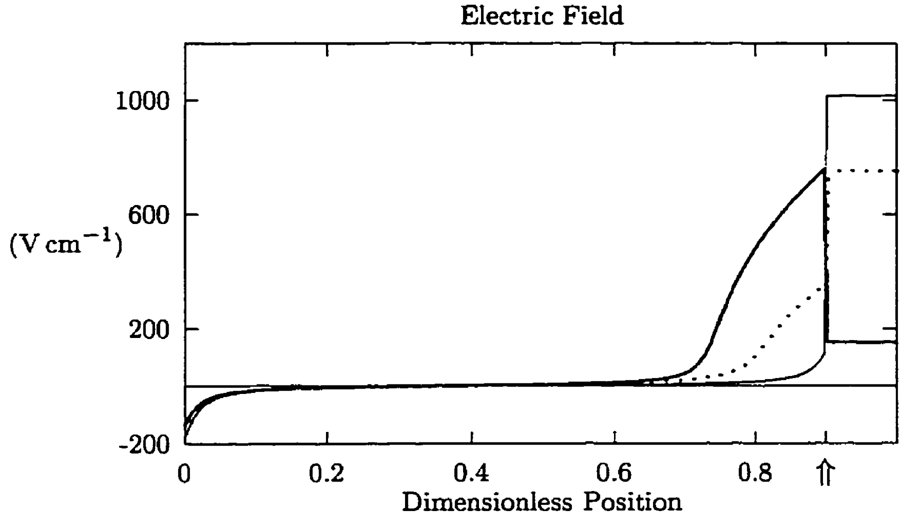

Figure 4.37: Electric field for charge accumulation on the dielectric barrier having ϵ_r=5 (⇑). Initial electric field without surface charge (solid bold line); after half period (dotted line); after five periods; steady-state configuration (solid line). For convenience, the zero-value ordinate is plotted.

Initially the ions drift towards the barrier and accumulate on it. The self-consistent field due to the surface charge density screens the applied field due to the electrodes. As seen in Figure 4.37, after five periods the surface charge field practically screens the total applied field. As a result, a large electric field exists in the barrier. One of the difficulties in making electrodes with dielectric barriers for plasma air remediation is that the barrier must have sufficient dielectric strength to avoid breakdown in the barrier.

A larger material permittivity for the barrier increases its capacity to accumulate surface charge as seen in Figure 4.38. A simple circuit analysis, modeling the plasma as a resistor R and the dielectric barrier as a capacitor C, yields the surface charge accumulation in time as:

$$\sigma(\tau) \approx \sigma_{max}\left(1 - e^{-\tau/RC}\right).$$

The characteristic time constant is $\tau_{RC} = RC$, at which time the surface charge density is $\sigma(\tau_{RC}) \approx 0.632\,\sigma_{max}$. We have from Figure 4.38 that σ_{max} is $2.31\,\mathrm{cm}^{-2}$ and $0.227\,\mathrm{cm}^{-2}$ for ϵ_r=50 and 5 respectively, which corroborate the fact that a 10-fold increase in permittivity results in a 10-fold increase in the "charge storage" capacity. The characteristic time constants are 2.6 and 0.45, in terms of the normalized time scale, for ϵ_r=50 and ϵ_r=5 respectively. The ratio of the characteristic time constants is 5.7, i.e., the barrier with ϵ_r=5 will saturate 5.7 times faster than the barrier with ϵ_r=50. This is in agreement with the results shown in Figure 4.38.

Note the disappearance of the high electric field in the cathode sheath in Figure 4.37 as the ions accumulate on the dielectric barrier. As a consequence, the electrons are now able to diffuse and occupy the region close to the barrier as shown in Figure 4.39. Therefore, the electrons will start to diffuse and stick to the surface of the barrier as shown in Figure 4.40. Note that the electron surface density is negligible compared to the ion surface density. This results from the electron-ion recombination term in the surface charge density equation of motion, as given by equations (2.62) and (2.63):

$$k_r^\sigma\,\sigma_e\,\sigma_{ion}.$$

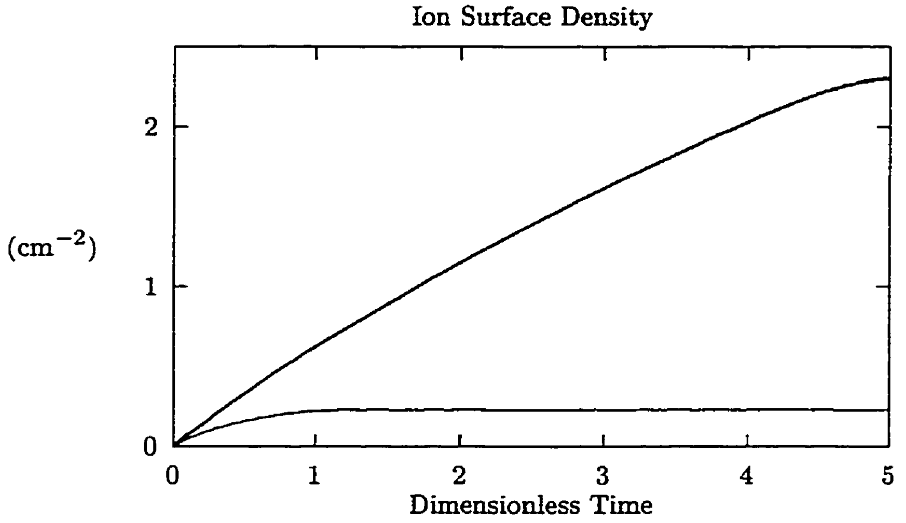

Figure 4.38: Ion surface density accumulating on the dielectric barrier. Case ϵ_r=50 (solid bold line); ϵ_r=5 (solid line). The time scale is normalized with respect to the scaling period $(1/\nu)$.

. The process is as follows. The ions accumulate due to their drift motion toward the barrier. As they accumulate they screen the applied field resulting in the disappearance of the high field region.

When the field is sufficiently low, the electrons are able to diffuse against the field and start to accumulate on the barrier. Since an ion density exists at the surface when the first few electrons hit the barrier, most of them are recombined with existing ions. Each time a recombination process occurs one electron and one ion are removed from the dielectric surface. Figure 4.40 indicates that the source of electrons at the barrier is greater than the sink resulting in a net increase. When the electrons start to accumulate on the barrier, at time $\tau \approx 1$ their rate of accumulation is maximum; the electron-ion recombination is negligible since it is proportional to σ_e.

Note that the peak electron density increases in Figure 4.39 as the charges accumulate on the dielectric barrier. This is due to the artificially maintained discharge due to the assumed static electron temperature.

The ion particle flux density is shown in Figure 4.41. As expected, the ion

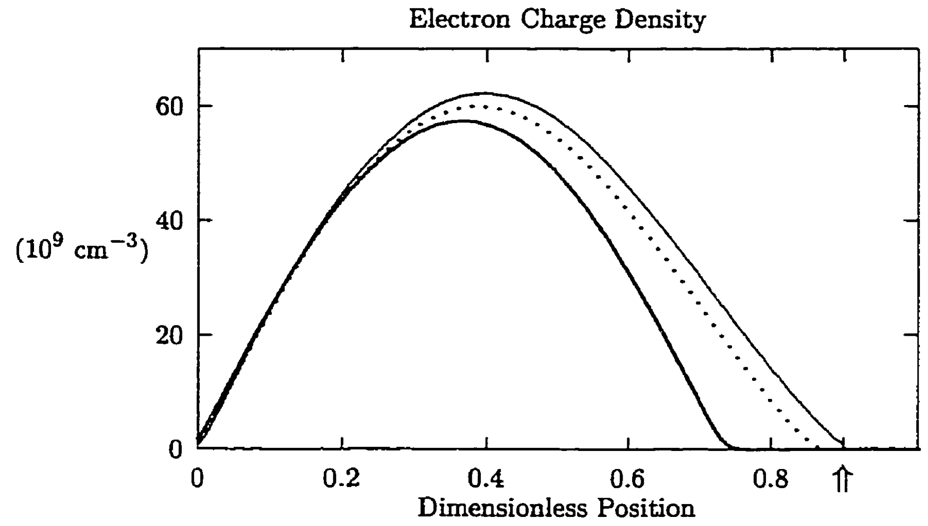

Figure 4.39: Electron density as charges accumulate on the dielectric barrier, ϵ_r=50 case (⇑). Initial density without surface charge (solid bold line), after four periods (dotted line), after five periods (solid line).

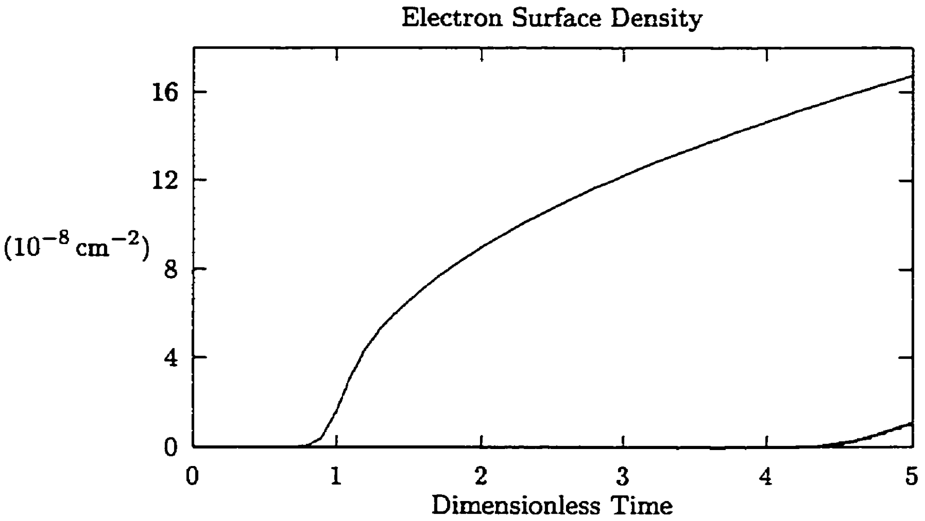

Figure 4.40: Electron surface charge accumulation on the dielectric barrier. Case ϵ_r=50 (solid bold line); ϵ_r=5 (solid line). The time scale is normalized with respect to the scaling period $(1/\nu)$.

flux at the surface of the dielectric barrier is decreased as the surface charges accumulate on the barrier.

The drift and diffusion components to the electron flux are shown in Figure 4.42. The electrons, being more mobile than the ions, are affected more by the disappearance of the high field region. This is accentuated by the fact that the net electron flux results from a concurrence between diffusion and drift, while in the case of the ions, the diffusion and drift components are both directed toward the barrier.

The net electron flux and the total conduction current are shown in Figure 4.43. Note the current reversal after five periods, due to the dominant process of electron diffusion.

The total conduction current is conserved which indicates a negligible displacement current. This means that the time required to accumulate an amount of charge sufficient to influence the plasma is much greater than the plasma response time.

4.3.3 Charge accumulation on dielectric barrier, full model.

The results from simulations studying the charge accumulation on the dielectric barrier for a constant applied voltage of 300 V across the electrodes are presented in this section. The full model is used, i.e., the electron temperature is self-consistent. A virtual frequency of $\nu = 10\,\text{MHz}$ is used to put the equations in a non-dimensional form.

The inclusion of the electron temperature equation considerably increases the stiffness of the equations of the model. This forces us to use much smaller time steps compared to the case when the electrons are assumed to have a static temperature. To make the simulations tractable, we used a driving frequency of 10 MHz for the time-dependent applied voltage at the electrodes. This frequency is in the range of frequencies used in thin film deposition and plasma etching.

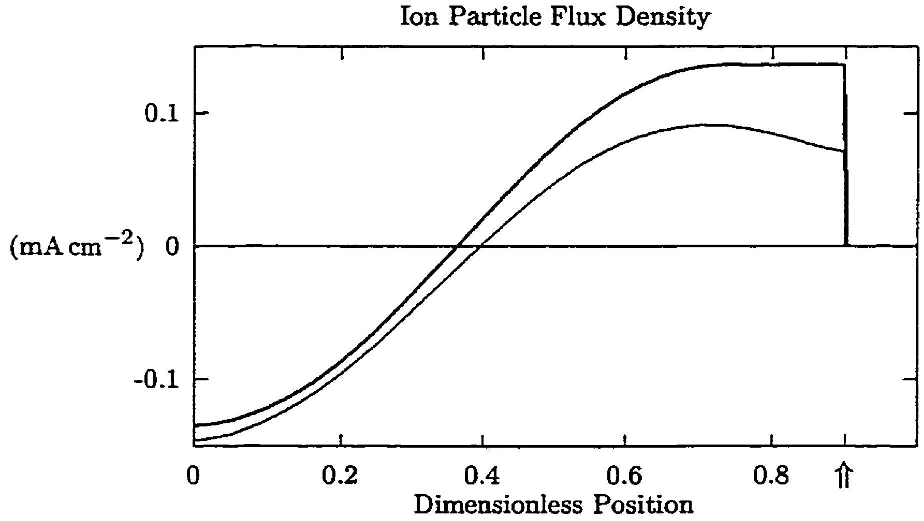

Figure 4.41: Ion flux density as charges accumulate on the dielectric barrier, ϵ_r=50 case (⇑). Initial flux density without surface charge (solid bold line); after five periods (solid line). For convenience, the zero-value ordinate is plotted.

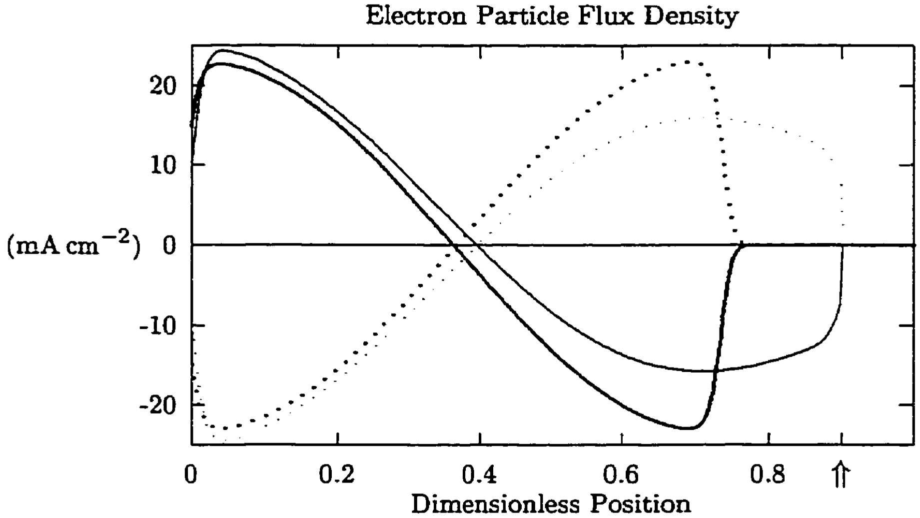

Figure 4.42: Electron flux density as charges accumulate on the dielectric barrier, case ϵ_r=50 (⇑). Drift component without surface charge (solid bold line); after five periods (solid line). Diffusion component without surface charge (dotted line); after five periods (light dotted line). For convenience, the zero-value ordinate is plotted.

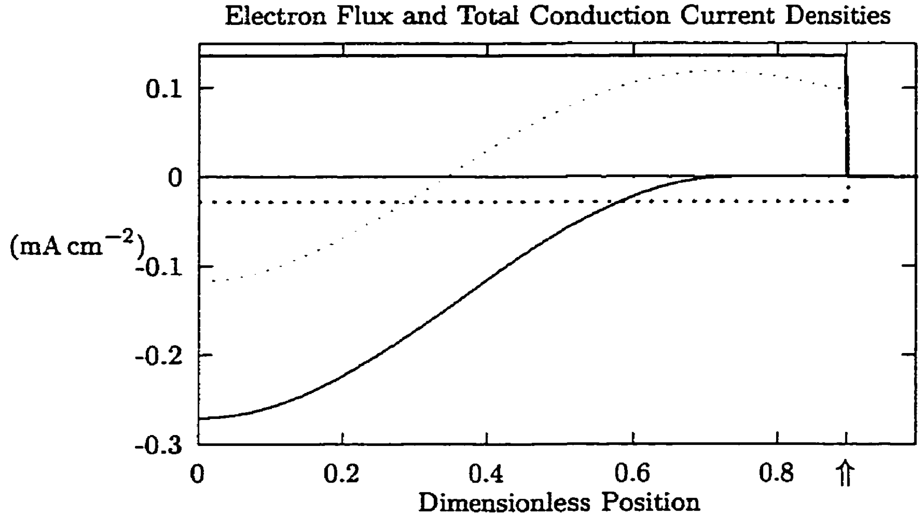

Figure 4.43: Electron and total conduction current densities as charges accumulate on the dielectric barrier, ϵ_r=50 case (⇑). Total conduction current density without surface charge (solid bold line); after five periods (dotted line). Electron current density without surface charge (solid line); after five periods (light dotted line). For convenience, the zero-value ordinate is plotted.

The charge accumulation during one period is not appreciable due to two factors: the discharge being at low pressure results in fewer charges that accumulate on the barrier, and the relatively high frequency, compared to the frequencies used in high pressure discharge, does not give much time for the surface charge to accumulate.

However, studying the impact of surface charge accumulations during one period will give clear indications that the discharge could not be maintained.

The electric field distribution shows practically no change after one cycle as shown in Figure 4.44. The ion accumulation is shown in Figure 4.45.

The electron temperature also shows little change after one cycle of charge accumulation as shown in Figure 4.46. The only change is in the height of the temperature peak in the cathode sheath. Surprisingly, in the same figure, the ionization rate shows relatively important changes compared to the other dependent variables. The main peak, which is responsible for sustaining the discharge, is decreased. The decrease of the ionization rate is corroborated

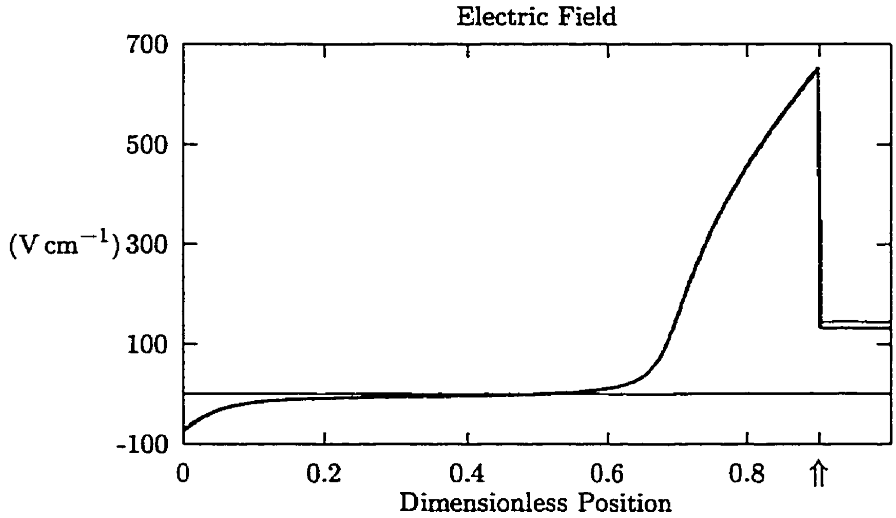

Figure 4.44: Electric field for charge accumulation on the dielectric barrier having ϵ_r=5 (⇑). Initial electric field without surface charge (solid bold line); after one period (line). For convenience, the zero-value ordinate is plotted.

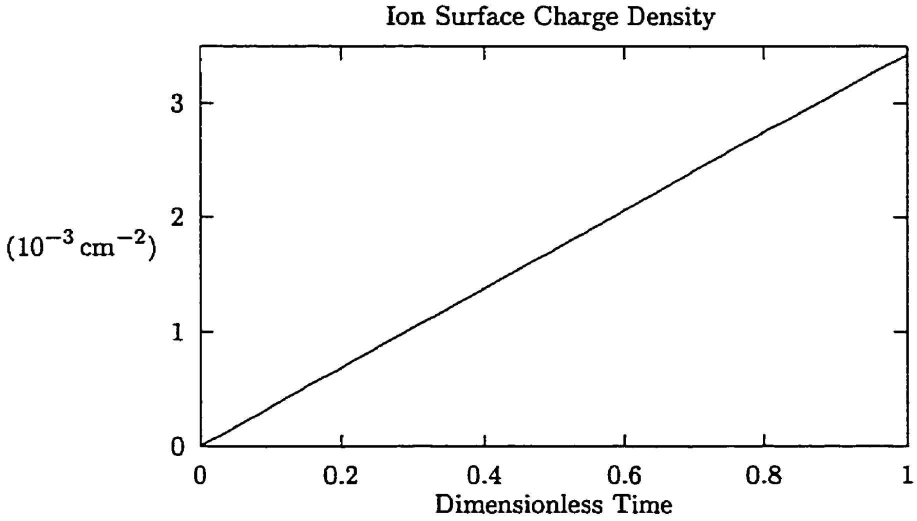

Figure 4.45: Ion surface charge accumulation on the dielectric barrier having ϵ_r=5 (⇑). The time scale is normalized with respect to the scaling period $(1/\nu)$.

with the lower electron Joule heating in the bulk of the plasma illustrated by Figure 4.47. This is significant because the charge accumulation process, which appears to be a small surface effect, actually influences important plasma sustaining terms throughout the plasma.

The ion particle flux term exhibits only very small changes in the high electric field region and practically none elsewhere, as seen in Figure 4.48. However, the electron particle flux, and consequently the total conduction current, show a uniform decrease throughout the plasma in Figure 4.49. Unlike the artificially sustained plasma, this will lead to the collapse of the discharge.

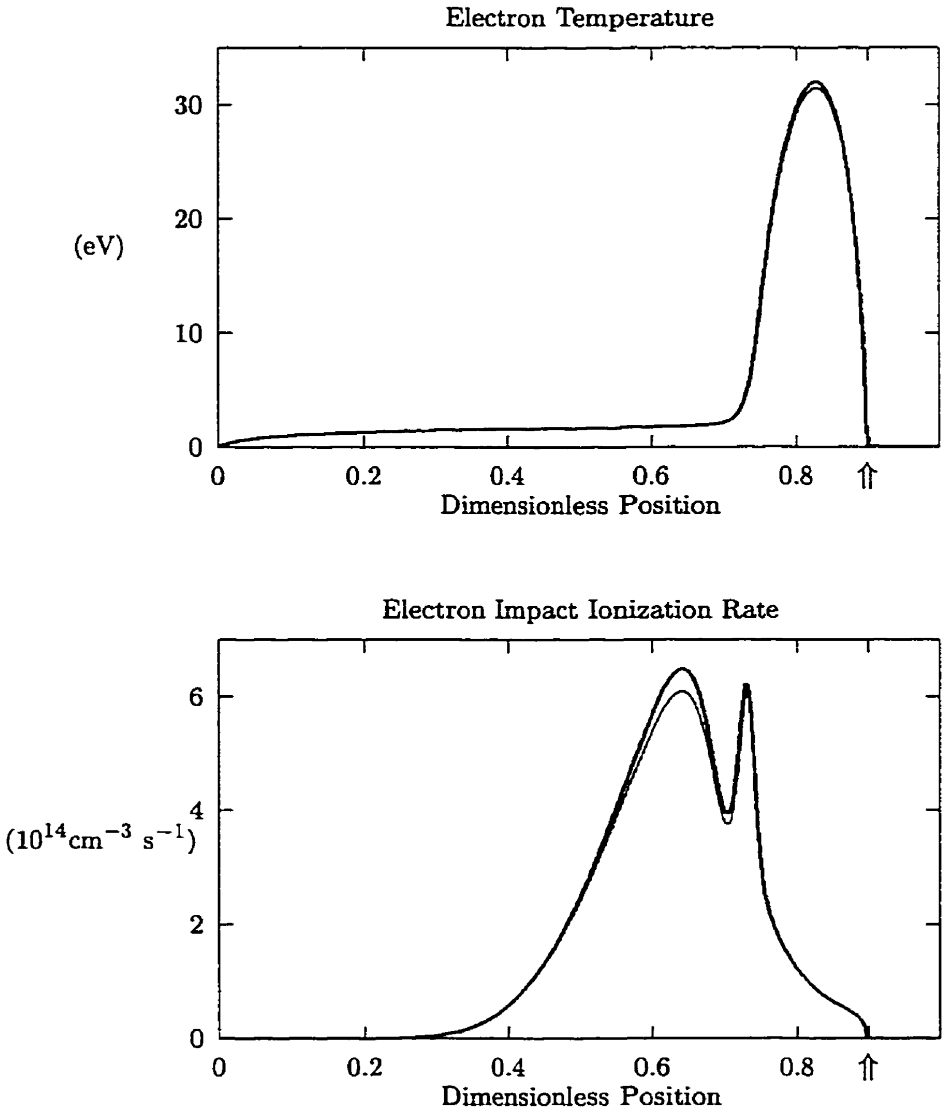

Figure 4.46: Electron temperature (top) and electron impact ionization rate (bottom) as charges accumulate on the dielectric barrier, case ϵ_r=5 (⇑). Initial distribution without surface charge (solid bold line); after one period (solid line).

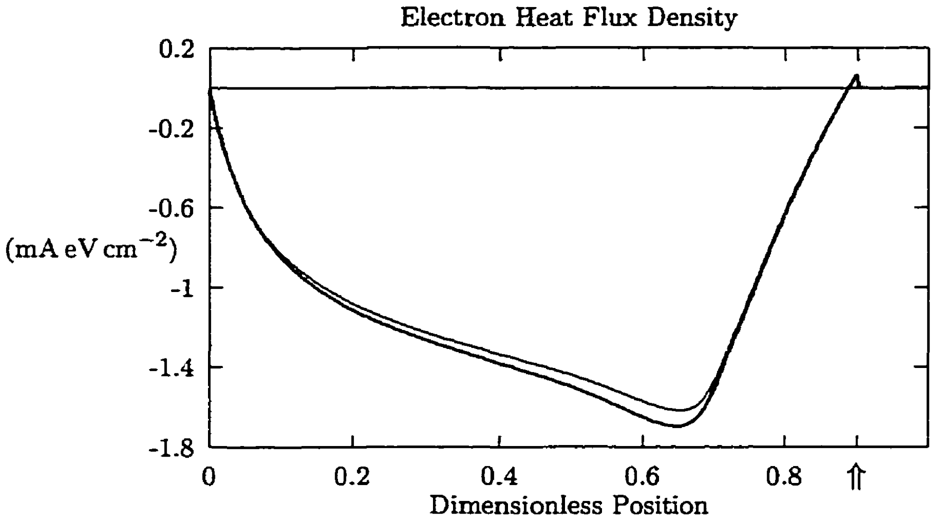

Figure 4.47: Electron heat flux density as charges accumulate on the dielectric barrier, case ϵ_r=5 (⇑). Initial distribution without surface charge (solid bold line); after one period (solid line). For convenience, the zero-value ordinate is plotted.

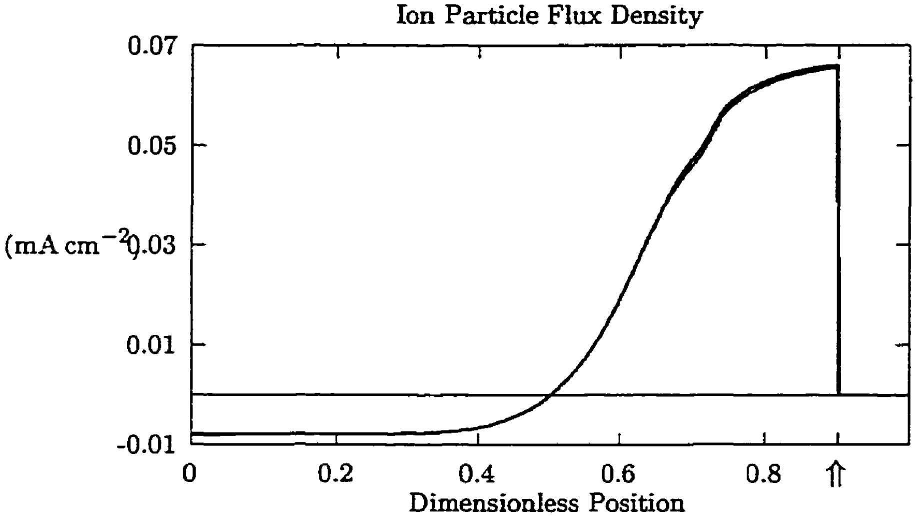

Figure 4.48: Ion flux density as charges accumulate on the dielectric barrier, case ϵ_r=5 (⥣). Initial flux density without surface charge (solid bold line); after one period (solid line). For convenience, the zero-value ordinate is plotted.

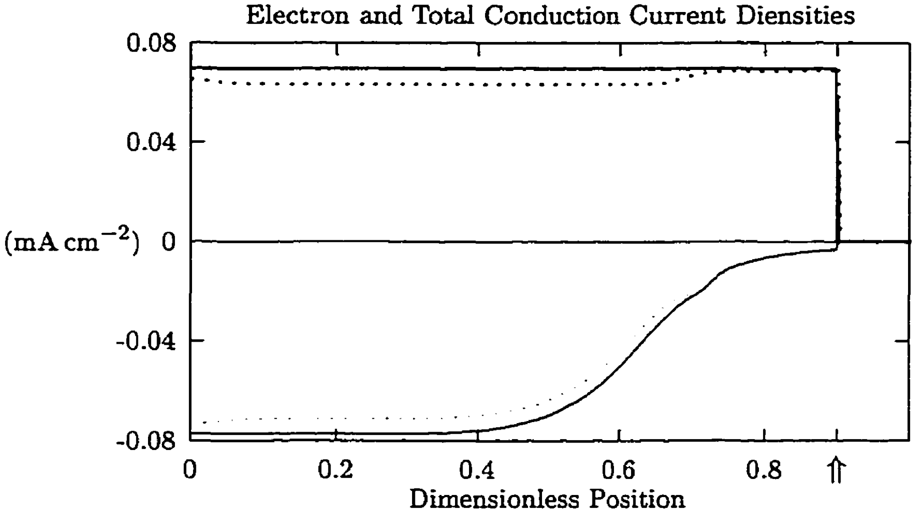

Figure 4.49: Electron and total conduction current densities as charges accumulate on the dielectric barrier, case ϵ_r=5 (⥣). Total conduction current without surface charge (solid bold line); after one period (dotted line). Electron current density without surface charge (solid line); after one period (light dotted line). For convenience, the zero-value ordinate is plotted.

4.3.4 Time-dependent discharge case

The results from simulations using time-varying applied electrode voltages with time-harmonic and pulse-waveform for the geometry having a dielectric barrier covering the cathode are presented in this section. The discharge conditions, including the applied voltages, are the same as used in section 4.2.3. The applied voltages are described in Figure 4.14.

The electric field at four times in the pulse period is given in Figure 4.50. The high field region near the dielectric barrier has increased considerably compared to an equivalent simulation without the dielectric barrier, as shown in Figure 4.16. Consequently, the region of plasma confinement is reduced. The time-modulation of the field in the plasma is greater than it was for the simulation without the barrier.

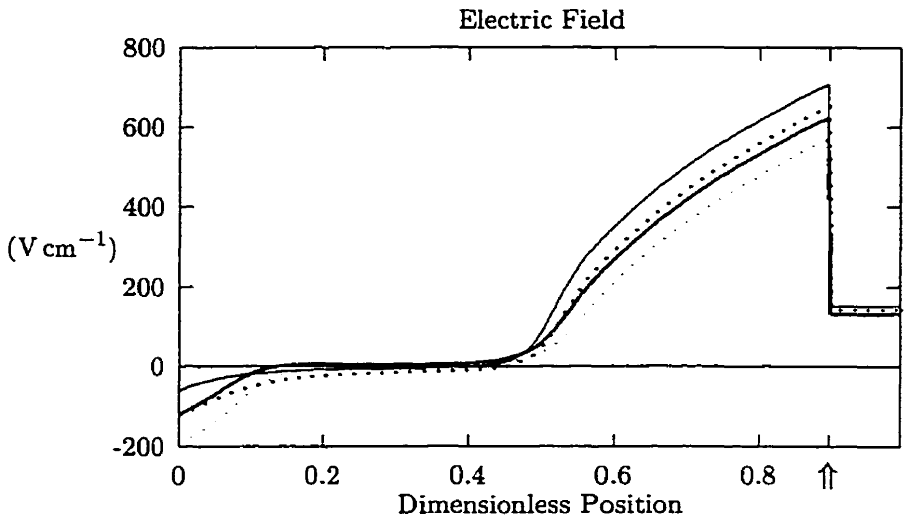

Figure 4.50: Electric field at different times in the period (T), for the case with a dielectric barrier, ϵ_r=5 (⇑). At 0.1 T (solid bold line); 0.4 T (solid line); 0.6 T (dotted line); and 0.9 T (light dotted line). Solution for the pulse-waveform case (−400 V to −600 V). For convenience, the zero-value ordinate is plotted.

This allows a greater control of the driving voltage over the inelastic reaction rates for the electron impact ionization rate as seen in Figure 4.51. Compared to the result previously obtained from the simulation without the barrier, see

Figure 4.17, the reaction rate, and its time-modulation, are relatively important throughout the plasma region.

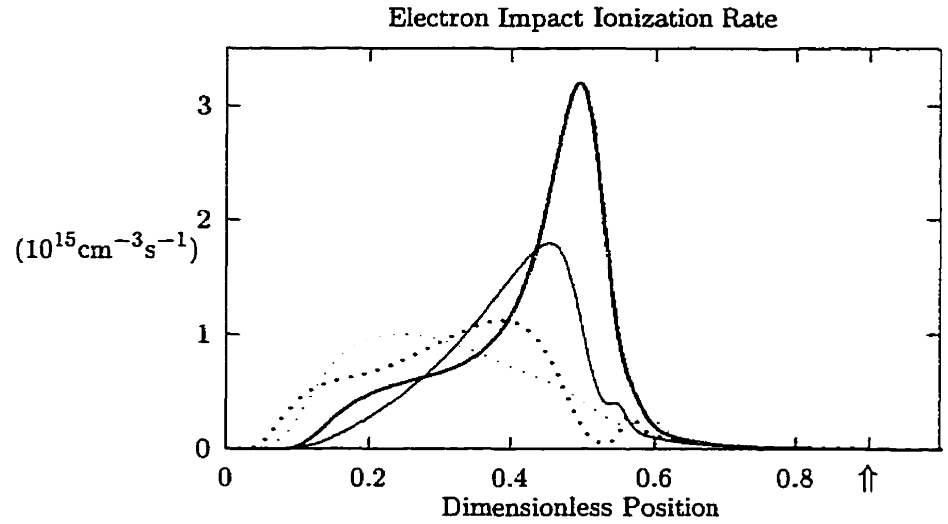

Figure 4.51: Electron impact ionization rate at different times in the period (T), for the case with a dielectric barrier, ϵ_r=5 (⥣). At 0.1 T (solid bold line); 0.4 T (solid line); 0.6 T (dotted line); and 0.9 T (light dotted line). Solution for the pulse-waveform case (−400 V to −600 V).

The electron temperature displays a much wider peak in the cathode sheath when a dielectric barrier is present in the discharge space, as seen in Figure 4.52, when compared with Figure 4.16. This is consistent with the electric field distribution. Note that the reaction rate is not important in the high field region, indicating a low electron density distribution. However, secondary electron emissions due to ion impact on the dielectric barrier are considered, and those electrons will surely not have a Maxwellian distribution function. It would not be appropriate to use constant kinematic coefficients for the electrons. Instead, coefficients that are a function of temperature should be considered. The coefficients can be obtained by solving the Boltzmann transport equation for various values of the reduced field, as was done for the ionization rate.

Period-averaged quantities are computed to compare results from simulations using both time-harmonic and pulse-waveform applied voltages. All

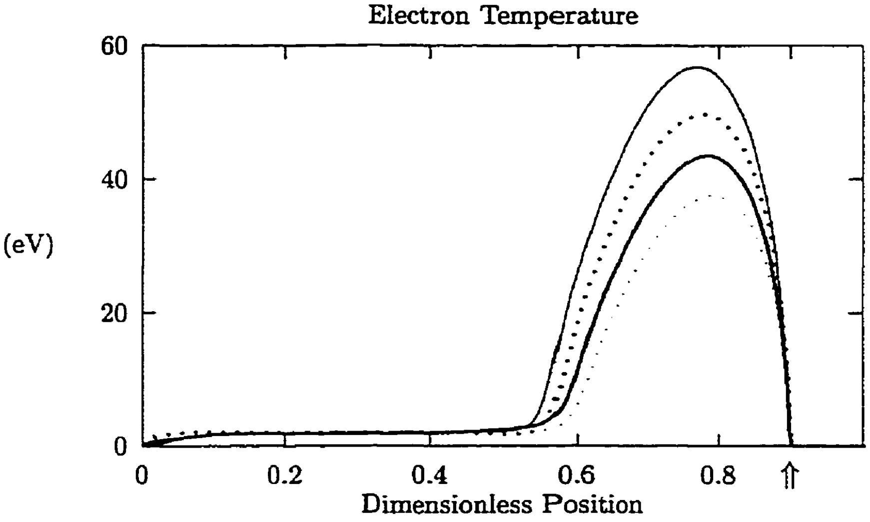

Figure 4.52: Electron temperature at different times in the period (T), for the case with a dielectric barrier, ϵ_r=5 (⇑). At 0.1 T (solid bold line); 0.4 T (solid line); 0.6 T (dotted line); and 0.9 T (light dotted line). Solution for the pulse-waveform case (−400 V to −600 V).

dependent variables, as shown in Figure 4.53 for the electric field and the electron temperature, exhibit little change due to the different applied voltage waveforms. This was also the case for simulations without the dielectric barrier.

However, a much higher period-integrated ionization rate was obtained from the pulse-waveform simulation, compared to the time-harmonic applied voltages as shown in Figure 4.54. Such a difference was not observed for simulations without the dielectric barrier.

The importance of this result is enhanced by the fact that the total conduction current is relatively unaffected by the shape of the applied voltage as shown in Figure 4.55, while the electron Joule heating is more important in the plasma bulk for the simulation using the pulse-waveform applied voltages, see Figure 4.56. Therefore, we obtain a greater reaction rate for an equivalent conduction current, in a period-averaged sense, for discharges driven by pulse shape applied voltages than for time-harmonic applied voltages.

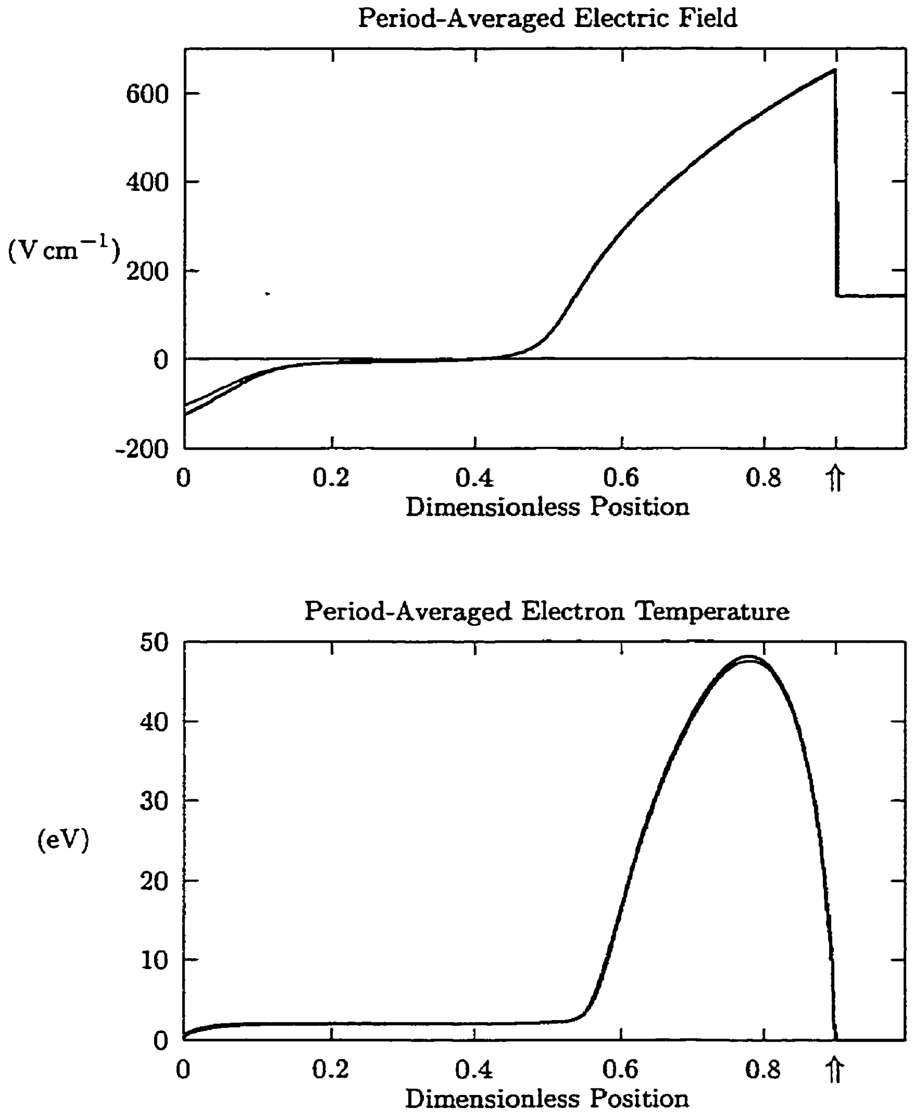

Figure 4.53: Period-averaged electric field (top) and electron temperature (bottom), for geometry with a dielectric barrier, ϵ_r=5 (⇑). Pulse-waveform (solid bold line) and time-harmonic (solid line) cases. Solutions with an applied voltage from −400 V to −600 V. For convenience, the zero-value ordinate is plotted in the upper plot.

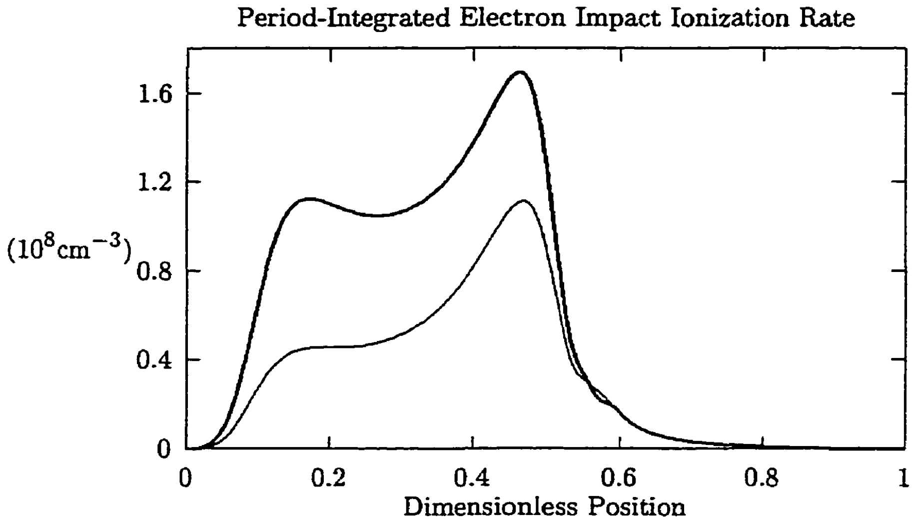

Period-Integrated Electron Impact Ionization Rate

Figure 4.54: Period-integrated electron impact ionization rate, for geometry with a dielectric barrier, ϵ_r=5 ($\Uparrow$). Pulse-waveform (solid bold line) and time-harmonic (solid line) cases. Solutions for cases with an applied voltage of −400 V to −600 V.

This result may be interpreted in the following manner. The inelastic electron impact collisions are characterized by threshold-like processes which are dependent on the electrons' kinetic energy. The discharge obtained using an applied voltage of pulse-waveforms with flat tops brings the electrons' kinetic energy to a level favoring specific inelastic processes for a period of time longer than a similar discharge obtained with a time-harmonic applied voltage. In this manner it is possible to select the right combination of dielectric barrier (in terms of material permittivity and thickness) and shape of the applied voltage (pulse width, pulse hight, and repetition rate) in order to favor specific reaction rates.

We will now study the discharge characteristics as functions of the voltage applied across the electrodes for pulse-waveform case.

The period-averaged electric field and electron temperature obtained from simulations using pulse-waveforms from −300 V to −500 V and from −400 V to −600 V are compared in Figure 4.57.

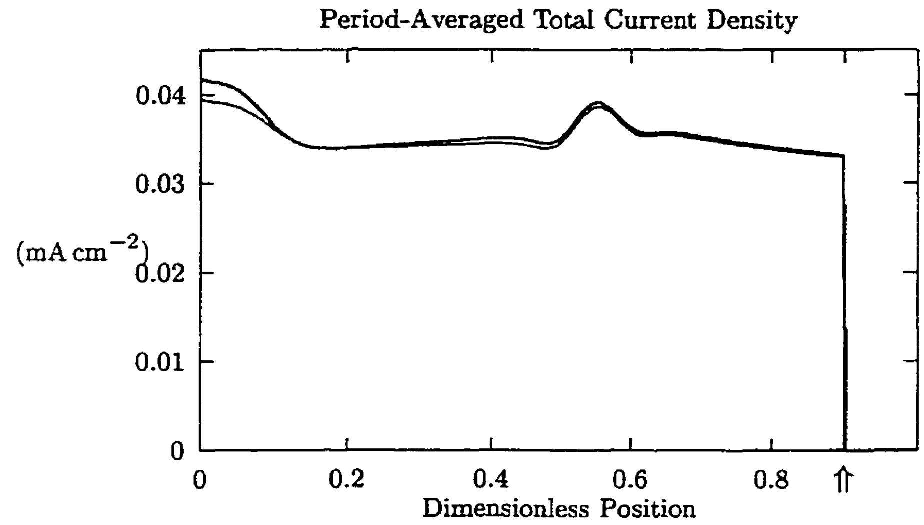

Figure 4.55: Period-averaged total current density, for geometry with a dielectric barrier, ϵ_r=5 (⥣). Pulse-waveform (solid bold line) and time-harmonic (solid line) cases. Solutions for cases with an applied voltage of −400 V to −600 V.

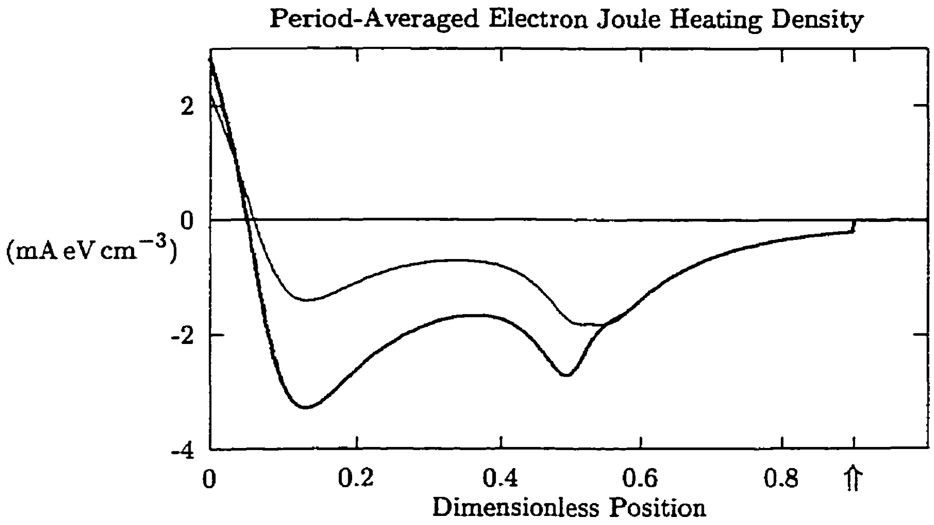

Figure 4.56: Period-averaged electron Joule heating density, for geometry with a dielectric barrier, ϵ_r=5 (⥣). Pulse-waveform (solid bold line) and time-harmonic (solid line) cases. Solutions for cases with an applied voltage of −400 V to −600 V. For convenience, the zero-value ordinate is plotted.

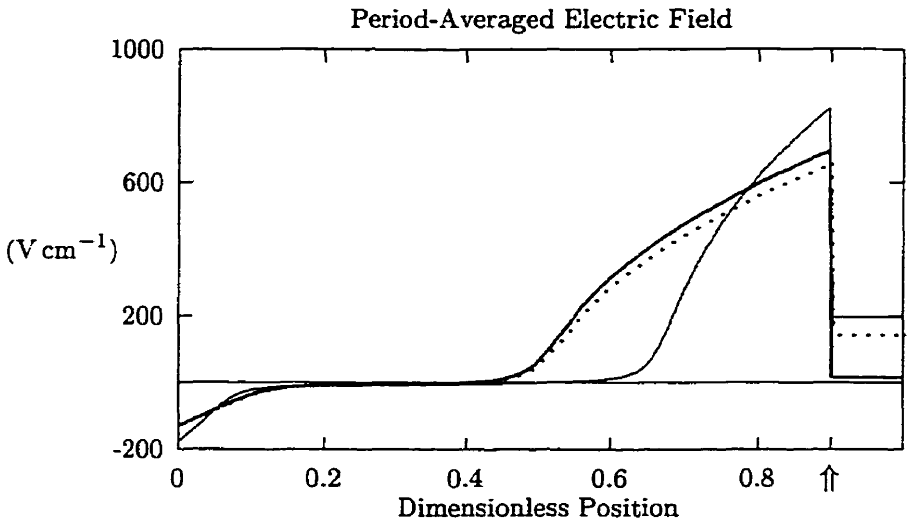

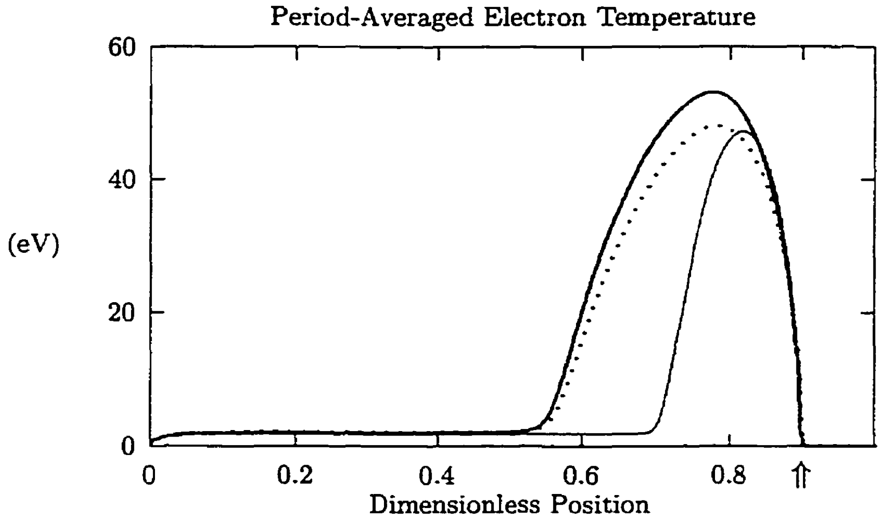

Figure 4.57: Period-averaged electric field (top) and electron temperature (bottom), for geometry with a dielectric barrier (⇑). The applied voltage is a pulse-waveform from −400 V to −600 V and ϵ_r=50 (solid bold line); ϵ_r=5 (dotted line). Pulse-waveform from −300 V to −500 V and ϵ_r=5 (solid line). For convenience, the zero-value ordinate is plotted in the upper plot.

The results are more significantly different than those obtained without a dielectric barrier, as shown in Figure 4.20, in two respects. First, the electron temperature peak is higher for the case with higher applied voltage, as obtained when no dielectric barrier is present. However, the maximum electric field is smaller for the case with higher applied voltage. This shows clearly that the electrons are not in thermal equilibrium with the electric field, not even locally. Second, the effect of a higher applied voltage in the case of a dielectric barrier discharge is to increase the thickness of the high electric field region (cathode sheath), while for a discharge without the dielectric barrier, the effect was only to change the maximum values of the electric field and the electron temperature, and not the cathode sheath thickness.

The consequences of these results are important. One can design the electrodes in order to maximize the rate of reactions while minimizing the electron flux density, and consequently, the conduction current. Compare the period-integrated ionization rates obtained from the simulations with different nominal voltages, shown in Figure 4.58, and the corresponding total conduction current shown in Figure 4.59.

This is the most important result of this thesis; it shows the regulating effect of the dielectric barrier, and also the ability to increase the efficiency of the plasma chemistry reactor by selecting the proper combination of the dielectric barrier and applied voltage characteristics.

Before we close this section, it is of interest to compare the period-averaged electron and ion Joule heating term obtained for a discharge with different nominal voltages, as shown in Figure 4.60. The electron Joule effect is, in general, relatively unchanged when different nominal voltage values are used. However the ion Joule heating exhibits, contrary to what might be expected, a considerably lower heating in the cathode sheath for the discharge with the higher applied voltage. This is an important factor to consider in the design of electrodes having a dielectric barrier. The thermal stress experienced by the barrier due to ion bombardment often causes the barrier to break down.

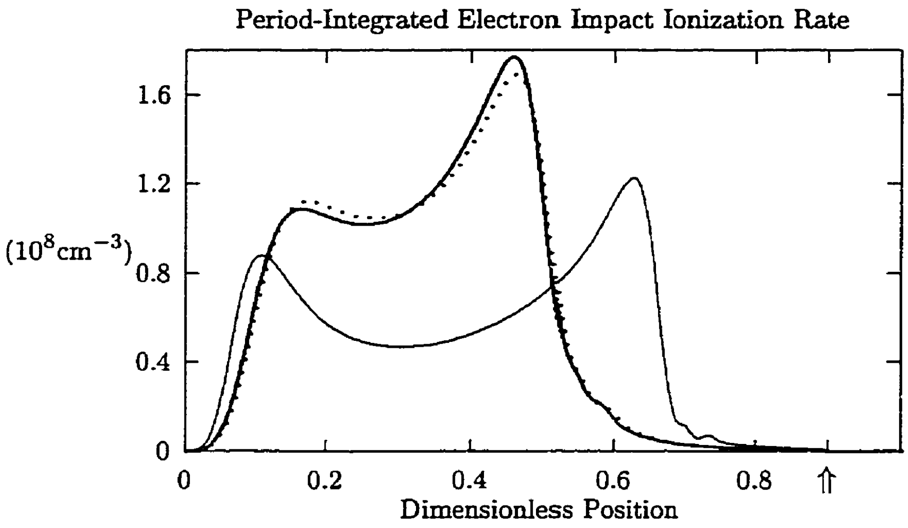

Figure 4.58: Period-integrated electron impact ionization rate, for geometry with a dielectric barrier (⇑). The applied voltage is a pulse-waveform from −400 V to −600 V and ϵ_r=50 (solid bold line); ϵ_r=5 (dotted line). Pulse-waveform from −300 V to −500 V and ϵ_r=5 (solid line).

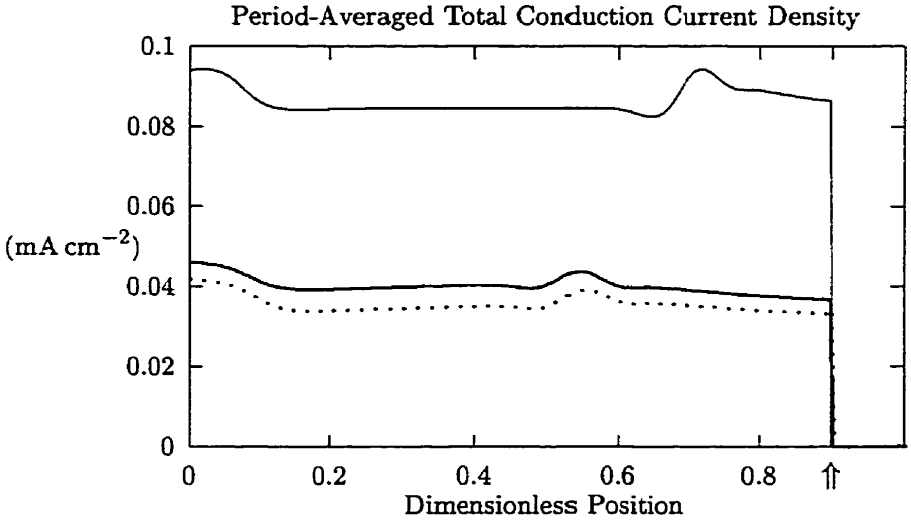

Figure 4.59: Period-averaged total conduction current density, for geometry with a dielectric barrier (⇑). The applied voltage is a pulse-waveform from −400 V to −600 V and ϵ_r=50 (solid bold line); ϵ_r=5 (dotted line). Pulse-waveform from −300 V to −500 V and ϵ_r=5 (solid line).

Therefore, the ability to attain higher reaction rates with lower thermal stress for the dielectric barrier is undoubtedly a desirable feature.

To close this chapter, we show that the two-fluid model incorporating a dielectric barrier in the discharge space preserves the divergence-less property of the total current.

The total conduction and displacement currents at four times in the period are shown in Figure 4.61. Note that the displacement current is more important for dielectric barrier discharge than it was for discharge without dielectric. Indeed, the displacement current exists throughout the plasma, indicating a more important modulation of the plasma due to the time variation of the applied voltage.

The total current, shown in Figure 4.62, is conserved at all times in the discharge period.

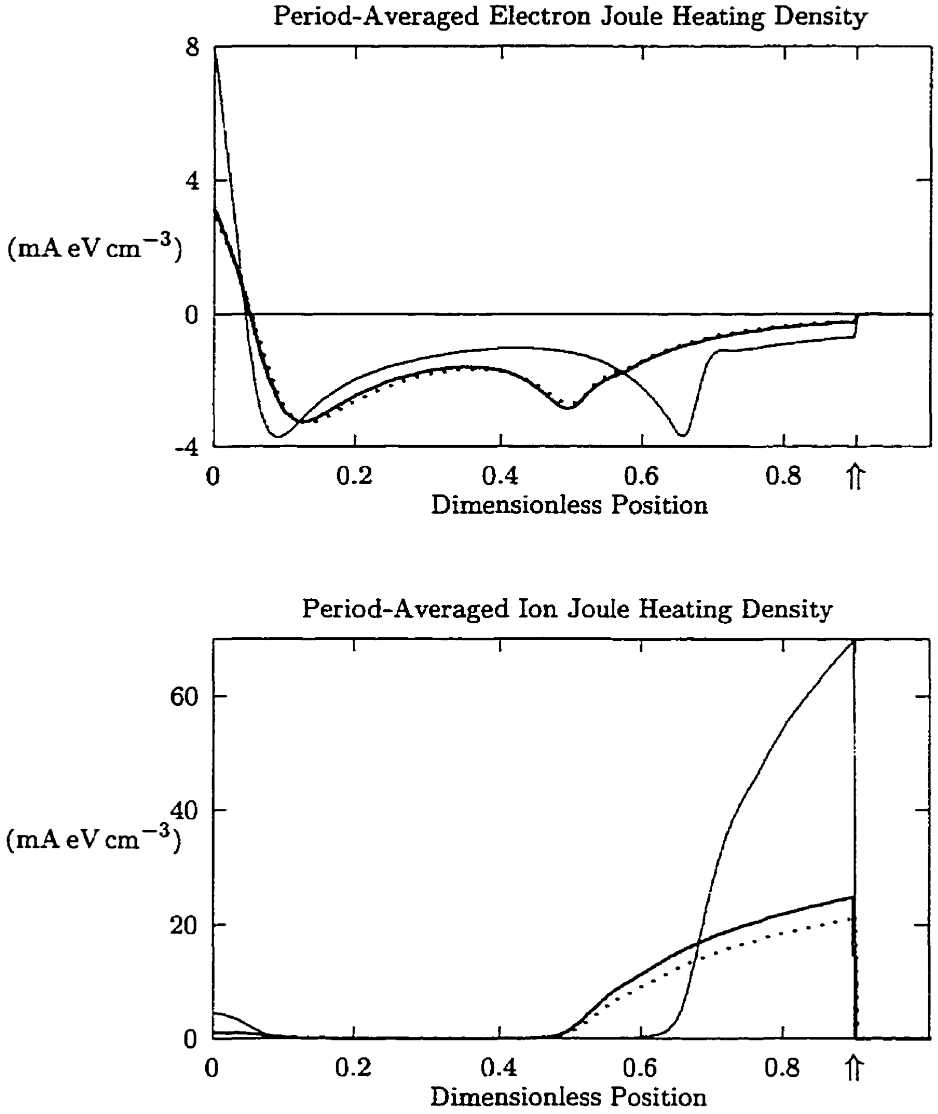
Period-Averaged Electron Joule Heating Density

Period-Averaged Ion Joule Heating Density

Figure 4.60: Period-averaged electron (top) and ion (bottom) Joule heating density, for geometry with a dielectric barrier (⇑). The applied voltage is a pulse-waveform from −400 V to −600 V and ϵ_r=50 (solid bold line); ϵ_r=5 (dotted line). Pulse-waveform from −300 V to −500 V and ϵ_r=5 (solid line). For convenience, the zero-value ordinate is plotted in the upper plot.

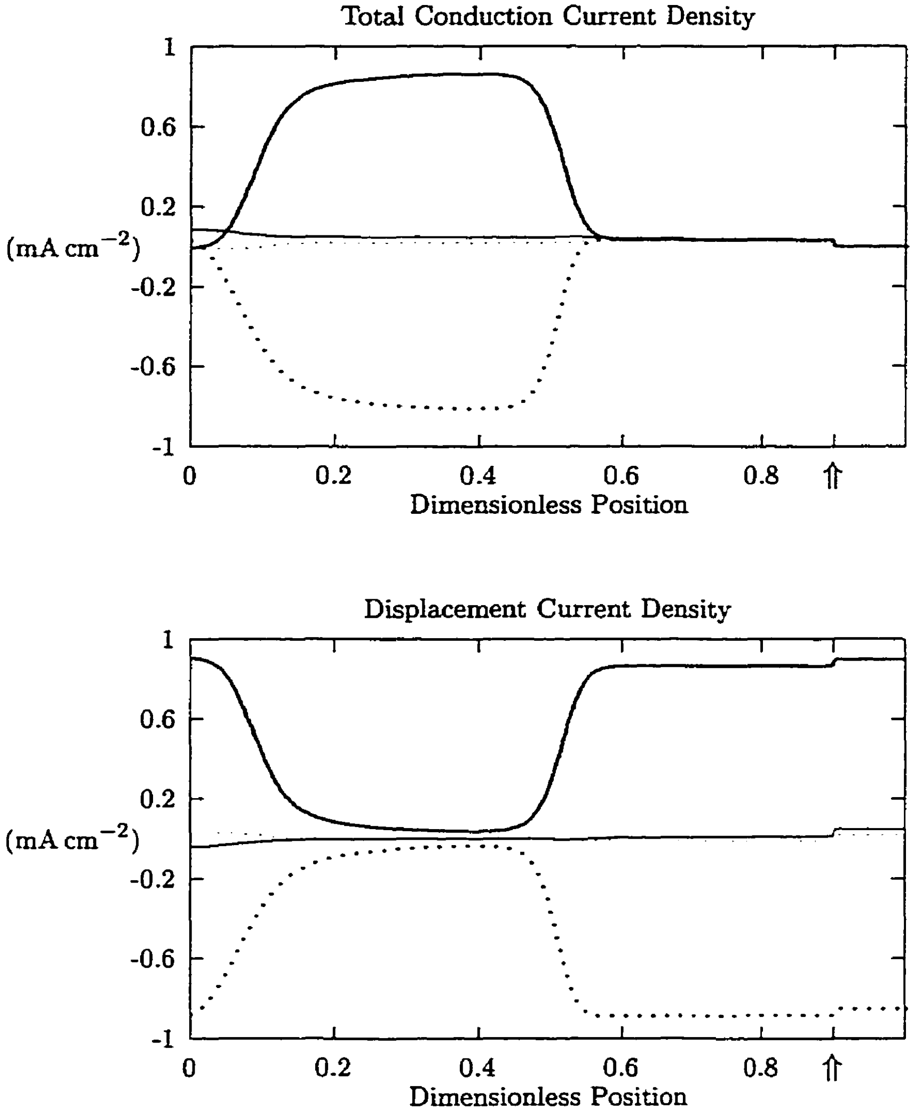

Figure 4.61: Total conduction (top) and displacement (bottom) current densities at different times in the period (T) for the case with a dielectric barrier, ϵ_r=5 (⇑). At 0.1 T (solid bold line); 0.4 T (solid line); 0.6 T (dotted line); and 0.9 T (light dotted line). Solution for pulse-waveform case (−400 V to −600 V).

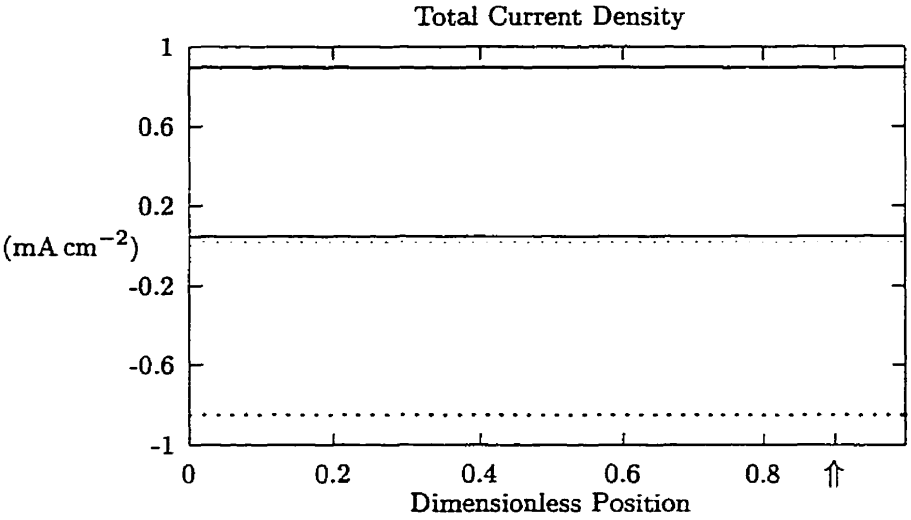

Figure 4.62: Total current density (total conduction plus displacement) at different times in the period (T) for the case with a dielectric barrier, ϵ_r=5 (⇑). At 0.1 T (solid bold line); 0.4 T (solid line); 0.6 T (dotted line); and 0.9 T (light dotted line). Solution for pulse-waveform case (−400 V to −600 V).

Chapter 5

Conclusion and summary

In this thesis we reported on the development of a computational model for predicting the physical structure of the gas discharge obtained between two electrodes, when one is covered with a dielectric material. The model represents the distribution of the electron and ion particle densities, electron energy, and electric field strength. This is a self-consistent numerical model, in which the dielectric properties of the dielectric material are included and the geometry of the electrodes is taken into account, thus coupling the charged-particle transport to the electric field.

New boundary conditions were developed for the electron gas at the anode; results presented in section 4.2.2 indicate that the common boundary conditions frequently used in the literature give solutions with non-physical behavior. The new boundary conditions give solutions with the expected physical behavior.

We developed new universal matrices for the finite element method with the ability to construct complex finite element matrices, replacing integrals by matrix products, in a consistent and uniform manner independent of element shape, dimension, and order.

Validation of the mathematical model was presented in section 4.1 where we reproduced the results of Wardlaw and Cohen [52] for the continuum analysis of the photoionization chamber.

Solutions for DC and time-varying applied voltages across the electrodes, using pulse-waveform and time-harmonic excitations, for the geometry with and without a dielectric barrier, have been presented.

In sections 4.3.2 and 4.3.3, we showed the regulating effect of the dielectric barrier by a surface charge accumulation mechanism, for discharge with a constant applied voltage assuming a static temperature for the electron gas, and for the full self-consistent model, respectively.

In section 4.3.4, simulations of a dielectric barrier discharge driven by pulse-waveform voltages were compared with simulations of discharge driven by time-harmonic applied voltages. The results showed very similar period-averaged electric fields, electron temperature profiles, charged particle densities, and total conduction current densities. However, a much higher period-integrated ionization rate was obtained from the pulse-waveform simulations, compared to time-harmonic applied voltage cases. Therefore, we obtain a greater reaction rate for an equivalent conduction current, in a period-averaged sense, for discharges driven by pulse-waveform applied voltages, than for time-harmonic excitations. Such a difference was not observed for simulations without the dielectric barrier.

The results indicate that the presence of the dielectric barrier not only plays a role in the regulation of the discharge by limiting the conduction current, but also by increasing the plasma response to the applied voltage. As a consequence, one can increase the energy efficiency of a plasma reactor by selecting the proper combination of a dielectric barrier and the applied voltage characteristics.

The developed mathematical model also represents the electric and thermal stresses experienced by the dielectric barrier, which are two important limiting factors in the design of a particular reactor. No other model in the literature provides such design specific information.

This physical model may be integrated into a complete plasma induced chemistry reactor model, which would be very attractive for industrial plasma chemistry applications. An example of the structure of such a model is shown in Figure 5.1. It relies on a Boltzmann code module for computing the transport coefficients, electron kinetic energy, and electron impact reaction rates from the cross section data, using the computed electron distribution function for a range of reduced electric fields. From this set of data one could relate, in the form of an approximate analytical expression, the transport coefficients and the electron impact reaction rates to the electron temperature. These relations would then be used in the plasma fluid model to obtain the space-time distribution of the radical production rates from the electron number density and temperature distribution. In this module many chemical species are not discriminated and are all considered to form a single species. From the radical production rates, the chemistry model would then determine the contaminant destruction rates and the composition of the gas exiting the reactor.

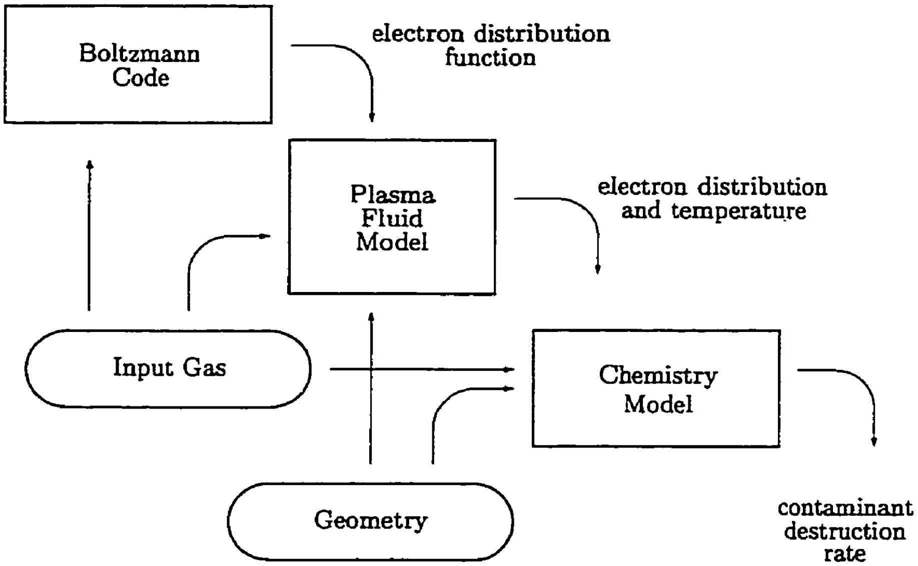

Figure 5.1: Inclusion of the developed physical model into a plasma chemistry model adding two modules, a Boltzmann code and a chemistry model.

This three module decomposition of the plasma reactor permits processes having very different space and time characteristics to be modeled separately. Such a decomposition of the non-equilibrium kinetics in RF discharge were used by Capriati, Boeuf, and Capitelli [25]. Sommerer and Kushner [47] developed a similar model in which they used a Monte Carlo simulation based on the field distribution from the fluid model solution rather than using a Boltzmann code. Recently, Mantzaris, Gogolides, and Boudouvis [100] developed a consistent plasma chemistry model using a similar modular approach assuming the electrons to be in local thermal equilibrium with the electric field. None of these sophisticated models consider the presence of a dielectric barrier in the discharge space.

Bibliography

[1] D. B. Graves. Plasma processing. *IEEE Trans. Plasma Sc.*, 22:31–42, 1994.

[2] Spectrum, February 1996.

[3] Spectrum, September 1996.

[4] B. Eliasson and U. Kogelschatz. Nonequilibrium volume plasma chemical processing. *IEEE Trans. Plasma Sc.*, 19:1063–1077, 1991.

[5] J. J. Lowke and R. Morrow. Theoretical analysis of removal of oxides of sulfur and nitrogen in pulsed operation of electrostatic precipitators. *IEEE Trans. Plasma Sc.*, 23:661–671, 1995.

[6] M. B. Chang, M. J. Kushner, and M. J. Rood. Removal of SO_2 and simultaneous removal of SO_2 and NO from simulated flue gas streams using dielectric barrier discharge plasmas. *Plasma Chem. Plasma Proc.*, 12:565–580, 1992.

[7] E. L. Neau. Environmental and industrial applications of pulsed power systems. *IEEE Trans. Plasma Sc.*, 22:2–10, 1994.

[8] *Proceedings of the NATO Advanced Research Workshop on Non-Thermal Plasma Techniques for Pollution Control*, Sept. 21–25, 1992 1993.

[9] Workshop on the treatment of gaseous emissions via plasma technology. NIST, Gaithersburg, March 1995.

[10] E. Kuffel and M. Abdullah. *High-voltage engineering.* Pergamon Press, second edition edition, 1970.

[11] B. Eliasson and U. Kogelschatz. Modeling and applications of silent discharge plasmas. *IEEE Trans. Plasma Sc.*, 19:309–323, 1991.

[12] A. C. Gentile and M. J. Kushner. Reaction chemistry and optimization of plasma remediation of N_xO_y from gas streams. *J. Appl. Phys.*, 78:2074–2085, 1995.

[13] J. Li, W. Sun, B. Pashaie, and S. K. Dhali. Streamer discharge simulation in flue gas. *IEEE Trans. Plasma Sc.*, 23:672–678, 1995.

[14] J.-M. Guo and C.-H. Wu. Two-dimensional nonequilibrium fluid models for streamers. *IEEE Trans. Plasma Sc.*, 21:684–695, 1993.

[15] G. V. Naidis. On streamer interaction in a pulsed positive corona discharge. *J. Phys. D: Appl. Phys.*, 29:779–782, 1996.

[16] J. P. Verboncoeur, G. J. Parker, B. M. Penetrante, and W. L. Morgan. Comparison of collision rates in particle-in-cell, Monte Carlo, and Boltzmann codes. *J. Appl. Phys.*, 80:1299–1303, 1996.

[17] S. D. Rockwood. Elastic and inelastic cross sections for electron-hg scattering from Hg transport data. *Phys. Rev. A*, 8:2348–2358, 1973.

[18] F. Esposito, G. Colonna, S. Longo, and M. Capitelli. Monte Carlo global sensitivity analysis of Boltzmann equation for electron kinetics in H_2 discharges. *Plasma Chem. Plasma Proc.*, 16:1–16, 1996.

[19] R. M. Thomson, K. Smith, and A. R. Davie. BOLTZ: A code to solve the transport equation for electron distributions and then calculate transport coefficients and vibrational excitation rates in gases with applied fields. *Comp. Phys. Comm.*, 11:369–383, 1976.

[20] W. L. Morgan and B. M. Penetrante. ELENDIF: A time-dependent boltzmann solver for partially ionized plasmas. *Comp. Phys. Comm.*, 58:127–152, 1990.

[21] V. A. Feoktistov, A. M. Popov, O. B. Popovicheva, A. T. Rakhimov, T. V. Rakhimova, and E. A. Volkova. RF discharge modeling considering time dependence and spatial nonlocality of the electron energy spectrum. *IEEE Trans. Plasma Sc.*, 19:163–169, 1991.

[22] C. M. Ferreira, L. L. Alves, M. Pinheiro, and A. B. Sa. Modeling of low-pressure microwave discharges in Ar, He, and O_2: similarity laws for the maintenance field and mean power transfer. *IEEE Trans. Plasma Sc.*, 19:229–239, 1991.

[23] M. Capitelli, G. Colonna, K. Hassouni, and A. Gicquel. Electron energy distribution functions and rate and transport coefficients of $H_2/H/CH_4$ reactive plasmas for diamond film deposition. *Plasma Chem. Plasma Proc.*, 16:153–171, 1996.

[24] G. Capriati, G. Colonna, and C. Gorse. A parametric study of electron energy distribution functions and rate transport coefficients in nonequilibrium helium plasmas. *Plasma Chem. Plasma Proc.*, 12:237–260, 1992.

[25] G. Capriati, J. P. Boeuf, and M. Capitelli. A self-consistent one-dimensional model for he nonequilibrium kinetics in RF discharges. *Plasma Chem. Plasma Proc.*, 13:499–519, 1993.

[26] N. L. Aleksandrov and I. V. Kochetov. Electron rate coefficients in gases under non-uniform field and electron density conditions. *J. Phys. D: Appl. Phys.*, 29:1476–1483, 1996.

[27] M. J. Kushner. A kinetic study of the plasma-etching process. i. a model for the etching of Si and SiO_2 in C_nF_m/H_2 and C_nF_m/H_2 plasmas. *J. Appl. Phys.*, 53:2923–2938, 1982.

[28] B. F. Gordiets, C. M. Ferreira, V. L. Guerra, J. M. A. Loureiro, J. Nahorny, D. Pagnon, M. Touzeau, and M. Vialle. Kinetic model of a low-pressure N_2–O_2 flowing glow discharge. *IEEE Trans Plasma Sc.*, 23:750–768, 1995.

[29] A. C. Gentile and M. J. Kushner. Plasma remediation of perchloroethylene in humid gas streams. *J. Appl. Phys.*, 78:2977–2980, 1995.

[30] A. V. Phelps and B. M. Jelenkovie. Simplified models of electron excitation and ionization at very high E/N. *Phys Rev. A*, 36:5327–5336, 1987.

[31] S. Shankar and K. F. Jensen. Analysis of spherical harmonic expansion approximations for glow discharges. *IEEE Trans. Plasma Sc.*, 23:780–787, 1995.

[32] J. Mathews and R. L. Walker. *Mathematical methods of physics.* Benjamin/Cummings Publishing Co., second edition edition, 1970.

[33] D. Loffhagen, R. Winkler, and G. L. Braglia. Two-term and multi-term approximation of the nonstationary electron velocity distribution in an electric field in a gas. *Plasma Chem. Plasma Proc.*, 16:287–299, 1996.

[34] T. J. Sommerer, W. N. G. Hitchon, and J. E. Lawler. Self-consistent kinetic model of the cathode fall of a glow discharge. *Phys. Rev. A*, 39:6356–6366, 1989.

[35] J. B. Adams. Solution of master and fokker-planck equations by propagator methods, applied to Au/NaCl thin film nucleation. *J. Comp. Phys.*, 76:159–175, 1988.

[36] T. J. Sommerer, W. N. G. Hitchon, and J. E. Lawler. Electron heating mechanism in helium RF glow discharge: A self-consistent kinetic calculation. *Phys. Rev. Lett.*, 63:2361–2364, 1989.

[37] D. Uhrlandt and R. Winkler. Radially inhomogeneous electron kinetics in the DC column plasma. *J. Phys. D: Appl. Phys.*, 29:115–120, 1996.

[38] J. P. Boeuf and E. Marode. A Monte Carlo analysis of an electron swarm in a non-uniform field: the cathode region of a glow discharge in helium. *J. Phys. D: Appl. Phys.*, 15:2169–2187, 1982.

[39] A. Tran Ngoc, E. Marode, and P. C. Johnson. Monte Carlo simulation of electrons within the cathode fall of a glow discharge in helium. *J. Phys. D: Appl. Phys.*, 10:2317–2321, 1977.

[40] J. W. Eastwood. Particle simulation methods in plasma physics. *Comp. Phys. Comm.*, 43:89–106, 1986.

[41] C. K. Birdsall. Particle-in-cell charged-particle simulations, plus Monte Carlo collisions with neutral atoms, PIC-MCC. *IEEE Trans. Plasma Sc.*, 19:65–85, 1991.

[42] R. W. Hockney and J. W. Eastwood. *Computer simulation using particles.* Adam Hilger, 1989.

[43] M. J. Kushner. Monte-Carlo simulation of electron properties in RF parallel plate capacitively coupled discharge. *J. Appl. Phys.*, 54:4958–4965, 1983.

[44] D. Vender and R. W. Boswell. Numerical modeling of low-pressure RF plasmas. *IEEE Trans. Plasma Sc.*, 18:725–732, 1990.

[45] R. W. Boswell and D. Vender. Simulation of pulsed electropositive and electronegative plasmas. *IEEE Trans. Plasma Sc.*, 19:141–143, 1991.

[46] M. Surendra and D. B. Graves. Particle simulations of radio-frequency glow discharge. *IEEE Trans. Plasma Sc.*, 19:144–157, 1991.

[47] T. J. Sommerer and M. J. Kushner. Numerical investigation of the kinetics and chemistry of RF discharge plasma sustained in He, N_2, O_2, He/N_2/O_2, He/SiH_4/NH_3 using a Monte Carlo-fluid hybrid model. *J. Appl. Phys.*, 71:1654–1673, 1992.

[48] C. H. Wu, C. Li, J. H. Tsai, and F. F. Young. Solving the boltzmann equation in a 2-d-configuration and 2-d-velocity space for capacitively coupled RF discharges. *IEEE Trans. Plasma Sc.*, 23:650–660, 1995.

[49] G. Schaefer and P. Hui. The Monte Carlo flux method. *J. Comp. Phys.*, 89:1–30, 1990.

[50] A. L. Ward. Effect of space charge in cold-cathode gas discharges. *Phys. Rev.*, 112:1852–1857, 1958.

[51] A. L. Ward. Calculations of cathode-fall characteristics. *J. Appl. Phys.*, 33:2789–2794, 1962.

[52] A. B. Wardlaw and I. M. Cohen. Continuum analysis of the photoionization chamber in the transition from low to high rate of ionization. *Phys. Fluids*, 16:637–650, 1973.

[53] S. T. Pai, X. M. Guo, and T. D. Zhou. Closed form analytic solutions describing glow discharge plasma. *Phys. Plasmas*, 3:3842–3852, 1996.

[54] P. M. Chung. Weakly ionized nonequilibrium viscous shock-layer and electrostatic probe characteristics. *AIAA J.*, 3:817–825, 1965.

[55] P. M. Chung. Near-surface electron temperature of weakly ionized plasma according to kinetic theory. *Phys. of Fluids*, 12(8):1623–1634, 1969.

[56] N. W. Albright and D. A. Tidman. Ionizing potential waves and high-voltage breakdown streamers. *Phys. of Fluids*, 15:86–90, 1972.

[57] R. Klingbeil, D. A. Tidman, and R. F. Fernsler. Ionizing gas breakdown in strong electric fields. *Phys. Fluids*, 15:1969–1973, 1972.

[58] I. Abbas and P. Bayle. A critical analysis of ionizing wave propagation mechanism in breakdown. *J. Phys. D: Appl. Phys.*, 13:1055–1068, 1980.

[59] P. Bayle and B. Cornebois. Propagation of ionizing shock wave in electrical breakdown. *Phys. Rev. A*, 31:1046–1058, 1985.

[60] J. P. Novak and R. Bartnikas. Density profiles, electric field and energy dissipation in a short gap breakdown: a two-dimensional model. *J. Phys. D: Appl. Phys.*, 21:896–903, 1988.

[61] J. P. Novak and R. Bartnikas. Breakdown model of a short plane-parallel gap. *J. Appl. Phys.*, 62:3605–3615, 1987.

[62] J. P. Novak and R. Bartnikas. Theoretical and experimental investigations on the process of high-pressure discharge development. *IEEE Trans. Plasma Sc.*, 19:95–101, 1991.

[63] J. P. Boeuf. Numerical model of RF glow discharge. *Phys. Rev. A*, 36:2782–2792, 1987.

[64] D. B. Graves and K. F. Jensen. A continuum model of DC and RF discharge. *IEEE Trans. Plasma Sc.*, PS-14:78–91, 1986.

[65] S. K. Park and D. J. Economou. Parametric study of a radio-frequency glow discharge using a continuum model. *J. Appl. Phys.*, 68:4888–4890, 1990.

[66] D. B. Graves. Fluid model simulations of a 13.56-MHz RF discharge: Time and space dependence of rates of electron impact excitation. *J. Appl. Phys.*, 62:88–94, 1987.

[67] M. H. Wilcoxson and V. I. Manousiouthakis. Well-posedness of continuum models for weakly ionized plasma. *IEEE Trans. on Plasma Sc.*, 21:213–222, 1993.

[68] M. S. Barnes, T. J. Cotler, and M. E. Elta. A staggered-mesh finite-difference numerical method for solving the transport equations in low pressure RF glow discharges. *J. Comp. Phys.*, 77:53–72, 1988.

[69] M. Meyyappan and J. P. Kreskovsky. Glow discharge simulation through solutions to the moments of the boltzmann transport equation. *J. Appl. Phys.*, 68:1506–1512, 1990.

[70] M. Meyyappan, T. R. Govindan, and J. P. Kreskovsky. A two-dimensional moment equations-based analysis of radio frequency capacitively coupled discharges. *J. Appl. Phys.*, 80:7154–7156, 1996.

[71] F. F. Young and C. H. Wu. Radial flow effects in a multidimensional, three-moment fluid model of radio frequency glow discharge. *App. Phys. Lett.*, 62:473–475, 1993.

[72] S. K. Park and D. J. Economou. Analysis of low pressure RF glow discharge using a continuum model. *J. Appl. Phys.*, 68:3904–3915, 1990.

[73] M. Surendra, D. B. Graves, and G. M. Jellum. Self-consistent model of a direct-current glow discharge: Treatment of fast electrons. *Phys. Rev. A*, 41:1112–1125, 1990.

[74] Ph. Belenguer and J. P. Boeuf. Transition between different regimes of RF glow discharge. *Phys. Rev. A*, 41:4447–4459, 1990.

[75] J. W. Bradley. A fluid model of the edge plasma in low-temperature discharges containing beam electrons. *J. Phys. D: Appl. Phys.*, 29:706–715, 1996.

[76] S. Pirooz, A. Ramachandran, and B. Abraham-Shrauner. Two-region computational model for dc glow discharge plasma. *IEEE Trans. Plasma Sc.*, 19:408–418, 1991.

[77] T. E. Nitschke and D. B. Graves. Matching an RF sheath model to a bulk plasma model. *IEEE Trans. Plasma Sc.*, 23:717–727, 1995.

[78] B. Rethfeld, J. Wendelstorf, T. Klein, and G. Simon. A self-consistent model for the cathode fall region of an electric arc. *J. Phys. D: Appl. Phys.*, 29:121–128, 1996.

[79] J. P. Boeuf and L. C. Pitchford. Pseudospark discharge via computer simulation. *IEEE Trans. Plasma Sc.*, 19:286–296, 1991.

[80] F. Y. Huang and M. J. Kushner. A hybrid model for particle transport and electron energy distributions in positive column discharge using equivalent species transport. *J. Appl. Phys.*, 78:5909–5918, 1995.

[81] T. J. M. Boyd and J. J. Sanderson. *Plasma Dynamics*. Thomas Nelson and Sons LTD, 1969.

[82] R. Jancel and T. Kahan. *Electrodynamics of plasmas*. John Wiley and Sons LTD, 1966.

[83] I. P. Shkarofsky, T. W. Johnston, and M. P. Bachynski. *The particle kinetics of plasma*. Addison-Wesley Publishing Company, 1966.

[84] A. Sitenko and V. Malnev. *Plasma physics theory*, volume 10 of *Applied Mathematics and Mathematical Computation*. Chapman and Hall, 1995.

[85] D. P. Lymberopoulos and D. J. Economou. Two-dimensional simulation of polysilicon etching with chlorine in a high density plasma reactor. *IEEE Trans. on Plasma Sc.*, 23:573–580, 1995.

[86] P. Lorrain and D. R. Corson. *Electromagnetic fields and waves*. W. H. Freeman and Company, 1970.

[87] M. Dufresne and P. P. Silvester. Universal matrices for the n-dimensional finite element. In *Third international conference on computation in electromagnetic*, conference publication number 420, pages 223–228. The electronic division of IEE and IEEE UKRI section, IEE, April 10–12 1996.

[88] L. Lapidus and G. F. Pinder. *Numerical solution of partial differential equations in science and engineering.* John Wiley and Sons LTD, 1982.

[89] J. N. Reddy and D. K. Gartling. *The finite element method in heat transfer and fluid dynamics.* CRC Press Inc., 1994.

[90] P. P. Silvester and R. L. Ferrari. *Finite elements for electrical engineers.* Cambridge University Press, Cambridge, third edition, 1996.

[91] P. P. Silvester. Construction of triangular finite element universal matrices. *Inter. J. Num. Meth. Eng.*, 12:237–244, 1978.

[92] P. P. Silvester. Permutation rules for simplex finite elements. *Inter. J. Num. Meth. Eng.*, 18:1245–1259, 1982. (short communication).

[93] J. H. Argyris and O. W. Scharpf. Finite elements in time and space. *Aeronautical J. of the Royal Soc.*, 73:1041–1044, 1969.

[94] M. Yousfi, A. Poinsignon, and A. Hamani. Finite element method for conservation equations in electrical gas discharge areas. *J. Comp. Phys.*, 113:268–278, 1994.

[95] L. R. T. Gardner, G. A. Gardner, and S. I. Zaki. Collisional effects in plasmas modeled by a simplified fokker-planck equation. *J. Comp. Phys.*, 107:40–50, 1993.

[96] E. Zauderer. *Partial differential equations of applied mathematics.* John Wiley and Sons LTD, 1988.

[97] W. H. Liu and A. H. Sherman. Comparative analysis of the Cuthill-McKee and the reverse Cuthill-McKee ordering algorithms for sparse matrices. *SIAM J. Numer. Anal.*, 13:198–213, 1976.

[98] G. H. Golub and C. F. Van Loan. *Matrix Computations.* The Johns Hopkins University Press, 1989.

[99] I. Abbas and P. Bayle. Non-equilibrium between electrons and field in a a gas breakdown ionizing wave: I. macroscopic model. *J. Phys. D: Appl. Phys.*, 14:649–660, 1981.

[100] N. V. Mantzaris, E. Gogolides, and A. G. Boudouvis. A comparative study of CH_4 and CF_4 RF discharges using a consistent plasma physics and chemistry simulator. *Plasma Chem. Plasma Proc.*, 16:301–327, 1996.

IMAGE EVALUATION
TEST TARGET (QA-3)

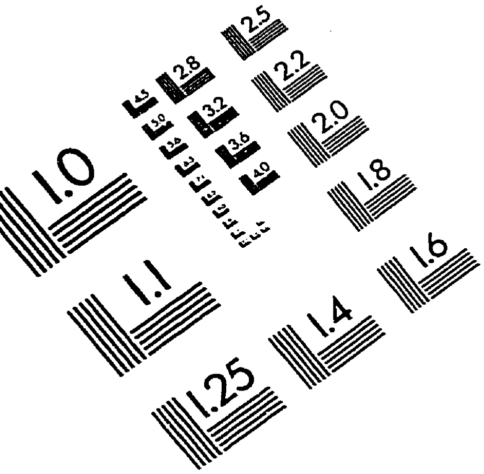

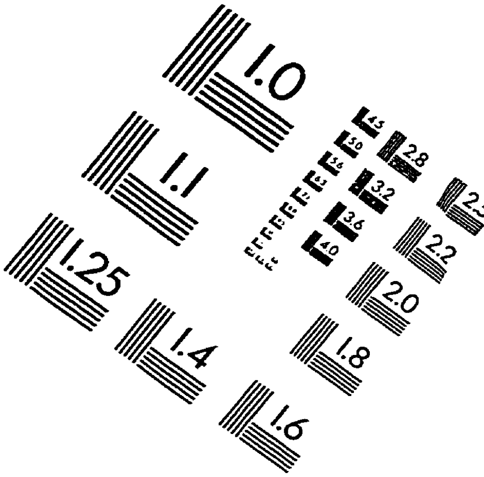

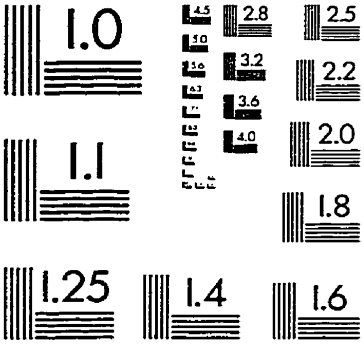

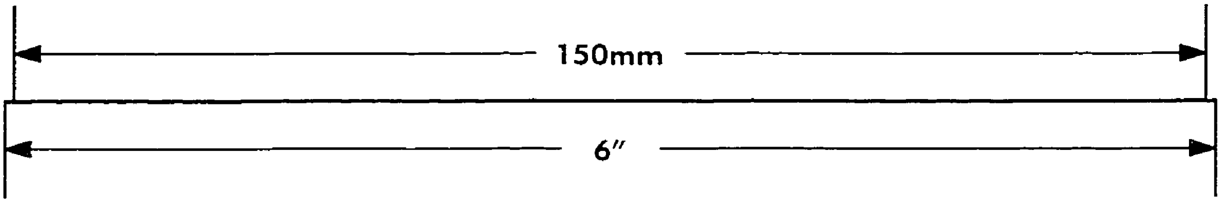

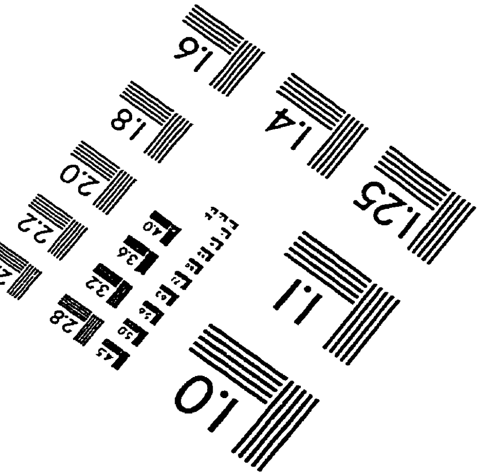

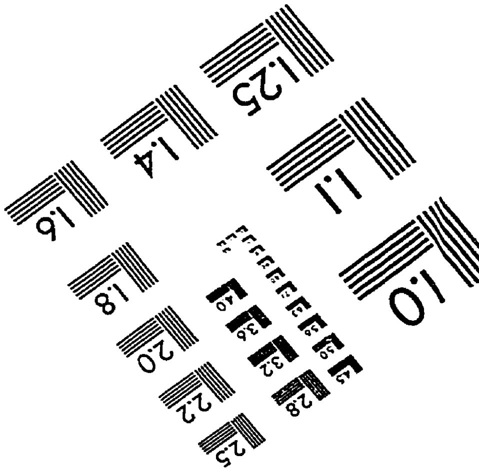

APPLIED IMAGE . Inc
1653 East Main Street
Rochester, NY 14609 USA
Phone: 716/482-0300
Fax: 716/288-5989